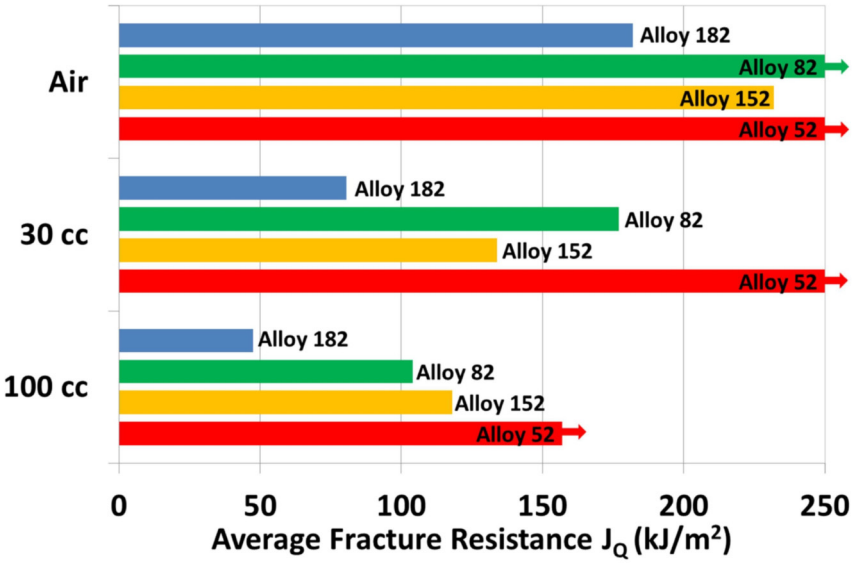

VISIONS • SCIENCE • TECHNOLOGY • RESEARCH HIGHLIGHTS
Dissertation
105

Effect of microstructure on low temperature hydrogen-induced cracking behaviour of nickel-based alloy weld metals

Matias Ahonen

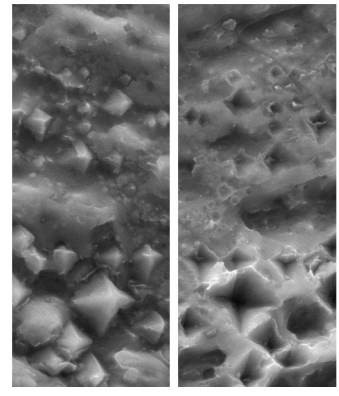

VTT SCIENCE 105

Effect of microstructure on low temperature hydrogen-induced cracking behaviour of nickel-based alloy weld metals

Matias Ahonen

VTT Technical Research Centre of Finland Ltd

Thesis for the degree of Doctor of Science (Tech.) to be presented with due permission of the School of Engineering for public examination and criticism in Auditorium K216, at the Aalto University School of Engineering (Espoo, Finland), on the 18th of September, 2015, at 12 o'clock noon.

ISBN 978-951-38-8338-6 (Soft back ed.)
ISBN 978-951-38-8339-3 (URL: http://www.vttresearch.com/impact/publications)

VTT Science 105

ISSN-L 2242-119X
ISSN 2242-119X (Print)
ISSN 2242-1203 (Online)

JULKAISIJA – UTGIVARE – PUBLISHER

Teknologian tutkimuskeskus VTT Oy
PL 1000 (Tekniikantie 4 A, Espoo)
02044 VTT
Puh. 020 722 111, faksi 020 722 7001

Teknologiska forskningscentralen VTT Ab
PB 1000 (Teknikvägen 4 A, Esbo)
FI-02044 VTT
Tfn +358 20 722 111, telefax +358 20 722 7001

VTT Technical Research Centre of Finland Ltd
P.O. Box 1000 (Tekniikantie 4 A, Espoo)
FI-02044 VTT, Finland
Tel. +358 20 722 111, fax +358 20 722 7001

Juvenes Print, Tampere 2015

Preface

This work was carried out at VTT Technical Research Centre of Finland Ltd mainly within the ENVIS project which was a part of the Finnish Research Programme on Nuclear Power Plant Safety (SAFIR) and also to some extent within the Tekes funded SINI project. The actual writing of this thesis was mainly funded by VTT. The financial support from VTT and other partners in the projects is greatly appreciated.

I would like to express my gratitude to Professor Hannu Hänninen for his guidance, advice and encouraging attitude towards my work. Ulla Ehrnstén is gratefully acknowledged for her support and for giving me a possibility to gather a good test matrix for this thesis. I wish to thank Wade Karlsen for pushing me forward and being my thesis advisor at VTT. I am also grateful to Professor Toshio Yonezawa for his advice and interesting discussions that we had during his stay at Aalto University.

Several colleagues at VTT and Aalto University have had contributions to this work and their help and support has been invaluable. I would like to thank Pasi Väisänen, Aki Toivonen, Esko Arilahti, Jyrki Ranta and Pekka Moilanen for their help and advice in autoclave testing. I also want to thank Tapio Saukkonen, Janne Pakarinen, Marketta Mattila, Taru Lehtikuusi, Juha-Matti Autio and Mykola Ivanchenko for helping me in the microscopy. Olga Todoshchenko and Arto Kukkonen are gratefully acknowledged for their contributions to the hydrogen content measurements. I would also like to thank Pertti Aaltonen for many interesting discussions that we had at the office during this work. There are probably also other colleagues at VTT who have had some contribution to this thesis and their work and support is appreciated.

Finally, I want to thank my lovely wife Sirpa. Without your support this work could not have been completed. I want to thank you for being such an amazing wife throughout the years. I am grateful to my parents Seppo and Kaisuliina Ahonen for being supportive during my whole life. I also want to thank Ivan Dolgov for giving me advice for data processing, but first and foremost for being a good friend during the time in Otaniemi and also after that.

Espoo, August 2015
Matias Ahonen

Doctoral dissertation

Supervising professor	Professor Hannu Hänninen Department of Engineering Design and Production School of Engineering Aalto University Espoo, Finland
Thesis advisor	Ph.D. Wade Karlsen VTT Technical Research Centre of Finland Ltd Espoo, Finland
Pre-examiners	Professor Toshio Yonezawa New Industry Creation Hatchery Center Tohoku University, Japan
	Adjunct Professor Pål Efsing Materials Mechanics and Structural Integrity Department of Solid Mechanics Royal Institute of Technology/KTH Stockholm, Sweden
Opponents	Professor Grace Burke School of Materials The University of Manchester, United Kingdom
	Adjunct Professor Pål Efsing Materials Mechanics and Structural Integrity Department of Solid Mechanics Royal Institute of Technology/KTH Stockholm, Sweden

Contents

List of abbreviations

a	crack length
a_0	initial crack length
Δa	crack growth
α	dimensionless diffusion parameter
AH	a heat treatment for Alloy X-750 consisting of equalizing and ageing
b_0	initial ligament length
b	unbroken ligament length
B	specimen thickness
B_e	effective specimen thickness
BH	direct ageing, a heat treatment for Alloy X-750
C_s	solid composition at the solid/liquid interface
C_0	nominal alloy composition
D_s	diffusivity of solute in solid
E	Young's modulus
E'	elastic modulus that is defined differently for plane stress and plane strain
E_T	activation energy for hydrogen needed to escape from a trap site to the normal lattice site
EBSD	electron backscatter diffraction
EDS	energy dispersive X-ray spectroscopy
f_s	fraction of solid
φ	heating rate

η	dimensionless constant used in J-integral calculation
HEE	hydrogen environment embrittlement
HTH	a heat treatment for Alloy X-750 consisting of solution anneal and ageing
ID	interdendritic
IG	intergranular
IGSCC	intergranular stress corrosion cracking
IHE	internal hydrogen embrittlement
J	J-integral
J_{IC}	value of J-integral near the initiation of stable crack growth, a size independent value of fracture toughness
J_Q	value of J-integral near the initiation of stable crack growth, interim fracture toughness or fracture resistance
K_I	stress intensity factor
k	equilibrium distribution coefficient
L	half the dendrite arm spacing
LTCP	low temperature crack propagation
MA	mill annealed, a heat treatment condition of Alloys 600 and 690
P	load
P_f	load that is used to define a loading rate in ASTM E 1820 – 01 standard
PWHT	post-weld heat treatment
PWSCC	pressurized water stress corrosion cracking
S	roller pin span
SEM	scanning electron microscope
SCC	stress corrosion cracking
SSRT	slow strain rate test
TEM	transmission electron microscope
$T_{0.5mm}$	tearing modulus or tearing resistance at the crack growth 0.5 mm
T_c	desorption peak temperature
t_f	solidification time

TT	thermally treated, a heat treatment condition of Alloys 600 and 690
U_c	energy absorbed in the material
$U_{c(el)}$	energy absorbed in the material due to elastic loading
U_p	energy absorbed in the material due to plastic deformation
V_{pl}	plastic part of the load line displacement
W	specimen width
δ	load line displacement
ν	Poisson's ratio
σ_Y	yield strength
σ_0	flow stress

Original features

The following features are believed to be original:

1. J-R tests were conducted in low temperature hydrogenated water using specimens extracted from dissimilar metal weld (DMW) mock-ups of Alloys 182, 152 and 52 and all-weld metal test blocks. The fracture resistance behaviour of DMWs and all-weld metal specimens of Alloys 182 and 52 were compared. Both types of Alloy 182 behaved in a similar manner regarding fracture resistance, but the DMW of Alloy 52 was found to exhibit higher J_Q values than all-weld metal Alloy 52.

2. Specimens of Alloy 182 and 52 weld metals were J-R tested in low temperature hydrogenated water in both as-welded and post-weld heat treated (PWHT) conditions. PWHT was found to increase the tearing resistance of Alloy 182 whereas the fracture toughness J_Q did not change markedly.

3. Intergranular or interdendritic (IG/ID) fracture surfaces of Alloy 52 weld metal was found to have a fine grain boundary structure. Crack propagation deviates between two parallel planes of a Cr-depleted zone near the grain boundary. The width of this grain boundary zone fits well with the Cr-rich $M_{23}C_6$ carbide size.

4. High temperature pre-exposure (300 °C) was shown to have a rather small but systematic increasing effect on fracture resistance of Alloy 182 and 152 weld metals tested in low temperature water regardless of the hydrogen content of the water.

5. A model was applied for hydrogen thermal desorption of DMWs of Alloys 52 and 182 in order to determine the activation energy for hydrogen desorption. Hydrogen trapping in Alloy 182 was observed to be dominated by a single trapping site whereas in Alloy 52 two different trapping sites were detected. The activation energy for hydrogen desorption was higher for the trapping site of Alloy 182 than for the trapping sites of Alloy 52.

1 Introduction

1.1 An overview of nickel-based alloys

Nickel-based alloys are used in a wide range of industries, including power generation, petrochemical, chemical processing, aerospace and pollution control, due to their good mechanical and corrosion properties. Nickel-based alloys are important to modern industry because of their ability to withstand a wide variety of severe operating conditions involving corrosive environments, high temperatures, high stresses and different combinations of these factors. A specific application of nickel-based alloys in the power generation industry is dissimilar metal welding between carbon steels and austenitic stainless steels because they provide a transition in the coefficient of thermal expansion for elevated temperature service (DuPont et al., 2009).

The most common use for nickel is that of an alloying element in ferrous alloys. The second most important end use is as a base metal in various alloys. Pure nickel has a face-centered cubic (fcc) structure up to its melting point. Therefore, ductile-to-brittle transition, which occurs for example in ferritic steels, does not occur in nickel-based alloys. Nickel has an extensive solubility for many alloying elements. It forms a complete solid solution with Co and almost complete solid solution with Fe. It can also dissolve about 35 % Cr, 20 % each of Mo and W and 5 to 10 % each of Al, Ti, Mn and V. These alloying elements can be used for solid solution strengthening and for formation of intermetallic precipitations that improve the strength of the alloy up to high temperatures, and to improve corrosion and oxidation resistance (Davis, 2000). On the other hand, nickel forms eutectic with various elements including Cr, Mo, Si, Ti, Al, Nb, W, P, S, and C. These eutectic crystals may have a detrimental effect on the fracture resistance and stress corrosion cracking (SCC) susceptibility of nickel-based alloys (Yonezawa, 2012; Yonezawa et al., 2015).

Nickel-based alloys are widely used in nuclear power plants. During the recent decades, earlier widely used Alloy 600 and its weld metals 182 and 82 are being substituted by higher Cr Alloy 690 and its weld metals Alloys 152 and 52 that exhibit better resistance to SCC (EPRI, 2004; Andresen et al., 2007; Buisine et al., 2010).

1.2 Welding metallurgy of nickel-based alloys

1.2.1 Weld solidification

Nucleation of a crystal from a liquid occurs if the energy barrier for nucleation can be overcome. In the case of fusion welding, the energy barrier becomes zero because the liquid metal of the weld pool is in intimate contact with the substrate grains and the liquid wets the substrate completely. Crystals nucleate from liquid metal upon the substrate grains without difficulties (Kou, 2003).

1.2.1.1 Epitaxial and nonepitaxial growth at fusion boundary

When welding without filler metal, nucleation occurs upon the substrate grains in such manner that the crystallographic orientation of the nucleation remains the same with the substrate grains. Such growth initiation process is called epitaxial nucleation (Kou, 2003). The continuity of crystallographic orientation that occurs in epitaxial nucleation across the fusion boundary was first observed by Savage et al. (Kou, 2003) when they applied the Laue X-ray back-reflection technique in order to study welds. For materials exhibiting a face-centered cubic (fcc) or body-centered cubic (bcc) crystal structure, the trunks of columnar dendrites grow in the <100> direction.

When welding with a filler metal, the base metal and weld metal differ from each other and therefore epitaxial growth is no longer possible and new grains will have to nucleate at the fusion boundary. Nelson et al. (1999) proposed that, when the crystal structures of the base metal and weld metal are different at the solidification temperature, nucleation of solid weld metal occurs in heterogeneous sites on the partially melted base metal at the fusion boundary. As a consequence of this, the fusion boundary exhibits random misorientations between the base metal and the weld metal grains.

1.2.1.2 Competitive growth

Away from the fusion line the grain structure is dominated by a mechanism known as competitive growth (Kou, 2003), which is schematically presented in Figure 1. During solidification the grains tend to grow towards the direction of maximum heat extraction, which is the direction perpendicular to the liquid weld metal pool. The dendrites within the grains, however, grow preferably in the easy-growth directions, which is <100> for fcc and bcc materials. Therefore, grains that exhibit a <100> direction perpendicular to the pool boundary will grow more easily and crowd out the less favourably oriented grains.

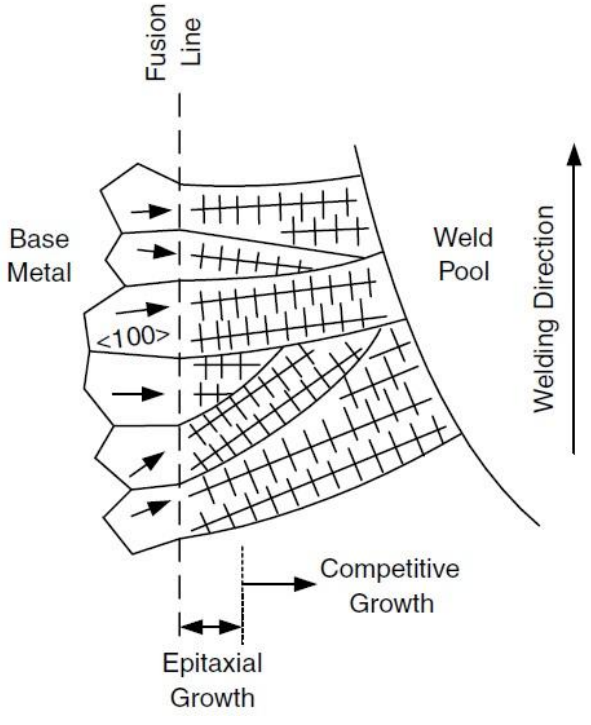

Figure 1. A schematic illustration of competitive growth in bulk fusion zone (Kou, 2003).

1.2.2 Grain structure

There are at least three different metallographically observable types of boundaries in nickel-based weld metals. Different boundaries are important since many of the defects, impurities and precipitates are associated with the boundaries. An illustration of the different boundaries is presented in Figure 2. Figure 2 (a) illustrates schematically how the different types of boundaries are formed during and after welding. Figure 2 (b) shows migrated grain boundaries in FM-52 weld metal (also called Alloy 52 weld metal), which have pulled away from the segregation patterns revealed by the etching (Lippold et al., 2004).

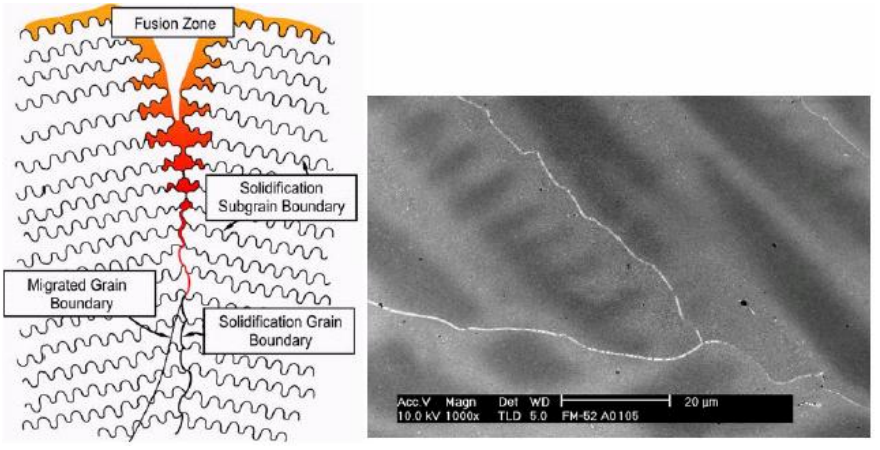

Figure 2. A shematical illustration of the different types of boundaries in (a) and a SEM image after etching showing migrated grain boundaries in (b) (Lippold et al., 2004).

Dendrite boundaries are a class of so called solidification subgrain boundaries (SSGB). These boundaries are evident in microstructure because of their different composition from the adjacent bulk microstructure. The dendrites within the same grain grow parallel to each other so that the crystallographic misorientations across the SSGBs are typically less than five degrees. Hence, the dislocation density along the SSGBs is low (Lippold et al., 1992).

The solidification grain boundaries (SGB) form when packets of dendrites intersect. These boundaries exhibit a high angular misorientation because each of the dendrite packets has a different growth direction. The large misorientation results in the development of a dislocation network along the SGB (DuPont et al., 2009).

It must be pointed out that the terminology of the different boundaries of welds varies. It is somewhat usual that solidification grain boundaries are called “dendrite boundaries” (Peng et al., 2003; Morra et al., 2014). It also appears that solidification grain boundaries are called merely “grain boundaries” by other researchers (Bruemmer et al., 2007). Another difficulty is to make a difference between SGBs that form as a result of intersection of dendrite packets exhibiting a small or large angular misorientation. If the angle between the dendrite packets is small the difference between SGBs and SSGBs becomes obscure. In this work cracking that occurs along boundaries in a weld is often referred as intergranular/interdendritic (IG/ID) cracking meaning the solidification grain boundaries, that are in literature called both grain and dendrite boundaries. Another reason for using the term IG/ID is that it is difficult to distinguish the difference between the grain and dendrite boundaries based on their appearance on the fracture surface.

In some cases it is possible that the solidification grain boundary of a nickel-based alloy weld starts to migrate to a position with lower boundary energy. The

chemical boundary still remains where the SGB was originally located as a consequence of the solidification. The new boundary that essentially is a crystallographic boundary is called a migrated grain boundary (MGB). This kind of a boundary occurs for example in Alloy 52 weld metal. The original SGB has a tortuous appearance and thus a high surface energy. A MGB is more smooth and straight and therefore energetically favourable. In multipass welds reheating provides the energy to activate such behaviour. The composition of a MGB varies locally depending on the composition of the microstructure where the grain boundary has migrated. Some segregation may also occur in MGBs via grain boundary sweeping mechanism, where fast diffusing interstitial elements such as S, P, B, O etc. may move with the boundary when the boundary migrates and then stay in the grain boundary. Migrated grain boundaries usually occur only in fully austenitic weld metals, because second phases are effective in pinning the SGBs and thus the migration cannot occur (DuPont et al., 2009).

Dynamic recrystallization occurs in some nickel-based welds. Morra et al. (2014) observed recrystallized grains in Alloy 52 mock-up at various locations, but especially at the mid-section of the weld between weld passes (Figure 3 a)) and crack tips. Dynamic recrystallization was commonly observed ahead of ductility dip cracks (DDC) (Figure 3 b)).

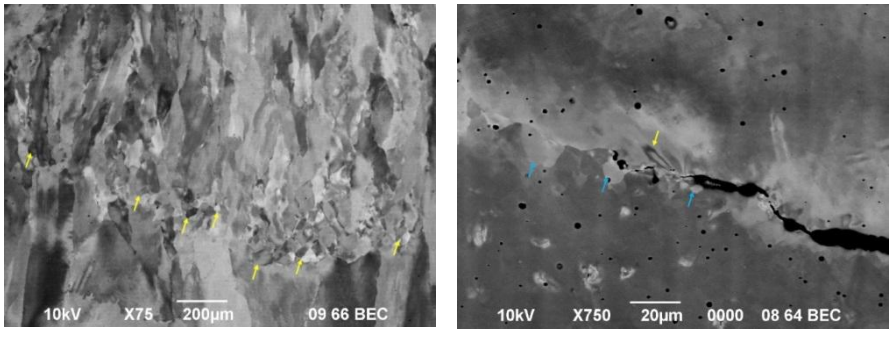

Figure 3. Examples of dynamic recrystallization in Alloy 52 weld mock-up. In a), a large section of recrystallized grains between weld passes. Recrystallized grains are indicated with yellow arrows. In b), dynamic recrystallization ahead of a ductility dip crack in Alloy 52 weld mock-up. Yellow arrow shows a plume of strain at a crack tip and blue arrows show areas of possible recrystallization (Morra et al., 2014).

1.2.3 Elemental segregation during solidification

Distribution of alloying elements across the cellular or dendritic substructure and the phases that form during solidification are important microstructural features in nickel-based alloys. The solidification behaviour of Ni-based alloy welds is con-

trolled by solute redistribution behaviour. Brody and Flemings (1966) proposed a following equation for solute redistribution of alloying elements:

$$C_s = kC_0\left[1 - \frac{f_s}{1 + \alpha k}\right]^{k-1}, \quad (1)$$

where C_s is the solid composition at the solid/liquid interface, C_0 is the nominal alloy composition, f_s is the fraction solid, and k is the equilibrium distribution coefficient. α parameter is a dimensionless diffusion parameter that is defined as:

$$\alpha = \frac{D_s t_f}{L^2}, \quad (2)$$

where D_s is the diffusivity of solute in solid, t_f is the solidification time, i.e., cooling time between the liquidus and terminal solidus, and L is half the dendrite arm spacing. The $D_s t_f$ term describes the distance a solute atom can diffuse in the solid during solidification, while the L term represents the length of the concentration gradient. If the diffusion in the solid is insignificant, i.e., $D_s t_f << L^2$, solute redistribution can be presented as proposed by Scheil (DuPont at al., 2009):

$$C_s = kC_0[1 - f_s]^{k-1}. \quad (3)$$

The Scheil equation assumes equilibrium at the solid/liquid interface, complete diffusion in the liquid, negligible diffusion in the solid and negligible dendrite tip undercooling. The k term, which is defined as a relation of the solid and liquid composition so that $k=C_s/C_l$, describes the solute atoms' tendency to partition to the liquid and solid phases during solidification. As the liquid solidifies, solute atoms are rejected by the solid into the liquid if $k < 1$. Elements with very low k values can produce steep concentration gradients across the cellular or dendritic substructure of the weld.

The Scheil equation has been shown to describe the solute redistribution rather well in nickel-based alloys. Joo and Takeuchi (1994) evaluated α parameter values for alloying elements of Alloy 713, which is a precipitation-strengthened Ni-based alloy. They discovered that $\alpha << 1$ for all the elements considered under all cooling rate conditions. This kind of behaviour seems to be similar in other Ni-based alloys as well (Heubner et al., 1988). Thus, solid state diffusion of alloying elements in nickel-based alloys is insignificant during solidification. However, α parameter values calculated for C are significantly greater than unity. This is due to C diffusion by interstitial mechanism that enables C to exhibit diffusion rates that are orders of magnitude higher than those for the substitutional alloying elements (Bose & Grabke, 1978).

DuPont et al. (2009) have summarized experimentally measured k values for different alloying elements in several Ni-based alloys that include both solid-solution and precipitation-strengthened alloys. The values represent k at the start of the solidification and do not account for variations in k that may occur during

solidification as the temperature decreases. The *k* values measured for different complex multicomponent alloys and Ni-X binary systems do not differ significantly from each other, except for Nb, Mo and in some quantity for Ti and Si. The *k* value of Nb ranges from 0.42 to 0.58. The value is lower in the multi-component alloys than in simple Ni-Nb system. This indicates that the presence of other alloying elements decreases the solubility of Nb in Ni. The *k* values for elements with similar atomic radii to Ni, namely Fe, Cr, and Co have *k* values close to unity. Also, the *k* values for W and Al are close about 1. Mo exhibits values ranging from 0.71 to almost one and Ti from 0.58 to 0.76. Si exhibits *k* values ranging from 0.51 to 0.69. The *k* values of C range from 0.21 to 0.27.

Young et al. (2001) calculated (JMatPro, version 4.1) solidification ranges for different materials commonly used in nuclear power plant applications, including nickel-based weld metals EN82, EN52 and EN52M. It must be pointed out that Scheil-based calculations are approximate and over predict the actual solidification temperature range because of the simplified assumptions such as equilibrium at the solid/liquid interface, complete diffusion in the liquid, negligible diffusion in the solid and negligible dendrite tip undercooling. According to the calculations the solidification range of EN52 is at about 1300–1400 °C, whereas EN82 solidifies at a range of about 1100–1350 °C, thus exhibiting solidification range more than twice larger than EN52.

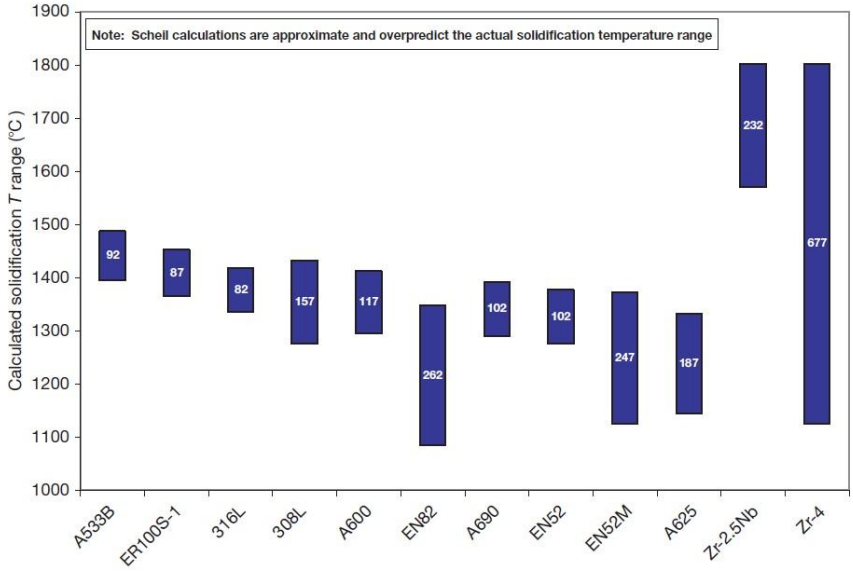

Figure 4. Comparison of the calculated (JMatPro, Version 4.1) solidification temperature ranges of some common materials used in nuclear power systems. Material compositions used for the calculation are typical values and significant variability exists within each alloy's specification range (Young et al., 2001).

1.2.4 Phases of nickel-based alloys

Phase transformations observed in nickel-based alloys depend on the chemical composition of the alloy. Solid-solution strengthened alloys contain little or no Al, Ti or Nb. They are strengthened primarily by the addition of substitutional elements such as Cr, Fe, Mo, W and Cu which provide solid-solution strengthening of the austenite (fcc) microstructure. Nb provides some solid-solution strengthening but it is primarily added because it is carbide former. The precipitation hardenable alloys contain several percent Al and Ti and some also substantial amounts of Nb which can form a strengthening precipitate with nickel (Ni_3Nb) (Davis, 2000; DuPont et al., 2009). Thermal treatment (TT) introduces formation of carbides in wrought nickel-based Alloy 600 and higher Cr Alloy 690. Alloy 600 exhibits M_7C_3 along the grain boundaries and additionally some intragranular M_7C_3 carbides, while Alloy 690 exhibits only $M_{23}C_6$ carbides (Yonezawa & Onimura, 1989).

Carbides are important precipitates in nickel-based alloy welds because they increase the strength of the grain boundaries when precipitated there, and have an effect on the corrosion behaviour of the material. Cr is an effective carbide former because it has a strong affinity with C. The welding process generates heat which enables Cr to interact with C to form carbides such as $M_{23}C_6$ and M_7C_3 which then precipitate on the grain boundaries. The formation of carbides may result in Cr depletion within the first-pass welding layer or in the heat-affected zone (HAZ), which causes degradation of the corrosion resistance. Cr depletion can be avoided by either increasing the Cr content of the alloy, or by alloying high affinity carbide formers such as Ti and Nb which typically form MC-type carbides (Davis, 2000; Lee et al., 2004). The typical phases observed in the nickel-based alloys are presented in the following.

1.2.4.1 Gamma prime (γ')

Gamma prime is an intermetallic precipitate and has an ordered fcc structure. Its composition is Ni_3Al or $Ni_3(Al, Ti)$, although Co and Cr can replace some of the Ni. Fe can replace either Ni or Al. The lattice parameter of γ' is similar to the austenite matrix, and thus the formed precipitates are coherent with the matrix. The shape of the precipitate can be either spherical (Fe-Ni-based alloys) or cuboidal, depending on Mo content and Al/Ti ratio. Those elements have also an effect on the lattice mismatch. When the lattice mismatch between γ' and the matrix is high, extended exposure above 700 °C causes formation of undesirable phases, namely η (Ni_3Ti) or δ (Ni_3Nb) (Davis, 2000).

1.2.4.2 Gamma double prime (γ'')

Gamma double prime has a bct structure with a Ni_3Nb composition and it is found in Fe-Ni-based alloys containing Nb. It is known especially as a strengthening phase of Alloy 718. γ'' has a disc-shaped morphology with a well-defined relationship to the austenite matrix. Strengthening is caused by lattice mismatch that causes coherency strains. Application of alloys strengthened by γ'' is restricted to temperatures below 700 °C because γ'' is a metastable phase. Extended exposure to temperatures above 700 °C causes loss of strength due to rapid coarsening of γ'' and formation of stable orthorhombic δ phase (Ni_3Nb) (Davis, 2000). δ phase is incoherent with the Ni matrix and therefore not an effective strengthener. In addition, the δ phase can lead to embrittlement associated with a loss of ductility (Davis, 2000; DuPont et al., 2009).

1.2.4.3 MC carbide

The MC-type carbide has a fcc crystal structure and usually forms at the end of solidification by eutectic-type reactions with the austenite matrix (DuPont et al., 1988). Also M(CN)-type carbonitrides, that are similar to MC-type carbides, exist in Ni-based alloys. The most notable metallic components of MC carbides are Nb and Ti because they have a strong tendency to segregate to the liquid during solidification. Also Ta, Hf and Th and Zr can act as a metallic component of the carbide. Since the precipitation of MC-type carbides occurs at the end of solidification, the MC carbides are distributed at the interdendritic and solidification grain boundary regions. They appear as globular or irregularly shaped particles. MC carbides are strong hydrogen traps and may also promote increased corrosion activity of nickel-based alloys in equalized and aged (Fish et al., 1997) and solution annealed and aged (Mills et al., 1999) conditions.

1.2.4.4 $M_{23}C_6$ carbide

$M_{23}C_6$ has a fcc (Davis, 2000) or complex cubic (DuPont et al., 2009) crystal structure and it is the most important carbide in Ni-based alloys. It forms on the grain boundaries during ageing (Davis, 2000) or in the cooling portion of the weld thermal cycle (DuPont et al., 2009) and, when properly formed, increases the strength of the grain boundaries to balance the matrix strength. The most desirable morphology is discrete globular, but also films, platelets, lamellae, and cells have been observed. According to Honeycombe & Bhadesia (1995), the particles usually develop a polyhedral habit, but occasionally in steels deformed at elevated temperatures a more regular cubic morphology is displayed. The morphology of the $M_{23}C_6$ carbide is of great importance because the carbides may precipitate as a continuous grain boundary film and degrade the properties of the material significantly (DuPont et al., 2009). Cr is the primary metallic element of the $M_{23}C_6$ carbide but Ni, Co, Fe, Mo, and W can substitute for it (Davis, 2000).

Kekkonen et al. studied the morphology and growth of $M_{23}C_6$ carbides in 304-type austenitic stainless steel (Kekkonen et al., 1985). According to their study, $M_{23}C_6$ carbide growth causes formation of a de-alloyed zone in AISI 304 type austenitic stainless steels due to grain boundary migration and Cr depletion, as schematically presented in Figure 5.

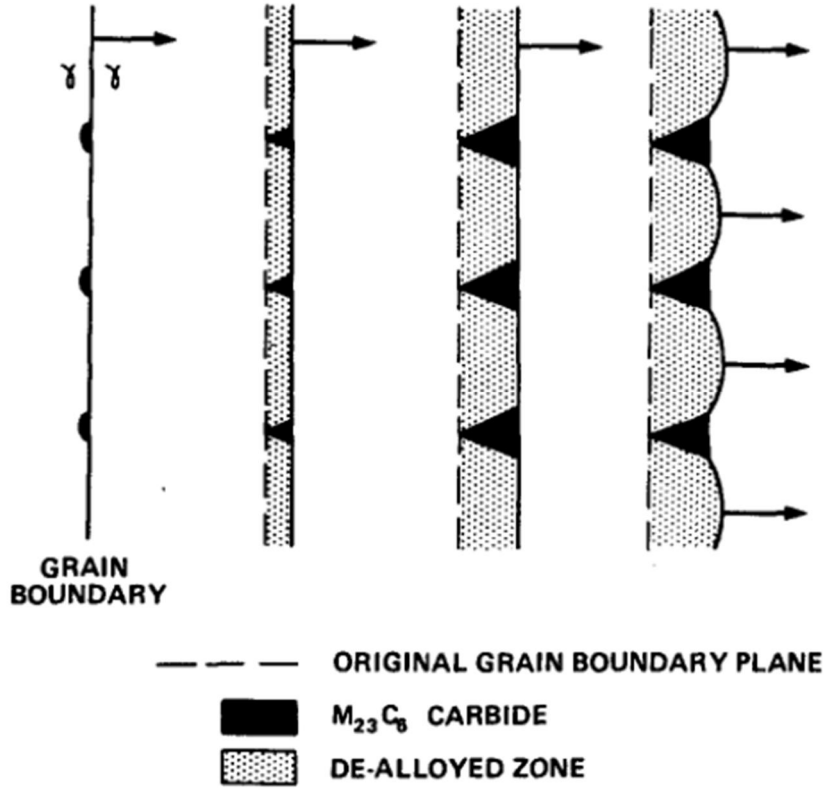

Figure 5. A schematic presentation of the various stages of $M_{23}C_6$ carbide growth in AISI 304 stainless steel during grain boundary migration (Kekkonen et al., 1985).

The $M_{23}C_6$ carbide usually forms in the temperature range of 760 to 980 °C in Ni-based alloys. Discrete $M_{23}C_6$ carbide formation is considered beneficial in Ni-based alloys because it can improve the creep strength of the material by restricting grain boundary sliding (DuPont et al., 2009). In austenitic stainless steels, the $M_{23}C_6$ carbide precipitates in the temperature range of 500 to 950 °C and is usually harmful because the precipitation leads to Cr depletion at the grain boundaries and thus degradation of intergranular corrosion resistance of which the classic weld heat-affected zone grain boundary sensitization is the well-known example (Peckner & Bernstein, 1977). The formation of $M_{23}C_6$ has been found to cause

strong, although not continuous, Cr depletion with levels down to ~5 % (13-15 % Cr in the matrix) in the grain boundary region also in Ni-based Alloy 182 weld metal (Thomas et al., 2009) that has been widely used in nuclear power plants. However, there are conflicting reports on the benefits and disadvantages of sensitization of Ni-based weld metals on primary water stress corrosion cracking (PWSCC) (Webb & Burke, 1995).

Both the matrix and the $M_{23}C_6$ carbide have cubic symmetry and based on electron diffraction evidence the orientation relationship has discovered to be as follows (Honeycombe & Bhadesia, 1995):

$$\{100\}_{M_{23}C_6} // \{100\}_{\gamma} : \langle 100 \rangle_{M_{23}C_6} // \langle 100 \rangle_{\gamma}$$

The lattice parameter of $M_{23}C_6$ carbide is approximately three times that of austenite, so the diffraction patterns are readily identified (Honeycombe & Bhadesia, 1995). An example of a TEM image showing $M_{23}C_6$ carbides at a migrated grain boundary of Alloy 52 is presented with a corresponding diffraction pattern in Figure 6 (Ramirez & Lippold, 2004).

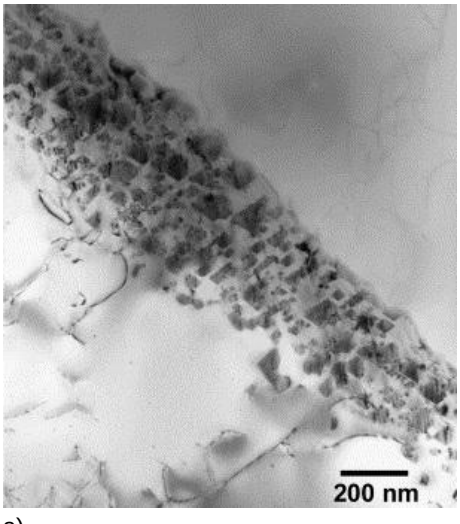

a)

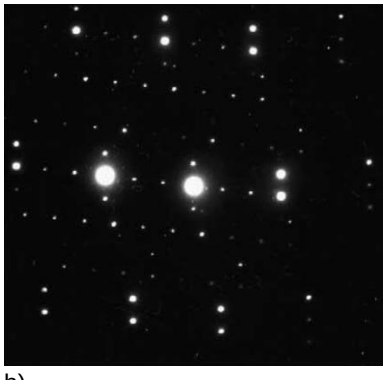

b)

Figure 6. $M_{23}C_6$ carbides at a grain boundary of Alloy 52 in a), and the selected area diffraction (SAD) pattern of the austenite grains and the carbides showing a cube-on-cube orientation relationship in b) (Ramirez & Lippold, 2004).

Yonezawa has studied the effects of chemical composition and fabrication method on carbide and other phase precipitation in nickel-based Alloy 690 TT (Yonezawa, 2013). The studied material was representative to the one used by Mills and

Brown (1999, 2002) ("Bettis' Material"). It is usually assumed that $M_{23}C_6$ precipitates during ageing in austenitic materials (Peckner & Bernstein, 1977; Davis, 2000; DuPont et al., 2009), but according to the calculation it appears that in some cases also formation from the liquid is possible. However, in commercial Alloy 690 primary $M_{23}C_6$ carbides are not common. The results of the calculation (Figure 7), that was based on Scheil's model, show that the solidification range is from slightly above 1400 °C to slightly below 1300 °C, which is in good agreement with the result obtained by Young et al. (2001) for Alloy 690, presented in Figure 4. Yonezawa's results show that in the case of the Bettis' material there are several phases that crystallize during solidification. At the end of solidification the crystallizing phases include Laves phase, austenitic matrix (fcc), titanium carbonitrides (Ti(C,N)) and $M_{23}C_6$ carbides. Micro cracks and voids were observed in eutectic (primary) $M_{23}C_6$ grain boundary carbides in cold-rolled Alloy 690 TT, but not in secondary $M_{23}C_6$ grain boundary carbides. Yonezawa comes to a conclusion that primary $M_{23}C_6$ grain boundary carbides must have an accelerating effect on intergranular stress corrosion cracking (IGSCC) growth rate.

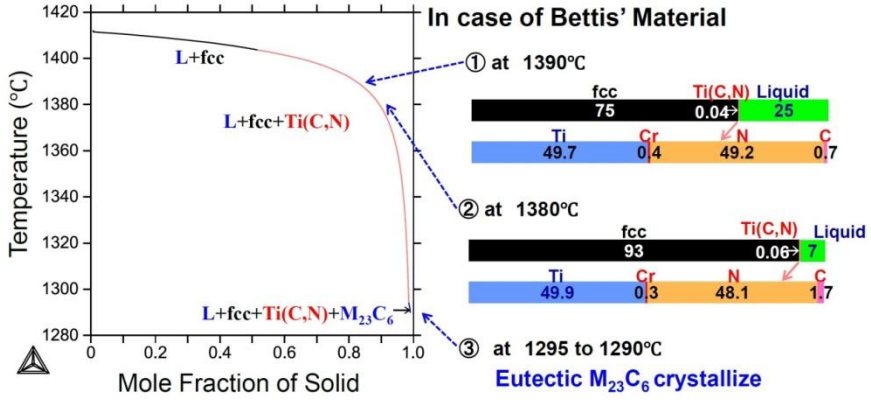

Figure 7. Scheil calculation showing phases formed during the solidification of the "Bettis' material" Alloy 690 (Yonezawa, 2013).

The microstructural studies of Alloy 690 by Yonezawa show that the applied fabrication methods have an effect on the $M_{23}C_6$ grain boundary carbide structure, as illustrated in Figure 8. If thermal treatment is applied after light forging and solution heat treatment (SHT), and the $M_{23}C_6$ carbides are relatively large and prone to cracking during cold rolling. On the other hand, if heavy forging with SHT followed by thermal treatment (TT) is applied after light forging and SHT, a desired microstructure, where there are no cracked carbides at the grain boundaries even after heavy cold rolling, is attained.

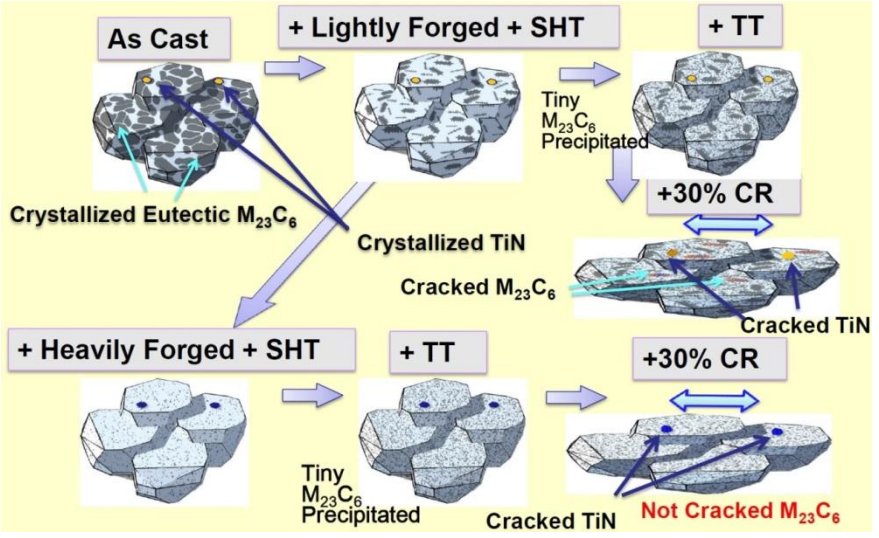

Figure 8. Illustration of the effect of fabrication on the $M_{23}C_6$ grain boundary carbide structure (Yonezawa, 2014).

Yonezawa has also studied the coherency of the $M_{23}C_6$ grain boundary carbides, both in Alloy 690 (Yonezawa, 2013, 2014) and in Alloy X-750 (Yonezawa et al., 1993). Yonezawa et al. (1993) showed that coherent and incoherent carbides have different effect on IGSCC behaviour of Alloy X-750. In their study material with incoherent carbides cracked in SSRT tests performed in hydrogenated high temperature water, whereas material with coherent carbides did not crack. Hydrogen content (up to 40 cm^3 H_2/kg H_2O) of the water did not have an effect on IGSCC susceptibility in simulated PWR water, thus it was concluded that the carbide coherency is the dominating factor in the IGSCC susceptibility of Alloy X-750.

1.2.4.5 M_6C carbide

M_6C is randomly distributed carbide that exhibits a fcc structure and lattice parameter close to that of $M_{23}C_6$ (a_0 = 1.085-1.175 nm for M_6C, a_0 = 1.050-1.070 nm for $M_{23}C_6$) (Davis, 2000) and it is also otherwise similar to $M_{23}C_6$ (Richards & Chaturvedi, 2000). M_6C carbide is generally rich in Mo or W, but other elements such as Cr, Ni, or Co, may substitute for it to some degree. It is observed in as-cast condition of nickel-based alloys that are rich in Mo or W. It is usually dissolved during heating before hot working. It may precipitate to grain boundaries where it manifests a blocky form or intragranularly exhibiting a Widmannstätten pattern (Davis, 2000).

1.2.4.6 M_7C_3 carbide

M_7C_3 carbides are present in some nickel-based alloys, such as Nimonic 80A (Davis, 2000) and Alloy 600 (Yonezawa & Onimura, 1989; Kaneda et al., 2007). The M_7C_3 carbide precipitates when the material is heated above 1000 °C and has a hexagonal structure. Addition of elements such as Co, Mo, or Nb to nickel-based alloys prevents formation of M_7C_3 (Davis, 2000).

1.2.4.7 Other phases

Mo and W act as stabilizing elements for some topologically close packed (tcp) phases, such as σ, μ, P and Laves. Those phases are generally undesirable due to their negative effect on both weldability and properties of nickel-based alloys. Their complex crystal structure leads to limited slip systems, which makes them brittle. They can reduce the ductility and toughness of the material if they are present in considerable amounts. Laves phase is observed as coarse intergranular, and sometimes intragranular particles in welds that contain Nb. Also Si, in addition to Nb, promotes formation of Laves phase in Alloy 718 (Davis, 2000; DuPont et al., 2009).

1.2.5 Dissimilar metal welding

Nickel-based alloy weld metals are often used when welding dissimilar combinations, such as pressure vessel steels (low alloy steels) to stainless steels. In these applications, several inherent properties of nickel-based alloys make them an ideal choice of material. When austenitic stainless steels are welded directly to carbon steels, the difference in coefficient of thermal expansion (CTE) can lead to fatigue and creep failures in the HAZ of the carbon steel (Lippold & Kotecki, 2005). The CTE of Ni lies between those of austenitic stainless steels and carbon steels and thus it provides a gradation of CTE across the weld joint and better distributes thermal stresses that are originated by the different CTEs of the joined materials. Nickel-based weld metals also have good corrosion resistance in as-welded condition (Kiser, 1990) and good impact strength at low temperatures (Hilkes et al., 2004). However, dilution of the two different base metals causes a non-identical composition within the fusion zones, which may degrade the properties of the weldment in some cases (Jeng et al., 2005).

Large compositional gradients exist in the fusion boundary region when welding carbon steels with Ni-based alloys. C diffuses from the HAZ to the fusion zone during the welding or post-weld heat treatment (PWHT) due to this gradient (Lundin, 1982) which can result in formation of some martensite according to the Schaeffler diagram (DuPont et al., 2009). The tendency for C to migrate from HAZ into the weld metal during PWHT is especially strong in high-Cr alloys, such as Alloy 52 (Mouginot & Hänninen, 2013; Hänninen et al., 2014).

Type II boundary is a grain boundary that occurs only in dissimilar joints. It runs approximately parallel to the fusion line and is located a few microns from the

fusion zone (DuPont et al., 2009). Type II boundary is important because a number of instances of in-service cracking has been associated with them. It is a weak and approximately planar interface that makes a preferential cracking site in cases of large local mismatch between the hard martensitic zone at the fusion line and the type II boundary region.

1.3 SCC of nickel-based alloys

Alloy 600 was developed in the 1950s as an alternative material to austenitic stainless steels. Alloy 600 has been used for stream generator tubing because it was observed to have a high resistance to SCC in chloride solutions, as reported by Copson (1959). Coriou et al. (1960) discovered the SCC susceptibility of some Ni-rich Fe-Ni-Cr alloys in high temperature, high purity water, but the validity of their observation was questioned. However, widespread occurrence of intergranular cracking of stream generator tubing in many PWR plants has revealed the generic character of the phenomenon (Berge, 1988; Welty & Blomgren, 1990). In the 1970s, thermally treated (TT) Alloy 600 was developed in order to improve the SCC resistance of Alloy 600, but SCC was eventually detected in TT material as well. A higher Cr nickel-based Alloy 690 was developed as an alternative material for steam generator tubing and it has performed well thus far.

Both Alloys 182 and 82 were observed to be susceptible to SCC in PWR conditions in laboratory tests (Andresen, 1987). Later, the SCC susceptibility of these weld metals was verified also by cracking cases in the operating power plants (Rao et al., 2002; Shah & MacDonald, 1993). SCC has occurred in PWRs in control rod drive mechanisms and thermocouple nozzles made of Alloy 600. In BWRs, the first case of intergranular cracking in a safe-end made of Alloy 600 was observed 1978 in Duane Arnold (commercial start 1974). The crack had initiated in the HAZ of the Alloy 600 and penetrated into the Alloy 182 weld metal causing a leak (Pasupathi et al., 1980). Since that several similar cracks have been found in BWR's.

Precipitate-hardenable nickel-based Alloy X-750 has also been found to be susceptible to SCC in PWR and BWR water. A pronounced effect of heat treatment on the IGSCC susceptibility has been reported (Hosoi et al., 1984; Yonezawa et al., 1984; Grove & Petzold, 1985; Skeldon & Hurst, 1988). A heat treatment that causes lower susceptibility consists of solution annealing at a relatively high temperature (>1050 °C), followed by a single-step ageing treatment of approximately 20 h at about 700 °C.

1.4 Low temperature crack propagation (LTCP)

Low temperature crack propagation (LTCP) is widely considered as a hydrogen-induced embrittlement phenomenon that has been observed in laboratory conditions for various nickel-based alloys at the temperature range of ~50 to 150 °C in

hydrogenated water. No LTCP incidents have been reported in open literature to date.

1.4.1 LTCP of Alloy X-750

Low temperature SCC, later named as LTCP, was first reported by Grove and Petzold (1985). They performed rising load tests for Charpy-sized precracked three-point bend specimens loaded at a constant extension rate of 0.005 cm/min in destilled 93 °C water. The studied material was Alloy X-750, which is a high-strength precipitation hardenable alloy originally developed for gas turbines and aerospace industry. It is widely used in internal applications for both Boiling Water Reactor (BWR) and Pressurized Water Reactor (PWR) designs, such as fuel assembly hold-down springs, control rod guide tube support pins, jet pump beams, and reactor internals structural bolting. Alloy X-750 is very similar in composition to solution annealed Alloy 600, but it contains additions of Ti and Al, which combine with Ni to form gamma prime (γ') precipitates, Ni_3Al and $Ni_3(Al, Ti)$, for strengthening (Davis, 2000). The nominal composition of Alloy X-750 is presented in Table 1. Although Alloy X-750 has performed well in the light water reactor environments, it has been observed that it is susceptible to fail under certain reactor operational and environmental conditions with low ductility by a stress corrosion mechanism acting alone or as the concluding mechanism in instances where fatigue cracks are already present (Baty et al., 1984). Grove and Petzold (1985) investigated the high and low temperature SCC susceptibility of Alloy X-750 by applying three different heat treatments:

1. Equalized and aged (AH), 885 ˚C/24 hours + 704 ˚C/20 hours,
2. Direct-aged (BH), 704 ˚C/20 hours
3. Solution annealed and aged (HTH), 1093 ˚C/1 hour + 704 ˚C/20 hours.

AH microstructure typically consists of coarse gamma-prime precipitates within the grains and few carbide precipitates at the grain boundaries. BH microstructure consists of grain boundary carbides that appear semi-continuous to continuous. Contrary to the AH heat treated microstructure, no coarse gamma-prime is visible within the grains. The microstructure of condition HTH is identical to that of typical BH, except that the grain size is larger. In addition, the 1093 °C solution anneal heat-treatment step of condition HTH significantly reduces variability introduced during processing. Gamma-prime, $M_{23}C_6$, and most MC carbides are put into solution, and grain growth occurs. The $M_{23}C_6$-type carbides precipitate at the new grain boundaries during aging at 704 °C, and fine gamma-prime is precipitated throughout the material. Grain growth during solution annealing is required to reduce phosphorus at the grain boundaries (Grove & Petzold, 1985).

The test results obtained with Charpy-sized (10x10x55 mm) precracked three-point bend specimens (Grove & Petzold, 1985) showed extremely rapid crack growth rates of 250 cm/day in low temperature water. Grove and Petzold conclud-

ed that the segregation of impurities, most importantly phosphorous, to the grain boundaries has a detrimental effect on the resistance to low temperature cracking. Mills et al. (1999) performed an extensive fracture mechanics based study on SCC of Alloy X-750 in high and low temperature water. They compared the LTCP behaviour of different heat treated conditions (AH, BH and HTH) of Alloy X-750 by conducting rising load tests with compact tension (CT) and three-point-bend specimens, constant displacement tests with bolt-loaded CT specimens, and controlled-load testing with CT specimens. The test matrix included both hydrogen-precharged and non-precharged specimens. They observed that the decrease in fracture resistance (K_{Pmax}) for a susceptible BH heat was associated with a fracture mechanism transition from ductile dimple rupture in air to intergranular LTCP in water. For the susceptible heat of BH heat treated Alloy X-750 the rapid crack advance leads to failure within one minute.

The effect of water temperature and hydrogen content on fracture resistance (K_{Pmax}) was studied by Mills et al. (1999) for AH, BH and HTH heat treated Alloy X-750. Selected results for representative material heats for each heat treatment condition are presented in Figure 9. It must be pointed out that the results for AH samples were chosen based on LTCP susceptibility, whereas the results for BH and HTH samples are representative for the whole test matrix. The results were obtained with hydrogen contents 16, 35 and 60 cm^3 H_2/kg H_2O at temperatures ranging from room temperature to 150 °C. HTH heats exhibit superior LTCP resistance compared to AH and BH heats. BH tends to be the most susceptible material condition to LTCP.

Table 1. Nominal chemical composition of Alloy X-750 (According to Special Metals).

Ni (+Co)	Cr	Fe	Ti	Al	Nb+Ta	Mn	Si	S	Cu	C	Co
70.00 min.	14.0-17.0	5.0-9.0	2.25-2.75	0.40-1.00	0.70-1.20	1.00 max.	0.5 max.	0.01 max.	0.50 max.	0.08 max.	1.00 max.

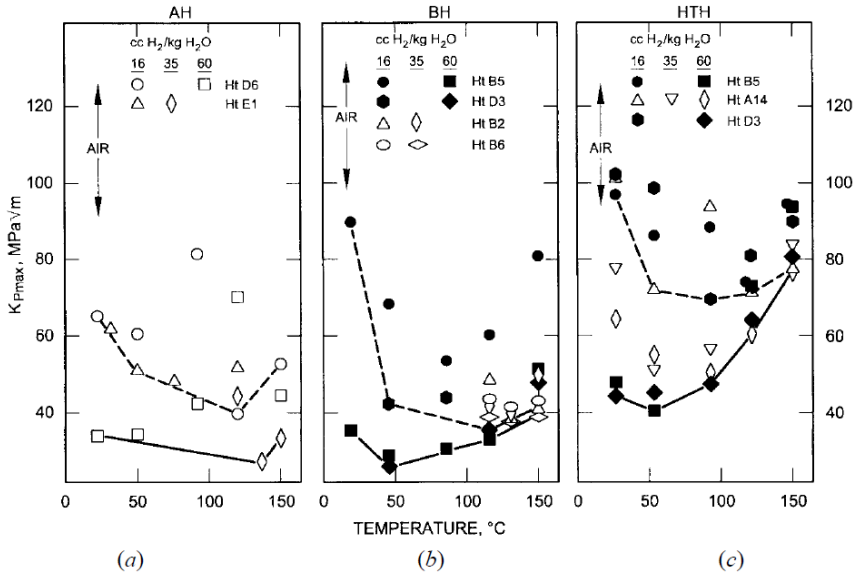

Figure 9. Rising load test results for Alloy X-750 in AH (a), BH (b), and HTH (c) conditions tested in hydrogenated water with varying temperature (Mills et al., 1999).

1.4.1.1 LTCP mechanism of Alloy X-750

Mills et al. (1999) observed that LTCP is a hydrogen-induced phenomenon. Their findings demonstrate that the change in fracture mechanism from ductile dimple to more brittle intergranular cracking occurs regardless of the source of hydrogen. Hydrogen-precharged specimens tested in air showed that hydrogen alone, without corrosion, can produce intergranular fractures that are indistinguishable in fractographic appearance from those produced in low temperature water without precharging.

Symons has studied the effect of hydrogen on the fracture toughness of Alloy X-750 by performing fracture toughness tests (Symons & Thompson, 1997; Symons, 1999, 2001). He compares the difference between internal hydrogen embrittlement (IHE) and hydrogen environment embrittlement (HEE) of Alloy X-750 (Symons, 2001). It was observed that the dominating factor in the hydrogen-induced embrittlement is the grain boundary hydrogen concentration. The fracture toughness test results showed that alloy X-750 is susceptible to both IHE and HEE, as shown in Figure 10. It was further shown that much less hydrogen is required to embrittle the material in hydrogen environment compared to internally charged hydrogen. Symons proposed a model to describe the role of grain boundary hydrogen concentration on the fracture behaviour and the characteristic dis-

tance ahead of the crack where fracture initiates. The degree of embrittlement of Alloy X-750 is controlled by the grain boundary hydrogen concentration irrespective of test temperature and bulk hydrogen concentration. According to Symons (2001), the characteristic distance is less for HEE than for IHE, because the strain is much higher in HEE case. Thus, for the same hydrogen levels in both cases, the toughness for HEE is much less than for IHE. The degree of embrittlement is the highest in the case of specimens that had internal hydrogen and were tested in hydrogen environment. This is possibly related to the increased grain boundary hydrogen concentration at the fracture location that induces decohesion and the high hydrogen concentrations over large distances that may enhance plasticity.

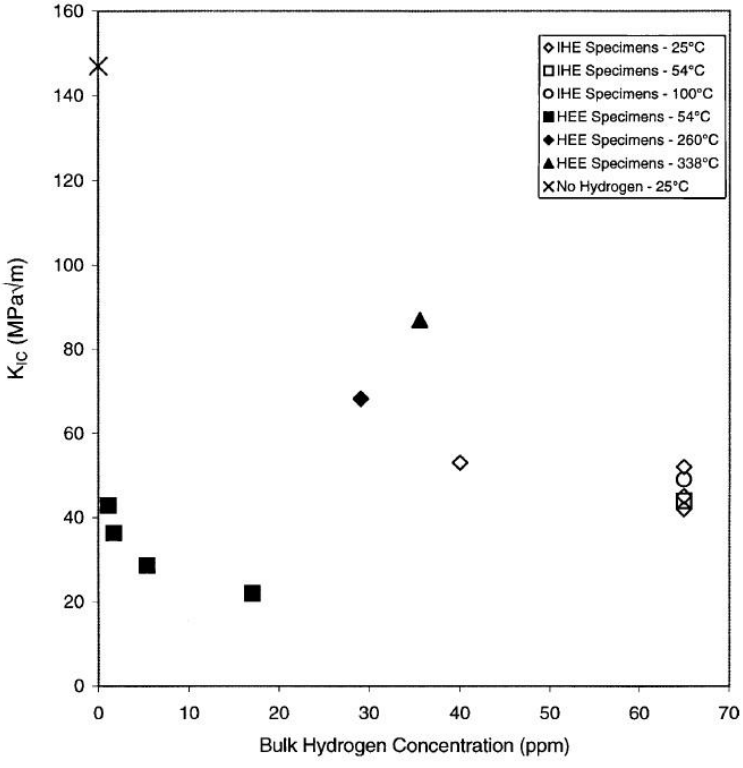

Figure 10. Fracture toughness K_{IC} values for Alloy X-750 specimens tested in IHE (open symbols) and HEE (closed symbols) conditions at high and low temperatures (Symons, 2001).

Grove and Petzold (1985) showed that LTCP does not initiate without presence of a pre-existing flaw or fatigue pre-crack, which was later confirmed also by Mills et al. (1999) who explained it by the greater diffusion distance for hydrogen and less severe stress state. The stress peak position relative to the crack tip is particularly

important. Figure 11 illustrates the difference in the cases of notched and pre-cracked specimens. In notched specimens the distance between the peak stress and the metal-water interface is much larger than in the case of pre-cracked specimens. Therefore, only a small fraction of the hydrogen at the water-metal interface reaches the critical peak stress location due to diffusion loss in the surrounding matrix. In pre-cracked specimens hydrogen concentrates to the stress zone around the crack tip. The concentration of hydrogen can be 3 to 4 times larger than the bulk hydrogen content of the material (Mills et al., 1999).

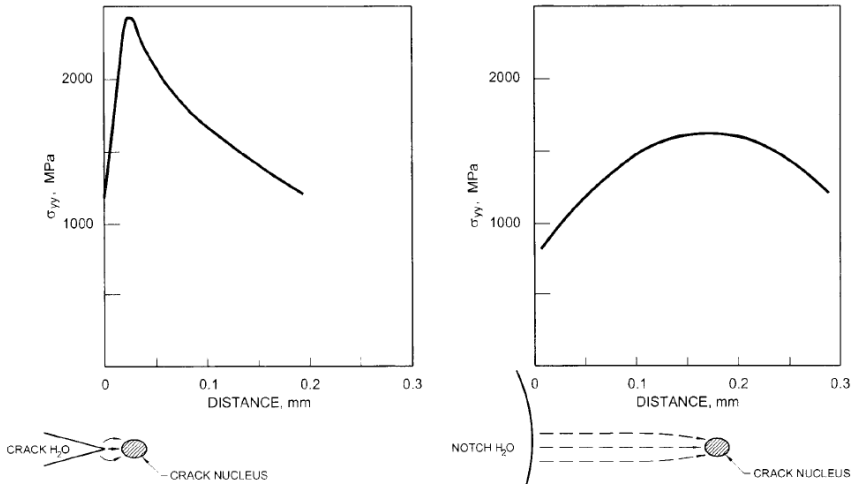

Figure 11. A schematic illustration of the difference between crack and notch regarding LTCP initiation (Mills et al., 1999).

Grove and Petzold (1985) argue that while grain boundary carbides have a strong effect on SCC susceptibility in high temperature water (MC carbides are detrimental because they are strong hydrogen traps, $M_{23}C_6$ carbides are beneficial because they induce compressive stresses and chemical differences at the grain boundaries) the effect of carbides in low temperature water is negligible.

Yonezawa and Onimura (1984) summarized the basic ideas of a few proposed mechanisms for intergranular stress corrosion cracking in high temperature water for nickel-based and iron-based alloys. Theories include ideas based on the effects of grain boundary impurities, Cr-depleted zone, grain boundary precipitate morphology/coherency and grain boundary precipitate free zone. Yonezawa concludes that there is no evidence to support the SCC models for Alloy X-750 that are based on Cr-depleted zone, precipitate free zone and the grain boundary segregation of impurity elements. Instead, SCC susceptibility in deaerated high temperature water seems to correlate well with the morphology and coherency of precipitates along the grain boundaries.

Observations made by Yonezawa and Onimura (1984) on the effects of impurities are somewhat contradictory to what Grove and Petzold (1985) reported. Yonezawa and Onimura compared the segregation of phosphorous at the grain boundaries with SCC susceptibility. Their results indicate that increasing amounts of phosphorous at the grain boundaries increases susceptibility to SCC in both high and low temperature water. A significant number of heats with high grain boundary phosphorous concentrations fail, while heats with low grain boundary phosphorous do not fail. However, not all the studied samples that had high phosphorous concentrations failed. The better SCC resistance of some samples is believed to result from favourable grain boundary microstructure. Thus, Grove et al. believe that the combined effects of grain boundary chemistry and microstructure explain the different SCC performance of the different heat-treated conditions of Alloy X-750 that were investigated in the study.

Grove and Petzold created a following SCC model for Alloy X-750 in low- and high-temperature water: Hydrogen is generated in general corrosion processes. Hydrogen atoms are prevented from combining into molecular hydrogen at the grain boundary surface by a recombination poison phosphorous, which is segregated to the grain boundaries. The concentration of atomic hydrogen builds up to some critical value, whereby the grain boundary cracks. The reasons for the failure may be pressure buildup, decohesion (lowering of the bond strength), formation of brittle hydride and increased local plasticity. Decohesion is assumed to be the most plausible mechanism for the grain boundary failure. Concerning metallurgical aspects, $M_{23}C_6$-type carbides at the grain boundaries are beneficial for lowering the SCC susceptibility, whereas MC-type carbides are harmful. $M_{23}C_6$-type carbides cause compressive stresses and chemical differences at the grain boundaries. MC-type carbides in Alloy X-750 principally contain titanium (TiC), and they are trapping sites for hydrogen. Trapping would increase the mean stay time of hydrogen at failure location and therefore result in earlier SCC. (Grove & Petzold, 1985)

Mills et al. (1999) explained the superior high temperature SCC performance of condition HTH by reduced phosphorous segregation, reduced intergranular gamma-prime, an absence of MC carbides along grain boundaries, a high density of intergranular $M_{23}C_6$ carbides and a large grain size. The gamma-prime phase has two effects: Firstly, it induces hydrogen generation at the cathodic matrix because it is highly anodic. Hosoya et al. (1988) proposed that the galvanic effect between gamma-prime and the matrix can result in extremely local anodic and cathodic process, which can promote accelerated cracking resulting from SCC, hydrogen-assisted cracking (HAC), or a combination of the two. Secondly, gamma-prime is a strong hydrogen trap. The HTH treatment reduces the amount of intergranular gamma-prime and increases the amount of Cr-rich $M_{23}C_6$, which is cathodic with respect to the matrix. (Mills et al., 1999)

Young et al. (2001) studied the effect of service temperature (> 249 °C for ~10 years) hydrogenated water on the low temperature fracture (LTF) of AH heat treated Alloy X-750. Exposure to high temperature water for extended times appears to degrade the LTF resistance of Alloy X-750 in AH condition. The observed

degradation was assumed to be due to an increased hydrogen concentration at grain boundary MC-type carbide trapping sites.

1.4.2 LTCP of Alloys 600 and 690 and their weld metals Alloy 182/82 and Alloy 152/52

The LTCP behaviour of solid-solution strengthened Alloys 600 and 690 and their weld metals has been extensively studied over the past 15 years by Mills and Brown (Brown & Mills 1999, 2002, 2005, 2007; Mills & Brown 1999, 2001; Mills et al. 2001). Their results have later been confirmed by several other researchers (Young et al., 2005; McIlree et al., 2006; Herms et al., 2009; Sakima et al., 2011; Peng et al., 2012; Ahonen et al., 2013, 2014).

The nominal chemical compositions of Alloys 600 and 960, Alloy 182, 82, 152 and 52 weld metals and chemical compositions of the EN82H and EN52 weld metals presented by Brown and Mills (Brown & Mills, 2002; Mills & Brown, 2001) are presented in Table 2. The most important difference between Alloy 600 and Alloy 690 is the Cr content. Alloy 182 and 152 weld metals are used for manual shielded metal arc welding (SMAW) whereas Alloy 82 (EN82H) and Alloy 52 (EN52) weld metals are welded using gas tungsten arc welding (GTAW).

Table 2. Chemical compositions of wrought Alloys 600 and 690 and their weld metals.

	Element												
Alloy	C	Mn	Fe	S	Si	Cu	Ni	Cr	Mo	Al	Ti	P	Nb
600	0.15	1.0	6.0-10.0		0.5	0.5	72.0 min	14.0-17.0					
690	0.05	0.50	7.0-11.0		0.50	0.50	58.0 min	27.0-31.0					
182	0.03	7	5.7	0.007	0.8	0.02	68	16.5			0.1	0.01	1.8
82	0.039	2.98	1	0.004	0.03	0.01	72.6	19.94			0.34	0.001	Nb+Ta 2.47
EN82H*	0.039	2.78	1.34	<0.001	0.092		72.2	20.03			0.33	<0.001	2.39
152	0.048	3.48	10.39	0.003	0.41	<0.01	55.2	28.74	0.01	0.06	0.09	0.003	Nb+Ta 1.54
52	0.03	0.24	9.8	<0.001	0.13	0.04	59.28	29.2	0.03	0.72	0.51	<0.001	Nb+Ta <0.02
EN52**	0.030	0.25	9.77	<0.001	0.17	0.004	58.96	28.89		0.66	0.55	<0.001	Nb+Ta 0.002
	*Material heat "C4 trans." in Brown and Mills 2001												
	**Material heat "C1" in Mills and Brown 2002												

Brown and Mills (Brown & Mills, 1999, 2002; Mills and Brown, 2001) performed fracture toughness (J-R) tests in high pH_{RT} (10.1–10.3) hydrogenated water by using pre-cracked and side-grooved CT specimens (W = 30.5 mm and B = 15.2 mm). The tests materials they used consisted of both hydrogen-precharged and non-precharged specimens and the hydrogen concentration of the water was up to 150 cm^3 H_2/kg H_2O. The effect of loading rate was also studied (from 0.005 to 305 mm/h).

Brown and Mills (1999) observed that EN82H and EN52 welds exhibited very high fracture toughness response in air and 338 °C water in both longitudinal and transverse orientations. The results obtained for longitudinal specimens were higher than those of transverse specimens, which was explained by the orientation of the columnar grains. Crack propagation in transverse direction occurs along the

columnar grains and the boundaries and interdendritic precipitates tended to be aligned in the cracking direction. Also wrought Alloys 600 and 690 exhibited very high fracture resistance J_{IC} values in air and in high temperature water.

In 54 °C water with 150 cm^3 H_2/kg H_2O, the fracture resistance (J_{IC}) of Alloy 600 decreased about 40 % from the value measured in air (Figure 12 (a)) (Brown & Mills, 2001). The tearing modulus (T), which is a measure of the tearing resistance after J_{IC} is exceeded, was virtually unaffected by the environment, thus Alloy 600 was demonstrated to maintain its excellent tearing resistance in low temperature water. However, the fracture resistance of EN82H weld metal was dramatically reduced in the same low temperature environment for both longitudinal and transverse specimens. The fracture resistance was decreased by an order of magnitude or even more. The results for transverse specimens are presented in Figure 12 (b). All the specimens of EN82H weld metal tested in low temperature hydrogenated water showed a marked reduction of fracture resistance values compared to those obtained in air or in high temperature water. The lowest J_{IC} values were 14 and 13 kJ/m^2 for longitudinal and transverse welds, respectively. All 10 J-R test results obtained in 54 °C water showed J_{IC} values clearly below 100 kJ/m^2 (13–79 kJ/m^2). In an earlier study (Brown and Mills, 1999) J_{IC} values of 18 and 114 kJ/m^2 were reported for longitudinal orientation and 18 and 103 kJ/m^2 for transverse orientation of EN82H weld metal. The increase of water temperature to 93 °C did not markedly improve the fracture resistance. However, the fracture resistance of EN82H was restored when the water temperature was increased to 149 °C (Brown & Mills, 2001).

Alloy 690 and its corresponding weld metal EN52 were tested in a similar study (Brown & Mills, 2002) as what was conducted for Alloy 600 and its weld metal EN82H. Alloy 690 was found to be significantly more susceptible to LTCP than the lower Cr Alloy 600, as seen in Figure 12 (c). EN52 welds, studied in longitudinal orientation, also showed a dramatic reduction of fracture resistance in low temperature water. Results for one material heat are presented in Figure 12 (d). However, the J_{IC} values of EN52 are somewhat higher than those measured for EN82H. It was reported earlier (Brown & Mills, 1999) that not all specimens of EN52 showed susceptibility to LTCP. Three of eight specimens fractured in a ductile manner showing little or no effect of low temperature water.

All the specimens that were observed to be susceptible to LTCP showed a transition in fracture mechanism from ductile dimple rupture to intergranular cracking (Brown & Mills, 1999, 2001, 2002). This transition was found to occur in Alloy 690 and weld metals EN82H and EN52 but not in Alloy 600 which retained its high toughness and tearing resistance in low temperature water.

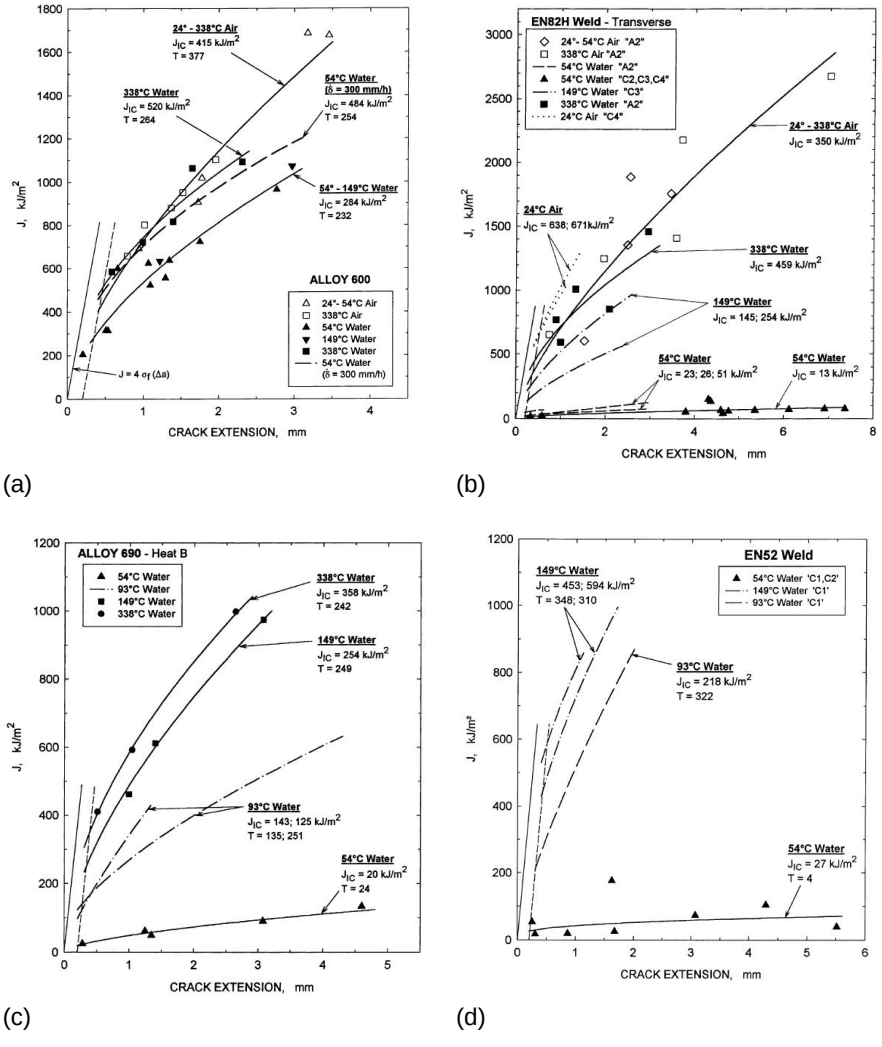

Figure 12. Fracture resistance (J-R) curves for Alloy 600 (a), EN82H weld metal (b) (Mills & Brown, 2001), Alloy 690 (c), and EN52 weld metal (d) (Brown & Mills, 2002) tested in air, high temperature water and low temperature water.

Shoji et al. criticized the results by Brown and Mills (2002) for Alloy 690 (Shoji et al., 2007). The materials that were used by Brown and Mills were different regarding the chemical composition and microstructure than the materials that Shoji et al. used for their tests. Especially Ti and Al contents were significantly higher in the material used by Brown & Mills. Yonezawa (2008) presented estimated J-R curve data for Alloy 690TT that shows that the Japanese material (690TT) is far less susceptible to environmental effect of hydrogenated low temperature water than

what Brown and Mills observed for their material (Figure 13). The inhomogeneous microstructure of Brown and Mills' Alloy 690 material, that included large primary carbides, was especially criticised. The large intergranular primary carbides are not present in the material used by Yonezawa. The reason for the occurrence of the large primary carbides, in addition to differences in chemical compositions, is believed to be a very short annealing time used in Brown and Mills' study (1074 °C for 5 min, air cooled) for a 76,2 mm diameter bar.

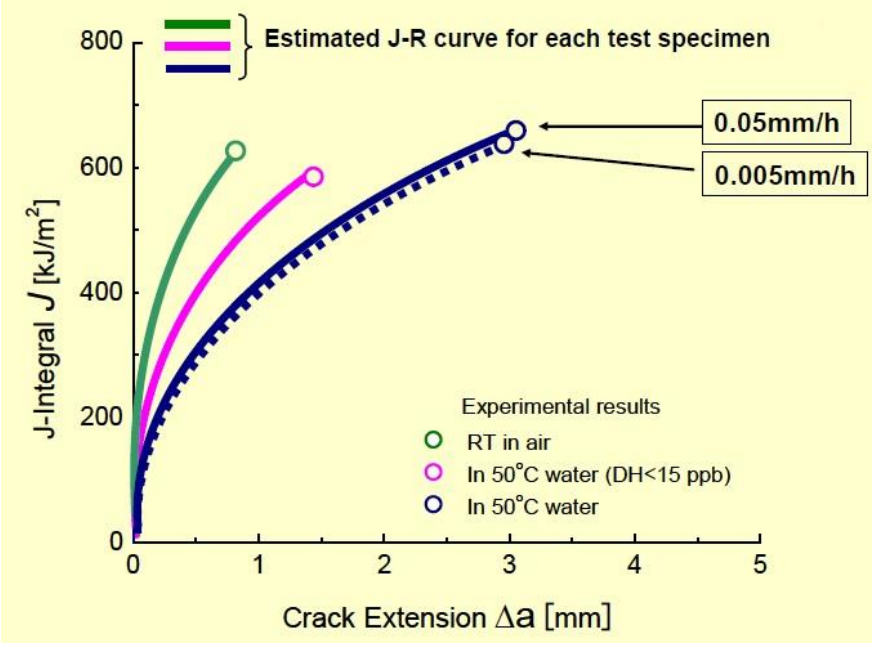

Figure 13. Estimated J-R curves for Alloy 690TT tested in air and in low temperature water with high (blue curve) and low (purple curve) hydrogen contents (Yonezawa, 2008).

The effect of loading rate on the fracture toughness behaviour was also studied by Brown and Mills (2001, 2002). They perceived that the fracture resistance is virtually unaffected by the loading rate, when the loading rate for the CT specimens was up to 1.3 mm/h (100 $MPam^{1/2}$/h). At a loading rate 15 mm/h (1000 $MPam^{1/2}$/h) the tested materials behaved in a ductile manner.

The results obtained by Young et al. (2005) confirm the results published by Brown and Mills for Alloy 82 weld metal. In addition, their results for Alloy 182 weld metal show a similar response to the low temperature hydrogenated water. McIlree et al. (2006) studied also the behaviour of Alloy 152 in addition to Alloy 182. They observed that the fracture resistance of Alloy 152 was also affected by hy-

drogenated water. The reduction of J_{IC} value was quite similar in both studied alloys but Alloy 152 retained its high tearing resistance in hydrogenated water. In that study different hydrogen concentrations were also applied in order to research the effect of hydrogen content of the low temperature water. It was observed that the fracture resistance and tearing modulus values were both decreased for Alloy 182 when the hydrogen content of the low temperature water was increased. In fact, Alloy 182 showed a clear reduction (~1/3 decrease) of fracture resistance in low temperature water even with no dissolved hydrogen. Hydrogen content 10 cm^3 H_2/kg H_2O further slightly decreased the fracture resistance. The results for Alloys 182 and 152 by McIlree et al. are presented in Figure 14. The tearing resistance of Alloy 152 was not significantly affected by addition of hydrogen, although the fracture mechanism clearly changed to intergranular cracking, when the specimens were tested with hydrogen contents 30 cm^3 H_2/kg H_2O and higher. With low hydrogen contents no intergranular cracking was observed in Alloy 152. The fracture surface appearance after testing in low temperature water with 30 cm^3 H_2/kg H_2O is presented in Figure 14 a) and b) for Alloys 182 and 152, respectively. Alloy 182 exhibits extensive intergranular (or possibly interdendritic) cracking whereas Alloy 152 has a clearly more ductile appearance with large areas consisting of dimples and only some areas that are purely intergranular fracture.

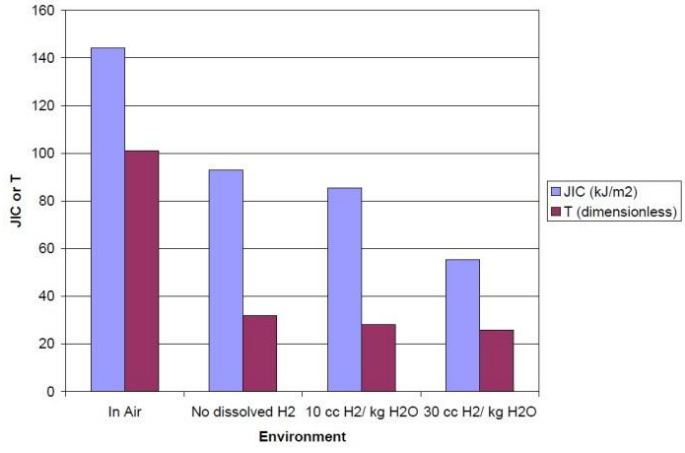

a)

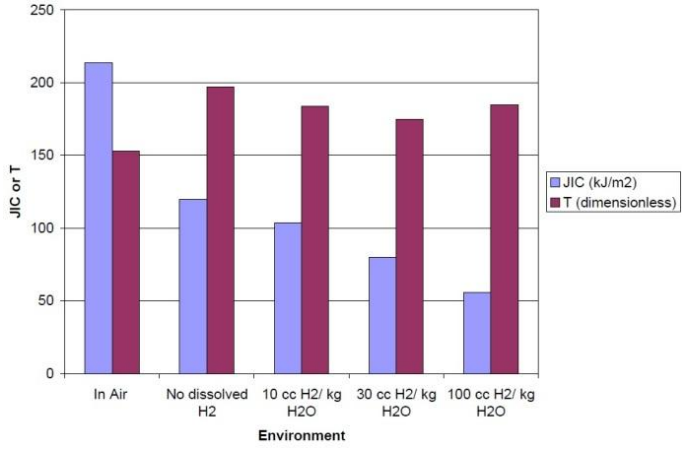

b)

Figure 14. J-R test resuts (J_{IC} and T values) obtained by McIlree et al. (2006) for Alloys 182 a) and 152 b) in low temperature water with varying hydrogen contents.

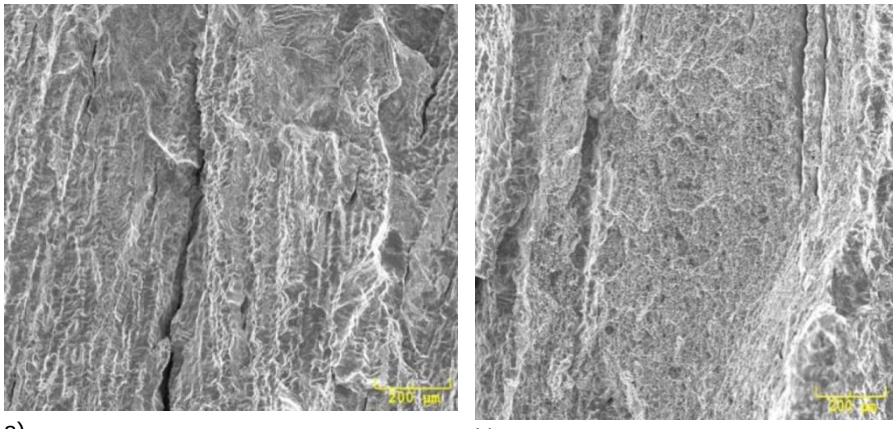

a) b)

Figure 15. SEM images of the fracture surfaces of Alloys 182 a) and 152 b) after J-R testing in low temperature water with hydrogen content 30 cm^3 H_2/kg H_2O (McIlree et al., 2006).

Herms et al. (2009) observed that the fracture resistance of Alloy 182 is decreased even at very low hydrogen contents (3–5 cm^3 H_2/kg H_2O) of the water. The fractographic examinations showed that the observed decrease of fracture resistance at low hydrogen content of the water was associated with intergranular cracking.

1.4.2.1 Sources of hydrogen

Hydrogen that is present in materials of nuclear power systems is originated from three primary sources that include (Young et al., 2012):

1) Hydrogen from fabrication, i.e. from welding or heat treating in hydrogen bearing atmospheres
2) Corrosion generated hydrogen
3) Gaseous hydrogen added to the cooling water

The nickel-based alloys are usually welded using shield gas that consists mostly of argon. Some hydrogen is sometimes added in order to decrease the amount of oxidization and to increase the voltage of the arc which in turn increases the welding temperature. Young et al. (2003) measured the bulk hydrogen contents of EN82H welds after welding using 0–5 % hydrogen in the shielding gas and in addition to that a shielding gas consisting of helium and argon (75 and 25 %, respectively). The hydrogen concentration of as-welded EN82H depends on the shielding gas, as shown in Figure 16. Hydrogen concentrations range from ~12.5 wt. ppm in 95% Ar/5 % H_2 weld to ~3.5 wt. ppm in the 75% He/25 % Ar weld.

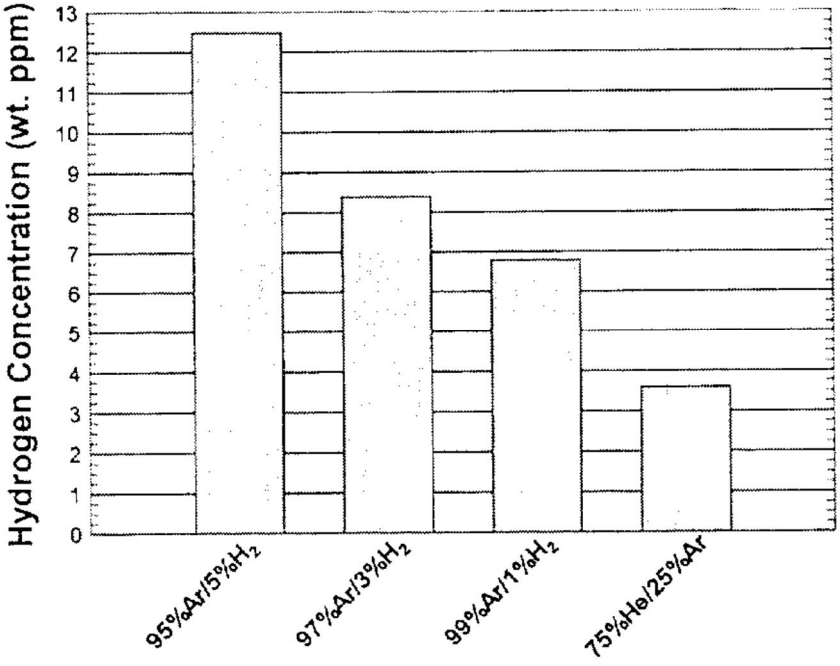

Figure 16. Bulk hydrogen contents of EN82H welds after welding using different shielding gases containing 0-5 % hydrogen (Young et al., 2003).

1.4.2.2 Hydrogen trapping

Hydrogen trapping may have a crucial effect on LTCP behaviour of nickel-based alloys where various types of inclusions and carbides are present (Mills et al., 2001). Different material defects can act as either hydrogen traps or hydrogen repellers (Pressoyre, 1983). Hydrogen traps can be divided in two categories: attractive traps and physical traps. Attractive traps are regions of the lattice where hydrogen atoms are subjected to an attractive force of various origins such as electronic force, tensile stress field, thermal gradient or chemical potential gradient. Physical traps are caused by physical discontinuities of the parent lattice. A physical discontinuity may create a location where it is more energetically favourable for hydrogen to stay (Pressoyre, 1983).

Yonezawa et al. (1993) studied the distribution of hydrogen and the microstructure of grain boundary precipitates by using electron micro audiographic technology. The studied material was Alloy X-750 in two different heat treatment conditions that were:

1) 1080 °C for 1 h, water cooled and 715 C for 16 h, air cooled

2) 982 °C for 1 h, air cooled and 719 °C for 16 h, air cooled.

These heat treatments resulted in different grain boundary carbides. The carbides in the first heat treatment condition were semi-continuous coherent $M_{23}C_6$ carbides, and in the second heat treatment condition discrete incoherent Cr carbides. The coherency of the carbides was observed to be important considering the IGSCC susceptibility of Alloy X-750 in SSRT test since only the material with incoherent carbides showed IGSCC susceptibility in hydrogenated (up to 40 cm^3 H_2/kg H_2O) high temperature simulated PWR water. The measured hydrogen content of the fractured material was up to 43 ppm close to the fracture surface of the SSRT specimen. The conclusion of Yonezawa et al. is that the incoherent precipitates trap more hydrogen and thus the precipitation conditions on grain boundaries dominate IGSCC susceptibility.

1.4.2.3 Hydrogen-induced degradation mechanisms

Oriani (1993) has reviewed the literature covering the proposed mechanisms for hydrogen-induced fracture. According to Oriani, the most important factor is the ability of dissolved hydrogen to lessen the binding forces between metal atoms. This will lead to easier propagation of a cleavage crack, or by reduction of the force needed for continuous emission of edge dislocations from the tip of a crack leading to easier crack propagation by localized plasticity. Hydrogen at low concentrations in pure Ni, α-Fe, α-Ti and Nb decreases the flow stress. Impurities change the response drastically. Large concentrations of hydrogen in Ti, Ta, V and Nb produce brittleness because the hydrides that are formed resist dislocation motion.

Birnbaum and Sofronis (1994) state that there are several mechanisms that aspire to explain hydrogen-related fracture phenomena. According the Birnbaum and Sofronis, three mechanisms are the most plausible: stress-induced hydride formation and cleavage, hydrogen-enhanced localized plasticity (HELP) and hydrogen-induced decohesion. HELP mechanism is based on the idea that the presence of hydrogen in solid solution decreases the barriers to dislocation motion, thereby increasing the amount of deformation that occurs in a localized region adjacent to the fracture surface. Hydrogen effects in microscopic scale based on observations obtained in various in situ TEM studies performed at about 290 K, which allows the observation of the fracture process in real time. Those studies have been performed for different bcc, fcc and hcp -structured metals covering various solid solutions and precipitations. According to these studies, hydrogen increases the dislocation mobility under conditions of constant stress. Enhanced dislocation velocities were observed on {112} and {110} slip planes of steel. In addition, hydrogen-enhanced operation of dislocation sources was observed within the crystals and at grain boundaries. Fractographic examinations also showed that plastic deformation occurs at regions close to the fracture surface when the specimen was stressed under hydrogen gas. It was also observed that when a crack stopped after some propagation in vacuum, it continued to grow when hy-

drogen gas was added to the environment. Hydrogen locally softens the material in front of the crack and thus enables the ductile crack growth to continue. However, the observations of softening in microscopic scale are contradictory to the macroscopic behaviour, because hydrogen charging has been reported to result in increased flow stress and only in a small number of cases has softening been observed. There are two things that are believed to explain this behaviour. Firstly, cathodic charging may introduce high hydrogen concentration gradients and correspondingly high stresses near the surface. The consequent hardening of the surface region may mask the softening caused by hydrogen. Secondly, it has been observed in the case of steels and nickel, that hydrogen induces localization of slip on a limited number of slip planes. An inhomogeneous distribution of hydrogen can cause shear localization which can cause significant hardening and increase of flow stress even in the presence of reduced barriers to dislocation motion.

Nibur et al. (2006, 2009) studied the effect of dissolved hydrogen on the deformation of small volumes of the austenitic stainless steel 21Cr–6Ni–9Mn by using nanoindentation examinations. Nanoindentation results show that homogeneous nucleation of circular dislocation loops is enhanced in the presence of hydrogen. It is further shown that this is likely due to hydrogen reducing the shear modulus of the material.

Sirois and Birnbaum (1992) studied the effects of hydrogen and carbon on thermally activated deformation in nickel. Angelo et al. (1995) point out that the results by Sirois and Birnbaum regarding hydrogen effect on dislocation movement measured using thin foils of pure nickel are controversial to a study performed for bulk nickel-based alloy IN903 specimens by Moody et al. (1993). Moody et al. observed that there is no difference in dislocation dynamics when the material is charged with hydrogen, whereas the results from the study by Sirois and Birbaum show that the activation enthalpy for dislocation slip in pure nickel decreases with increasing hydrogen content. Hence, there is still a lack of consensus regarding the viability of the HELP mechanism.

LTCP is widely considered to be a hydrogen-related degradation phenomenon. Brown and Mills (2002) suggest that the intergranular cracking in the case of LTCP is probably due to hydrogen-induced decohesion process, originally presented by Troiano (1960), whereby hydrogen decreases cohesive strength and promotes failure along specific crystallographic planes.

1.5 LTCP risk in nickel-based materials

Mills & Brown (1999) have proposed a classification for LTCP risk assessment in nuclear power plants based on fracture resistance J_{IC} and tearing resistance T values. The highest risk category is for materials that exhibit J_{IC} values lower than 30 kJ/m^2 and T below 10. At these toughness levels fracture may occur even below yield stress loadings with relatively small flaw sizes and linear-elastic frac-

ture mechanics assessment should be included for design and operational analyses. For materials, whose J_{IC} values range from 30 to 150 kJ/m^2 and T between 10 and 100, stable or unstable fracture can occur at approximately yield strength loadings for components containing small or intermediate flaw sizes and fracture control based on fracture mechanical analyses (elastic-plastic fracture mechanics methods) should be considered. For materials, that exhibit J_{IC} greater than 150 kJ/m^2 and T above 100, conventional stress limits are adequate for guarding against fracture.

LTCP risk in PWR plants has been evaluated by Demma et al. (2005). Demma et al. point out that LTCP is unlikely to occur during PWR shutdown because such situation where pressure, hydrogen addition and low temperature exist simultaneously is avoided. Cronvall (2011) showed in a structural integrity analysis based study that the critical crack size for Alloy 182 would be slightly more than 50 % of the wall thickness that was assumed to be 40 mm. Large cracks would most probably be observed in non-destructive examinations (NDE) before reaching such size. On the other hand, if J_I values of a crack reach the corresponding J_{IC} value under LTCP conditions, the resulting crack growth could be fast and lead to a leaking crack before the next inspections.

1.6 Basics of elastic-plastic fracture mechanics

Linear elastic fracture mechanics (LEFM) is valid only as long as nonlinear material deformation is confined to a small region surrounding the crack tip. In many ductile materials, including nickel-based alloys, it is virtually impossible to characterize the fracture behaviour with LEFM, and an alternative fracture mechanics model is required. Elastic-plastic fracture mechanics applies to materials that exhibit time-independent, nonlinear behaviour (i.e., plastic deformation) (Anderson, 2005). Fracture resistance behaviour of austenitic materials can be studied e.g. by applying J-R testing.

1.6.1 J-Integral

J-integral represents a way to calculate the energy release rate per unit fracture surface area in a material. J-integral for a variety of configurations can be written as follows (Anderson, 2005):

$$J = \frac{\eta U_c}{Bb} \tag{4}$$

where η is a dimensionless constant (η=2 for a deeply cracked plate in pure bending), U_c is the absorbed energy, B is the specimen thickness and b is the unbroken ligament size. Thus, the equation (2) expresses J as the energy absorbed, divided

by the cross-sectional area, times a dimensionless constant. Equation (2) can be separated into elastic and plastic components:

$$J = \frac{\eta_{el} U_{c(el)}}{Bb} + \frac{\eta_p U_p}{Bb} \tag{5}$$

$$= \frac{K_I^2}{E'} + \frac{\eta_p U_p}{Bb} \tag{6}$$

where $E' = E$ for plane stress and $E' = E/(1 - \nu^2)$ for plane strain. (Anderson, 2005)

1.6.2 Fracture resistance curve

Fracture resistance curve (J-R curve), is an illustration of fracture behaviour of a test specimen where J-integral is plotted as a function of crack propagation (Δa). The different stages of the fracture are schematically presented in Figure 17. When a specimen is loaded crack blunting begins to occur. Crack growth initiates at a stage where the *dJ/da* of the J-R curve begins to decrease, as illustrated in the schematic figure. The ASTM 1820 – 01 standard defines J_{IC}, a specimen size independent value of fracture toughness, as a value of J-integral where the 0.2 mm blunting line crosses the J-R curve. That is nominally the onset of stable crack growth, i.e. the moment when the crack growth initiates.

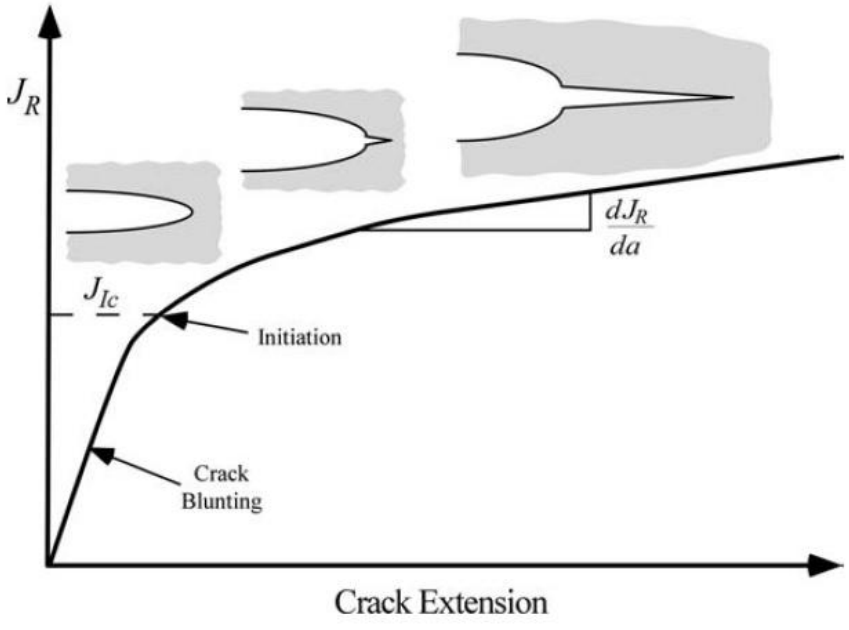

Figure 17. A schematical illustration of the different stages of fracture during a J-R test (Anderson, 2005).

2 Objectives of the study

The aim of this study was to perform different experiments that can be used to evaluate the LTCP behaviour of nickel-based alloy welds. The experimental methods selected for the study include J-R tests, microscopy, chemical analyses and hydrogen thermal desorption spectrometry. J-R tests were conducted in order to determine the fracture resistance behaviour of the studied materials in low temperature hydrogenated water. Different types of microscopy and chemical analyses were utilized for microstructural characterization of the fracture surfaces of J-R test specimens and cross-sections of the welds. Thermal desorption spectroscopy was applied in order to study the hydrogen trapping behaviour of the studied materials. Electron microscopy (SEM and TEM) was concentrated on the grain boundary structures, especially carbide structures, which provide information on the possible hydrogen trapping sites.

Some factors that may have an effect on the fracture toughness behaviour of nickel-based alloy welds have not been extensively studied thus far. These factors involve the effect of high temperature (300 °C) pre-exposure and the effect of post-weld heat treatment on the LTCP behaviour of the dissimilar metal welds. The effects of these factors are studied for the DMW materials.

3 Materials

Two types of materials have been used to manufacture the SE(B) test specimens for J-R testing, i.e., all-weld metal blocks and dissimilar metal weld mock-ups. All-weld metal blocks were fabricated by welding Alloy 182, 82, 152 and 52 weld metals on crossed steel bars. In DMW mock-ups the studied weld metals consist of Alloys 182, 152 and 52. The coupons for thermal desorption spectroscopy were extracted from DMW mock-ups from the mid-thickness of the weld.

3.1 All-weld metal test blocks

The SE(B) test specimens of all-weld metals, i.e., Alloy 182, Alloy 82, Alloy 152 and Alloy 52, were cut from the samples presented in Figure 18. The samples were fabricated by welding multiple beads on crossed steel bars, as presented in Figure 19 a). Welding parameters when welding the test blocks were according to the filler material manufacturer recommendations. The SE(B) specimens for J-R tests were extracted as illustrated in Figure 19 b). The compositions of the all-weld metal test blocks are identified in Table 3. The UNS standard compositions according to Special Metals for the corresponding weld filler metals are presented in Table 4. Compositions of the all-weld metals are within standard specifications, except for the Fe contents of Alloy 82 and 152 that are slightly high (4 and 13 %, respectively), and for the Mn content of Alloy 82 () that is also a little higher than in the standard composition. Welding was carried out manually without post-weld heat treatment.

Figure 18. All-weld metal test blocks of Alloy 82, Alloy 182, Alloy 52 and Alloy 152, respectively.

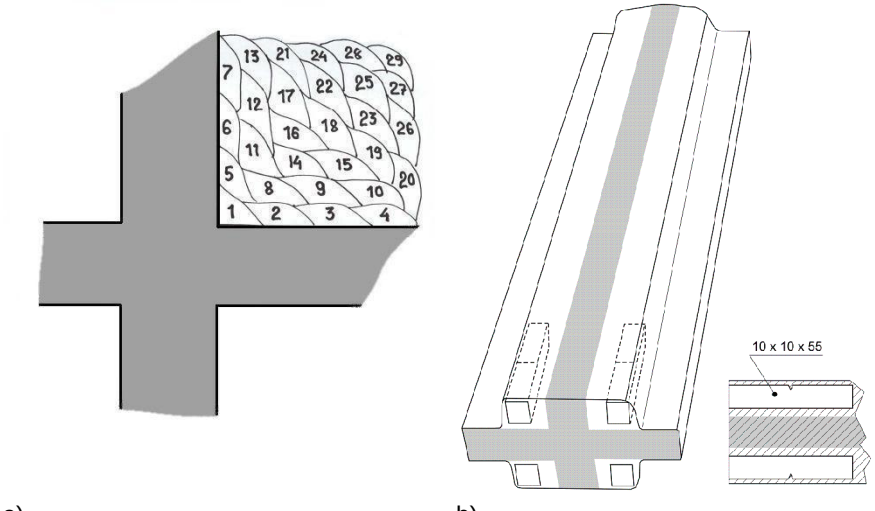

a) b)

Figure 19. Welding sequence of the all-weld metal test block Alloy 182 in a) and a schematic illustration that shows extracting of the specimens from the test blocks in b).

Table 3. Chemical compositions of the all-weld metal test blocks (in weight %) (Hänninen et al., 2007).

Element	Alloy 182	Alloy 82	Alloy 152	Alloy 52
Cr	15.6	19.5	28.1	28.7
Fe	9.1	4	13	10.3
Cu	0.01	0.01	0.01	0.01
Al	0.02	0.06	0.06	0.84
Co	0.02	0.01	0.03	0.04
Nb	2.1	2.9	2.2	0.04
Mo	0.05	0.02	0.05	0.03
Ti	0.01	0.2	0.01	0.58
Mn	6.5	3.6	5	0.33
Si	0.7	0.13	0.39	0.22
S	0.002	0.002	0.002	0.002
P	0.002	0.002	0.002	0.002
C	0.02	0.02	0.02	0.02
Ni	Bal.	Bal.	Bal.	Bal.

Table 4. Chemical compositions of the weld filler metals (in weight %) (according to Special Metals).

	Alloy (UNS)			
Element	182 (W86182)	82 (N06082)	152 (W86152)	52 (N06052)
C	0.10 max.	0.10 max.	0.05 max.	0.04 max.
Mn	5.0-9.5	2.5-3.5	5.0 max.	1.0 max.
Fe	10.0 max.	3.0 max	7.0-12.0	7.0-11.0
S	0.015 max.	0.015 max.	0.015 max.	0.015 max.
Si	1.0 max.	0.5 max.	0.75 max.	0.50 max.
Cu	0.50 max	0.50 max	0.50 max	0.30 max.
Ni+Co	59.0 min.	67.0 min.	Bal.	Bal.
Cr	13.0-17.0	18.0-22.0	28.0-31.5	28.0-31.5
Mo	-	-	0.50 max.	0.50 max.
Al	-	-	0.50 max.	1.10 max.
Ti	1.0 max.	0.75 max.	0.50 max.	Al+Ti 1.5 max.
P	0.030 max.	0.030 max.	0.03 max.	0.02 max.
Nb+Ta	1.0-2.5	2.0-3.0	1.0-2.5	0.10 max

3.2 Dissimilar metal weld (DMW) mock-up test blocks

DMW mock-up materials were manufactured using Alloy 182, Alloy 152 and Alloy 52 weld metals. The cross-section images of the mock-ups, named Aalto 182 (Alloy 182), KAIST (Alloy 152) and Aalto NGW (Alloy 52), are presented in Figures 20–22. The welding procedures of Aalto 182 and Aalto NGW mock-ups are reported in Hänninen et al. (2014).

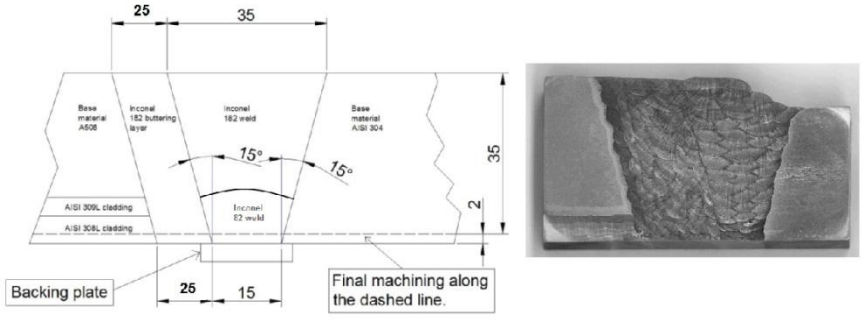

Figure 20. A schematic drawing of weld cross-section of test block Aalto 182 mock-up (Alloy 182) on the left, and a photograph taken from the actual polished and etched cross-section on the right.

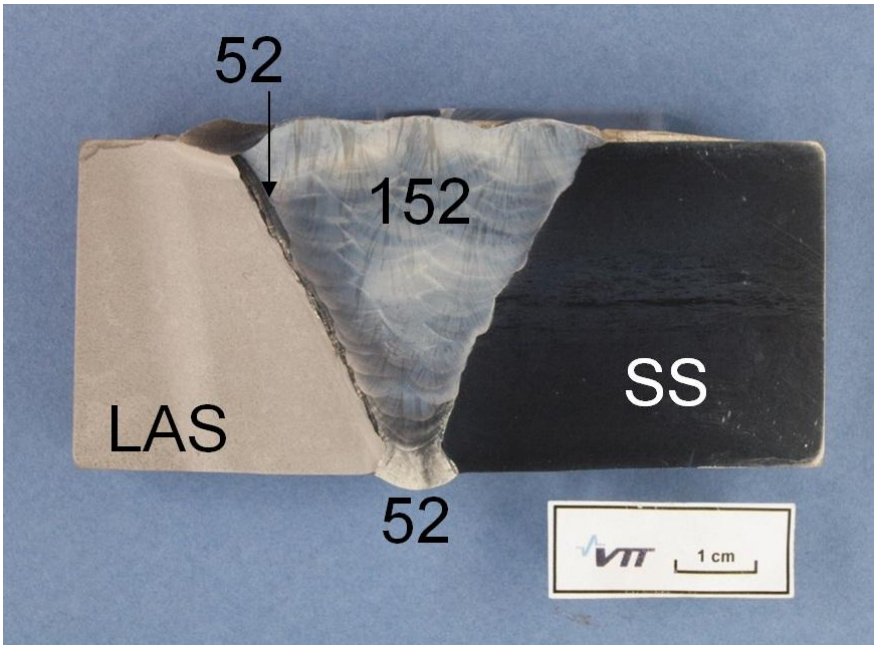

Figure 21. A photograph of KAIST mock-up (Alloy 152) test block cross-section (polished and etched) showing low alloy steel and stainless steel base materials, Alloy 52 butter and root and Alloy 152 weld.

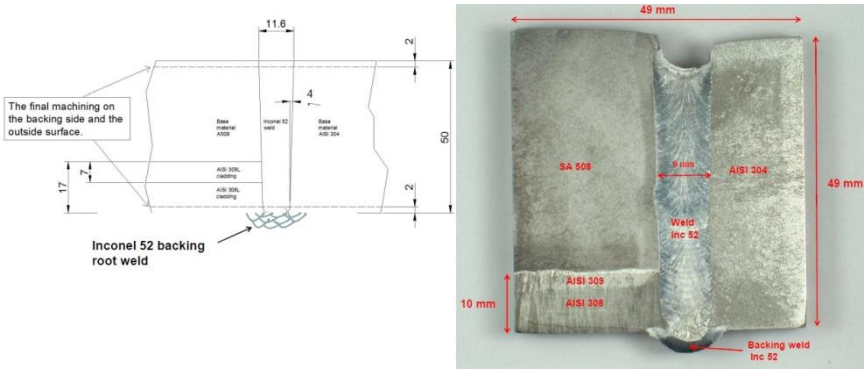

Figure 22. A schematic drawing of weld cross-section of test block Aalto NGW mock-up (Alloy 52) on the left, a photograph taken from the actual polished and etched cross-section on the right.

4 Methods

4.1 J-R tests

The fracture toughness tests were performed using pneumatic servo-controlled loading device and the crack growth was measured using potential drop (PD) method. The J-R curves were calculated according to the standard test method for measurement of fracture toughness, ASTM E 1820 – 01.

There are several criteria that the test has to meet in order to be a valid J-R test according to the ASTM 1820 - 01 standard. In the case of inhomogeneous materials the requirements of crack front evenness are not always met. In addition, the acceptable specimen size is dependent on the toughness and flow stress of the material. In this study the crack front evenness was not always met. The size criteria were almost always met excluding some specimens where the fracture resistance was measured to be above 200 kJ/m^2. The chosen loading rate was also slower than the standard requires. Since the specimens do not always meet all the requirements of the standard, the results obtained from the fracture toughness testing are reported as fracture resistance J_Q instead of fracture toughness J_{IC}, which is, according to the ASTM 1820 – 01 standard, a size-independent value of fracture toughness. Tearing resistance ($T_{0.5mm}$) has been calculated at the crack growth (Δa) 0.5 mm using the equation (7):

$$T = \frac{E}{\sigma_0^2}\left(\frac{dJ}{da}\right) \tag{7}$$

where σ_0 is the flow stress of the material. The flow stress was calculated from yield and tensile strength values that were specified for Alloy 182, 82, 152 and 52 weld metals in the reference by Hänninen et al. (2007).

The crack growth 0.5 mm was chosen because most of the curves that reached the 0.2 mm blunting line also reached the crack growth of 0.5 mm. In addition, the Δa value 0.5 mm was considered appropriate here for 10 x 10 x 55 mm SE(B) specimens since for example Mills & Brown (1999) measured the *T* value at Δa=1.3 mm by using significantly larger CT specimens (W=30.5 mm and B=15.2 mm).

An in-house Cracklength software, which calculates the crack length according to the ASTM E 1820 standard using nine measurements from the crack plane, was used to determine the crack lengths as shown in Figure 23.

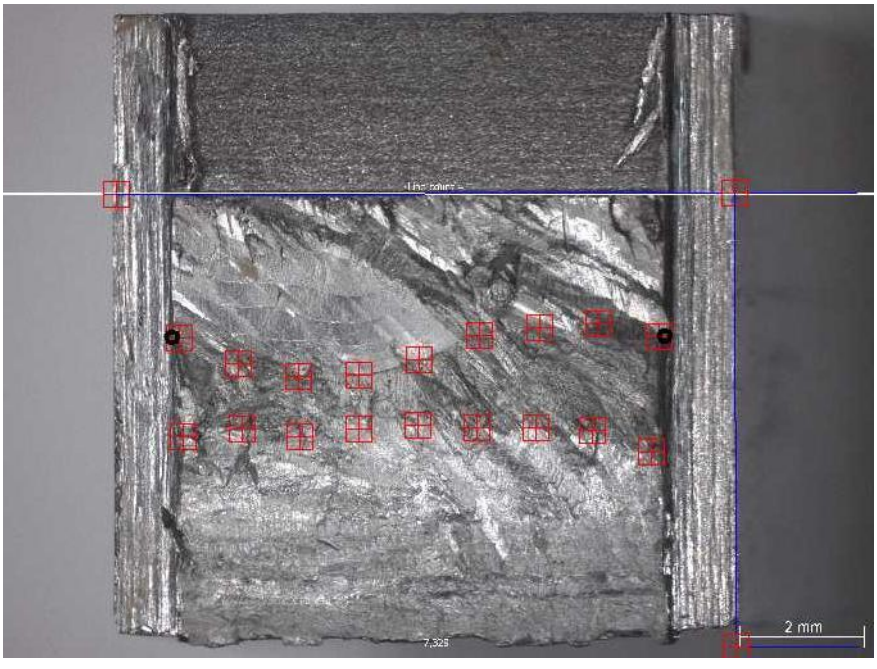

Figure 23. An example of crack length measurement by using Cracklength software.

4.1.1 J-R test specimens

The specimens were cut from the test blocks presented in Figure 18 (all-weld metal test blocks Alloy 182, 82, 152 and 52) and Figures 20–22 (Aalto 182 mock-up Alloy 182, KAIST mock-up Alloy 152 and Aalto narrow gap weld (NGW) mock-up Alloy 52). The specimens were extracted from the DMW mock-ups so that the

notch and fatigue pre-crack located approximately in the middle of the weld. All the specimens were machined, fatigue pre-cracked to nominal 0.5 a/W and 20 % side grooved. The size of the specimens was 10 x 10 x 55 mm.

1 x 1 mm slits for PD leads were machined to each specimen in both ends of the specimen and on both sides of the notch. The distance of the leads from the crack plane was 2 mm. Following specimen orientations were used: L-S for all-weld metal specimens of Alloys 182, 82, 152 and 52, and T-S for dissimilar metal weld specimens of Alloys 182, 152 and 52. The orientations are explained in Figure 24. The different orientations were used in order to get a sufficient amount of specimens from available test blocks.

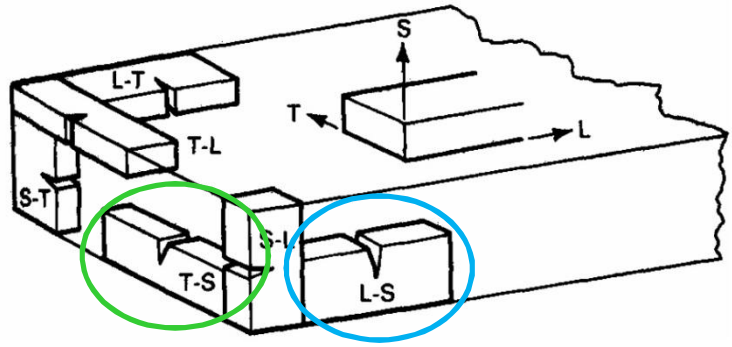

Figure 24. Schematic picture showing specimen orientations: longitudinal (L), width (T) and short transverse (S). Longitudinal direction (L) corresponds to the welding direction. The orientations used in this study are circled with green (DMW specimens) and blue (all-weld metal specimens) (ASTM E 1823-96).

4.1.2 Environments and loading

Fracture toughness tests were conducted in room temperature air and in an autoclave with and without pre-exposure in hydrogenated water. The specimens were assembled to a specimen holder, and the clearance between a specimen and a bellows was originally set to be approximately 0.01 mm. The PD wires of the specimens were welded to the wires of the PD measurement equipment.

For the environmental tests, about 15 l of pure water containing boric acid (200 ppm) and lithium hydroxide (2.1 ppm) additions (pH 7.4) was put into the autoclave and heated to the temperature of 55 °C. This boric acid concentration was chosen because it corresponds to a typical PWR shutdown water chemistry. Two target levels of hydrogen concentration were chosen, 100 and 30 cm^3 H_2/kg H_2O, and the hydrogen content was measured during the test for tests with 30 cm^3 H_2/kg H_2O. For tests with 100 cm^3 H_2/kg H_2O the hydrogen content of the water

was evaluated from the hydrogen partial pressure by applying Henry's law. The actual hydrogen contents during the tests were estimated to be within ± 2-3 cm^3 H_2/kg H_2O from the target levels for the tests with 30 cm^3 H_2/kg H_2O and within ± 10 cm^3 H_2/kg H_2O for the tests with 100 cm^3 H_2/kg H_2O. Hydrogen content 30 cm^3 H_2/kg H_2O was chosen because it is a typical hydrogen concentration of PWR water in normal operation. Hydrogen content 100 cm^3 H_2/kg H_2O was used in order to demonstrate the effect of hydrogen on the fracture resistance. All the hydrogenated water tests were performed at the temperature of 55 °C, which was chosen because literature data is mostly attained at the same temperature and the LTCP effect is the most severe below about 65 °C (Young et al., 2012).

The effect of pre-exposure at high (operation) temperature was investigated by performing test series in which the autoclave temperature was elevated to 300 °C and maintained for 24 hours or 30 days prior to testing, and then cooled to the testing temperature 55 °C. The temperature during the different stages of the 24 h pre-exposure and during the actual J-R –test is presented as a function of time in Figure 25. The hydrogen content in the pre-exposure test series was set to be 100 cm^3 H_2/kg H_2O at 55 °C. The 30 days pre-exposure test followed a similar temperature sequence with the exception of longer high temperature hold time and slightly faster cooling that lasted about 11 hours.

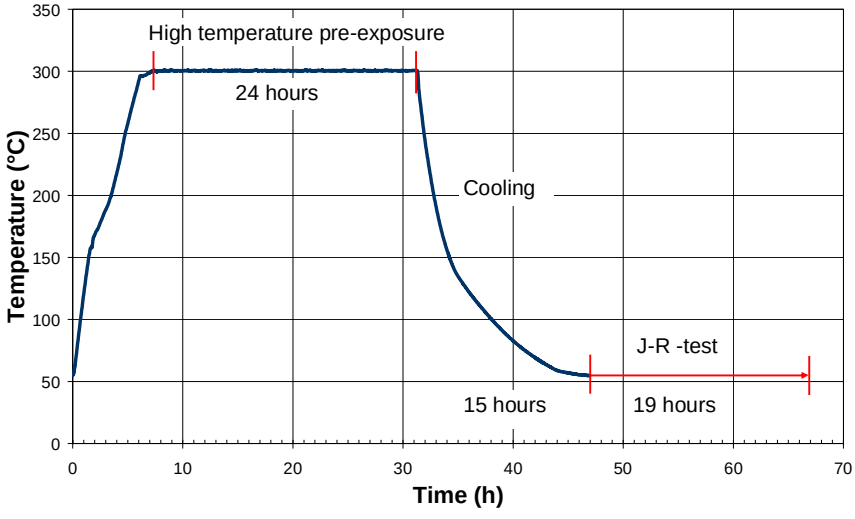

Figure 25. Temperature sequence in the pre-exposure test series where the high temperature hold time was 24 h.

Loading rate was 0.1 mm/h in every test series, and the duration of a test was approximately 19 hours. The loading rate was chosen based on the research of

Mills and Brown (2001), so that the rate is clearly slower than the threshold rate, 1.3 mm/h, proposed for CT-specimens (W = 30.5 mm, B = 15.2 mm) of Alloy EN82H, which corresponds to $\dot{K}$=100 MPa $m^{1/2}$/h. In the case of SE(B) specimens of Alloy 182, 82, 152 and 52 weld metals, the chosen rate corresponds to $\dot{K}$ values in the range of 24–31 MPa $m^{1/2}$/h. The features affecting the $\dot{K}$ value, which is constant over the linear part of a constant displacement rate test, are the stiffness and the initial crack length of a specimen. The chosen loading rate is slower than the ASTM E 1820 – 01 standard rate for SE(B) specimen testing. The standard limits the time to reach the load P_f between 0.1 and 10.0 min, and in these tests the corresponding time was approximately 40 min. The load P_f is defined as:

$$P_f = \frac{0.5Bb_0^2\sigma_Y}{S} \tag{8}$$

4.1.3 Post-weld heat treatments

Post-weld heat treatment was performed for some samples extracted from NGW Alloy 52 and Aalto Alloy 182 mock-ups. Heat treatment for specimens of NGW Alloy 52 mock-up was 550 ± 15 ˚C for 17.1 h following 610 ± 15 ˚C for 7.4 h. Heat treatment for specimens of Aalto Alloy 182 was 615 °C for 6 h.

4.1.4 Test matrix for J-R tests

The test matrix consisting of successful tests conducted in low temperature water is presented in Table 5. Some of the performed tests were unsuccessful due to problems that occurred with measurements. Reference tests for Alloy 182, 82, 152 and 52 weld metals were also performed in air in addition to environment tests, that are listed in Table 5.

Table 5. Test matrix for J-R tests conducted in low temperature water. “cc” in the “Pre-exposure” column corresponds to cm^3 H_2/kg H_2O.

Material	AW/PWHT	Pre-exposure at 300 °C	Hydrogen content (cm^3 H_2/kg H_2O)	Number of successful tests
All-weld metal 182	AW	-	100	2
All-weld metal 182	AW	-	30	2
All-weld metal 182	AW	24 h 100 cc	100	3
Aalto 182	AW	-	30	2
Aalto 182	AW	30 days 30 cc	30	2
Aalto 182	PWHT	-	100	3
Aalto 182	PWHT	-	30	3
All-weld metal 82	AW	-	100	3
All-weld metal 82	AW	-	30	2
All-weld metal 82	AW	24 h 100 cc	100	3
All-weld metal 152	AW	-	100	2
All-weld metal 152	AW	-	30	2
KAIST 152	AW	-	100	2
KAIST 152	AW	-	30	4
KAIST 152	AW	-	5	3
KAIST 152	AW	-	0	2
KAIST 152	AW	30 days 30 cc	30	2
KAIST 152	AW	30 days 5 cc	5	3
All-weld metal 52	AW	-	100	3
All-weld metal 52	AW	-	30	2
Aalto NGW 52	AW	-	100	3
Aalto NGW 52	AW	-	30	3
Aalto NGW 52	AW	30 days 30 cc	30	3
Aalto NGW 52	PWHT	-	100	2
Aalto NGW 52	PWHT	-	30	3

4.2 Microscopy

Optical microscopy was applied in order to examine the grain and dendrite structure of the studied materials. Fractographic examinations were performed by using Scanning Electron Microscopy (SEM) in order to get more information on the cracking that occurred during J-R testing. The microscopy results for each material, Alloy 182, 82, 152 and 52 weld metals, are presented, although the main focus of the SEM study was in Alloys 182 and 52 and especially in specimens tested in water with high hydrogen content. The SEM examinations were performed at both Aalto University and at VTT. The microscope used at Aalto University was Zeiss Ultra 55 SEM and at VTT both Zeiss Ultra Plus field emission SEM and Philips XL30 ESEM microscopes were used. In addition, Transmission Electron Microscopy (TEM) was applied in order to study the carbides located at the different boundaries of Alloy 182 and 52 weld metals. The TEM specimens were extracted from the DMW materials of Alloys 182 and 52 and the materials were studied in both as-welded (AW) and post-weld heat treated (PWHT) conditions. TEM examinations were carried out by using VTT's microscope Philips CM200 FEG-STEM. Compositional analyses were carried out utilizing a Noran Voyager energy dispersive X-ray analyser and Gatan System Six software. A liquid nitrogen cold-finger was also employed in order to help reduce hydrocarbon contamination in the microscope.

4.3 Hardness measurements

Vickers hardness was measured for all-weld metal and DMW test blocks by applying a load of 1 kg. The measurements were conducted on polished weld cross-sections, and the presented values are averages from at least five measurements that were located approximately in the middle of the welds, thus being representative to the location of the pre-crack tip of a J-R test specimen.

4.4 TDS measurements

Thermal desorption spectra (TDS) were determined for Alloy 182, 152 and 52 DMW samples. TDS curves were measured for Alloys 182, 52 and 152 for as-welded condition and for Alloys 182 and 52 also in relevant PWHT condition. The effect of pre-exposure at high temperature (300 °C) water was also studied by using hydrogen contents 5 and 30 cm^3 H_2/kg H_2O. The studied coupons were extracted from DMW mock-ups that were also used for the J-R tests. The dimen-

sions of the TDS coupons were about 10 x 4 x 0.9 mm and they were grinded and cleaned before the measurements.

TDS measurements were carried out with a thermal desorption apparatus designed and assembled at Aalto University. It allows to analyse hydrogen desorption in the temperature range of 25 to 1000 °C with background vacuum level better than 10^{-8} mbar. The apparatus consists of main UHV (ultra-high vacuum) chamber equipped with furnace and mass spectrometer and high-vacuum air-lock system for the sample supply into the main chamber. The heating system provides a direct control of the heating rate from 1 to 10 °C/min. Heating rate for most of the measurements in this study was 6 °C/min. Additionally, heating rates of 3 and 9 °C/min were applied for Alloys 182 and 52. Specimens for TDS measurements were cleaned before measurements with acetone in an ultrasonic bath for 1 min and dried in the He-gas flow to remove any water residuals from the specimen surface.

Activation energies were determined for Alloys 182 and 52 (DMW samples) according to the model presented by Lee and Lee (1984) and later applied by e.g. Young et al. (1997) and Ai et al. (2013). Activation energy for hydrogen desorption, E_T, can be calculated for the desorption site observed using ramped TDS data obtained at different heating rates, which produce a different desorption peak temperature, T_c. The T_c increases with the heating rate, φ (= dT/dt), and E_T depends on T_c and φ according to the following equation:

$$\frac{d\ln(\varphi/T_c^2)}{d\,(1/T_c)} = -E_T/R \tag{9}$$

The hydrogen activation energy (E_T) needed to escape from the trap site to the normal lattice site is calculated from the slope of ln (φ/T_c^2) vs ($1/T_c$) plot by measuring the change of peak temperatures with the heating rates.

4.5 Bulk hydrogen measurements

The bulk hydrogen measurements for DMW samples of Alloys 182, 152 and 52 were performed using hydrogen measurement system of Leybold-Heraeus. The samples were grinded and cleaned prior to the measurements. The hydrogen contents were measured from as-welded samples (Alloys 182, 152 and 52) and pre-exposure (30 days at 300 °C PWR water with 30 cm^3 H_2/kg H_2O) samples (Alloys 182 and 152).

5 Results

5.1 J-R test results

J-R test results are presented as average fracture resistance (J_Q) values for each set of parallel specimens. All the J-R curves calculated from the J-R test data as well as J_Q and T values are presented in Annex 1. The curves are presented in Annex 1 for each test environment so that the results obtained for all-weld metal specimens and dissimilar metal weld specimens are divided to separate plots, except for air tests that are all presented in a single plot. In all environment tests there were more than a single specimen of each material tested in each environment and those parallel specimens of a certain material are plotted in the graph using the same colour (blue for Alloy 182, green for Alloy 82, orange for Alloy 152 and red for Alloy 52).

5.1.1 As-welded materials

J-R test results for specimens manufactured from all-weld metal and DMW samples are presented in Figures 26–29. These specimens were tested in as-welded condition. The J-R test results are presented as average values for each test series. Parallel specimens were tested for each material-environment combinations in order to decrease the uncertainty caused by scatter. The average values are calculated from results obtained with two to six parallel specimens per material. The air tests were conducted using all-weld metal specimens and for Alloy 152 also using dissimilar metal weld specimens (KAIST material). The tearing moduli are calculated for the curves that reached crack growth of 0.5 mm.

In air tests, the fracture resistance (J_Q) of Alloy 182 is the lowest of the studied materials. Furthermore, Alloy 182 specimen is the only all-weld metal specimen that shows significant crack growth during J-R testing in ambient air. The GTAW welded materials Alloy 52 and 82 show nothing but blunting during the air test within the 2 mm load-line displacement range that the equipment allows. The results for Alloy 152 DMW and all-weld metal specimens are somewhat scattered since the all-weld metal exhibits higher fracture resistance than the tested DMW specimens.

Figure 26 shows a clear trend between the increasing hydrogen content and decreasing fracture resistance of Alloy 182. The same kind of behaviour can be observed for Alloys 82, 152 and 52 (Figures 27–29, respectively), although decrease in fracture resistance was observed only for some specimens of Alloy 52 in hydrogenated low temperature water. The average fracture toughness results for all the tested materials are lower when tested with hydrogen content 100 cm^3 H_2/kg H_2O than the ones obtained with hydrogen content 30 cm^3 H_2/kg H_2O. Alloy 182 seems to be the most susceptible weld metal to LTCP with hydrogen content 30 cm^3 H_2/kg H_2O. However, at high hydrogen contents (100 cm^3 H_2/kg H_2O) some specimens of Alloy 52 exhibit a large relative decrease of fracture resistance when compared to the results obtained in air, and even the absolute J_Q values are similar to those obtained for Alloy 182.

The J-R test results for Alloys 182 and 152 obtained after pre-exposure in 300 °C water are consistently higher than those obtained in the same test environment without pre-exposure. The effect of pre-exposure is quite clear even after a short (24 h) high temperature exposure with high hydrogen content, although the differences between the results with and without pre-exposure are not dramatic. However, the results for Alloys 82 and 52 are more complicated. Alloy 82 shows slightly higher average results without pre-exposure, although it also exhibits large scatter of the results and quite small amount of data compared to Alloys 182 and 152. It the case of Alloy 52, the pre-exposure seems to increase the average fracture resistance slightly when only all-weld metal specimens are considered, as seen in Figure 30. All of the all-weld metal specimens of Alloy 52 tested with 100 cm^3 H_2/kg H_2O exhibited a significant environmental effect (both with or without pre-exposure), whereas only one of the three DMW Alloy 52 specimens showed a reduction of fracture resistance.

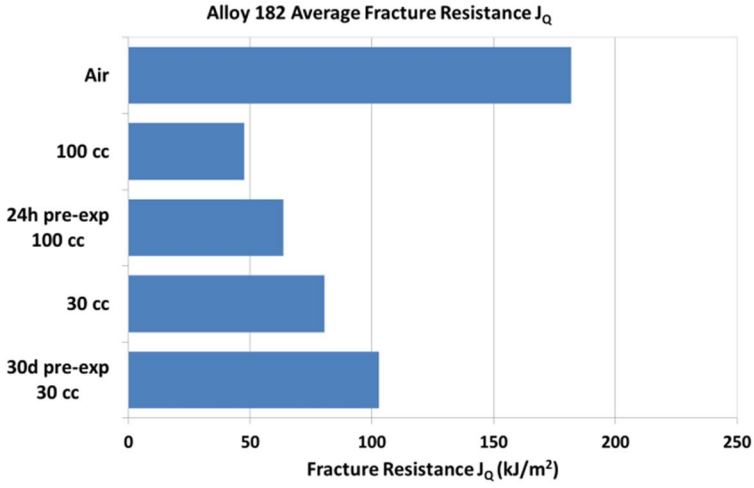

Figure 26. Average fracture resistance (J_Q) values for Alloy 182 tested in air and in 55 ˚C water (200 ppm H_3BO_3 and 2.1 ppm LiOH) with hydrogen contents of 100 and 30 cm^3 H_2/kg H_2O, with and without high temperature (300 ˚C) pre-exposure.

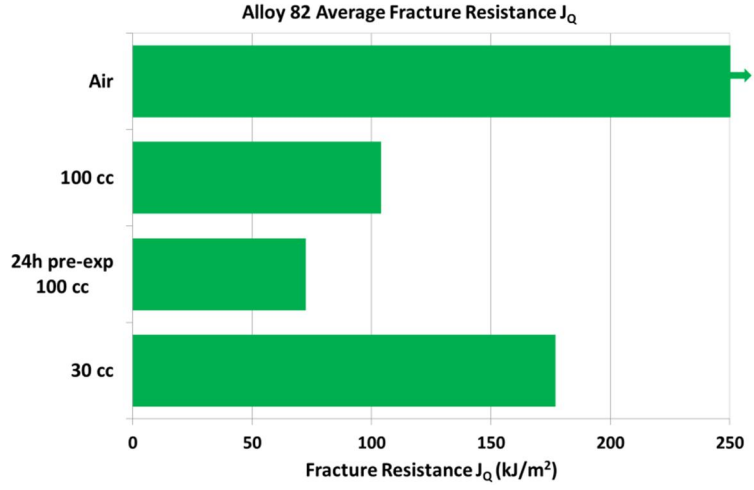

Figure 27. Average fracture resistance (J_Q) values for Alloy 82 tested in air and in 55 ˚C water (200 ppm H_3BO_3 and 2.1 ppm LiOH) with hydrogen contents of 100 and 30 cm^3 H_2/kg H_2O and with high temperature (300 ˚C) pre-exposure. The arrow means that the value is > 250 kJ/m^2.

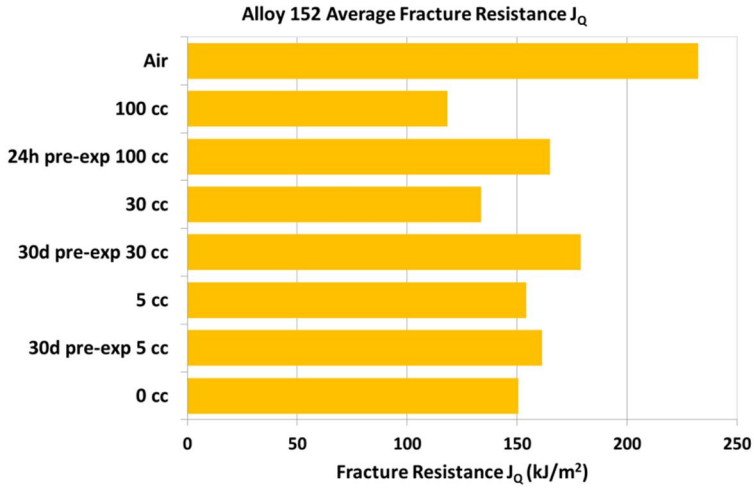

Figure 28. Average fracture resistance (J_Q) values for Alloy 152 tested in air and in 55 ˚C water (200 ppm H_3BO_3 and 2.1 ppm LiOH) with various hydrogen contents and with high temperature (300 ˚C) pre-exposure.

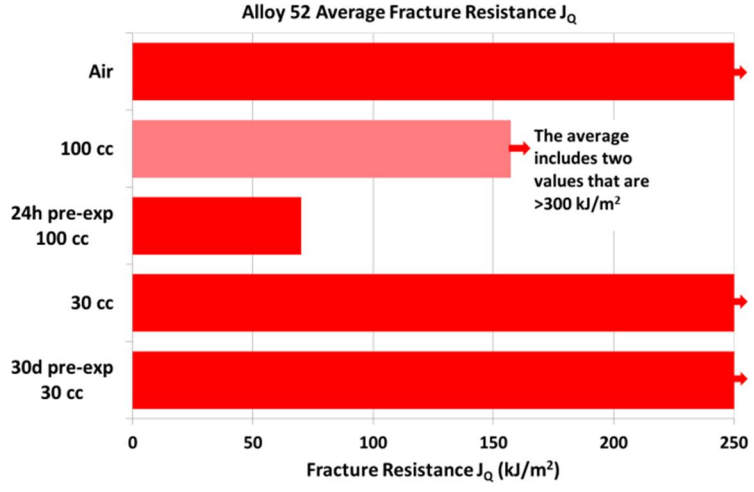

Figure 29. Average fracture resistance (J_Q) values for Alloy 52 tested in air and in 55 ˚C water (200 ppm H_3BO_3 and 2.1 ppm LiOH) with hydrogen contents of 100 and 30 cm^3 H_2/kg H_2O and with high temperature (300 ˚C) pre-exposure. The arrows mean that the average values include values that are >300 kJ/m^2.

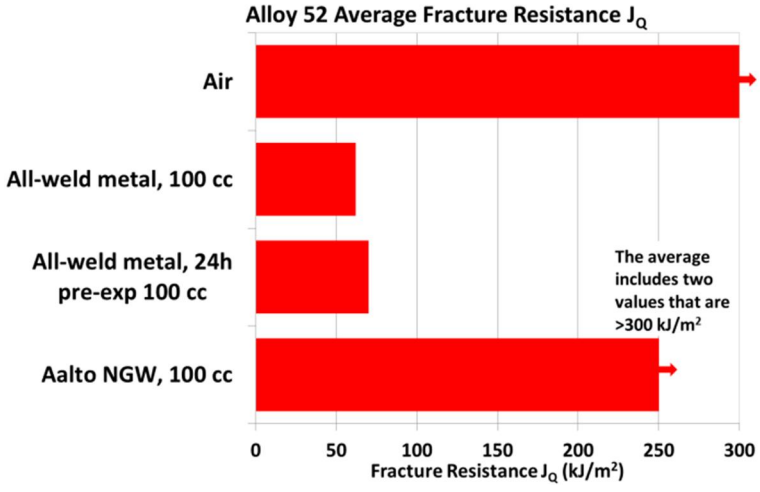

Figure 30. Average fracture resistance (J_Q) values for all-weld metal and DMW specimens of Alloy 52 tested in air and in 55 ˚C water (200 ppm H_3BO_3 and 2.1 ppm LiOH) with hydrogen content of 100 H_2/kg H_2O. All-weld metal specimens were also tested after high temperature (300 ˚C for 24 h) pre-exposure. The average value for the tests conducted for Aalto NGW with 100 cm^3 H_2/kg H_2O (100 cc) includes two values that are >300 kJ/m^2.

5.1.2 Post-weld heat treated materials

Specimens of Alloys 182 and 52 were post-weld heat treated and after that tested in low temperature hydrogenated water. The tested materials were dissimilar metal welds Aalto 182 (Alloy 182) and Aalto NGW (Alloy 52) and the hydrogen contents of the water were 30 and 100 cm^3 H_2/kg H_2O. The average fracture resistance J_Q values are presented in Figure 31 with the air test results of the AW samples as a reference. The calculated J-R curves are presented in Annex 1. The fracture resistance was not significantly affected by the PWHT, although the obtained average J_Q values for PWHT specimens were slightly below the ones obtained for the as-welded DMW specimens. Note that Figure 29 shows the results for all AW Alloy 52 specimens, both all-weld metal and DMW together. However, it must be mentioned that comparing the results for DMW specimens of Alloy 52 is not exact because there were results obtained for both AW and PWHT specimens that can only be determined as >300 kJ/m^2 and the exact value could not be measured. The average J_Q value for PWHT Alloy 182 is about 40 kJ/m^2, which is the lowest average value obtained within this study for any material-environment combination. On the other hand, the tearing resistance was higher in PWHT specimens than in AW specimens of Alloy 182. The average tearing resistance values for AW specimens of Alloy 182 tested with 100 and 30 cm^3 H_2/kg H_2O were 98

and 144, respectively, whereas the corresponding values for PWHT specimens were 185 and 297, respectively. Thus, the tearing resistance of PWHT specimens was about twofold compared to AW specimens with both hydrogen contents of the water.

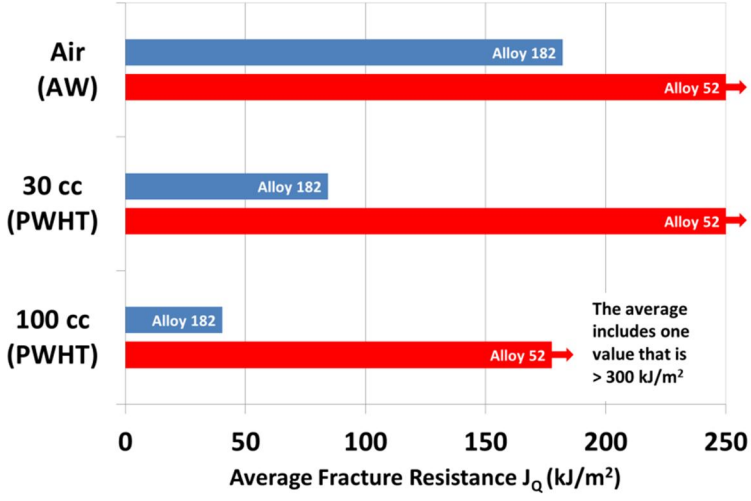

Figure 31. Average fracture resistance values for post-weld heat treated (PWHT) Alloy 182 and 52 DMW specimens tested in hydrogenated low temperature (55°C) water. Air test results for AW specimens are presented for reference.

5.2 Hardness measurements

Vickers hardness results for the weld metal samples are presented in Table 6 as average values from at least five measurements that were located approximately in the middle of the welds. The hardness results for the test materials do not show a large variation. In the case of each weld metal that was studied as both all-weld metal and DMW mock-up the hardness of the DMW mock-up was higher. Aalto Alloy 182 exhibits slightly higher hardness than all-weld metal Alloy 182 and similarly, the hardness of NGW Alloy 52 is slightly higher than that of all-weld metal Alloy 52 in as-welded condition. In the case of Alloy 152 the difference between the all-weld metal (205 HV1) and DMW (253 HV1) materials is the largest. The hardness of NGW Alloy 52 is slightly decreased due to post-weld heat treatment (203 HV1 in AW condition, 191 HV1 in PWHT condition), whereas Aalto Alloy shows the opposite effect of PWHT (208 HV1 in AW condition, 227 HV1 in PWHT condition).

Table 6. Hardness (HV1) measurement results for the nickel-based alloy welds.

Material	Hardness (HV1)
All-weld metal Alloy 182 (AW)	202
Aalto Alloy 182 (AW)	208
Aalto Alloy 182 (PWHT)	227
All-weld metal Alloy 82 (AW)	215
All-weld metal Alloy 152 (AW)	205
KAIST Alloy 152 (AW)	253
All-weld metal Alloy 52 (AW)	200
NGW Alloy 52 (AW)	203
NGW Alloy 52 (PWHT)	191

5.3 TDS and bulk hydrogen content measurements

TDS curves were determined for Alloys 182, 52 and 152 for as-welded condition and for Alloys 182 and 52 also in relevant PWHT condition. The results are presented for Alloys 182, 52 and 152 in Figures 32–34, respectively.

TDS curve maxima for Alloy 182 are located at about same temperature (~ 400 °C) for both as-welded samples and high temperature pre-exposed samples (Figure 32). The curves show that Alloy 182 contains the largest amount of hydrogen when it is in as-welded condition. In addition, it was observed that hydrogen outgassing occurs due to high temperature water pre-exposure. It is also notable that the small peak at about 500 °C in the thermal desorption curve is smaller when measured after pre-exposure to 30 cm^3 H_2/kg H_2O compared to the as-welded condition. The PWHT sample shows a slight shift (about 20 °C) of the maximum peak towards lower temperatures. Furthermore, as a consequence of PWHT, the high temperature peak that was observed to decrease after pre-exposure (30 cm^3 H_2/kg H_2O), does not exist at all in the TDS curve for the post-weld heat treated sample.

TDS peaks for Alloy 52 are somewhat wider in shape in all conditions and have almost a plateau at the maximum (Figure 33). This shape indicates that the peak is a sum of at least two peaks. In as-welded condition, Alloy 52 exhibits a low thermal desorption peak. Pre-exposure in high temperature water with 30 cm^3 H_2/kg H_2O increases the hydrogen content of the material so that the TDS peak maximum is at about the same level as that in the respective curve for Alloy 182. Assuming that there are at least two peaks included in the desorption curve, the higher temperature peak at about 500 °C occurs also in the case of Alloy 52. Pre-exposure with 5 cm^3 H_2/kg H_2O does not affect the hydrogen desorption behaviour of Alloy 52 significantly when compared to the result obtained for as-welded condition.

Of the studied materials Alloy 152 (Figure 34) manifests the highest TDS peak in as-welded condition, which is in accordance with the bulk hydrogen content

measurements presented in Table 7. The TDS peak maxima are significantly lower after pre-exposure to high temperature water. The TDS curve obtained for the 5 cm^3 H_2/kg H_2O pre-exposed sample has a complex shape with multiple peaks, whereas the shape of the curve for 30 cm^3 H_2/kg H_2O pre-exposed sample is smoother.

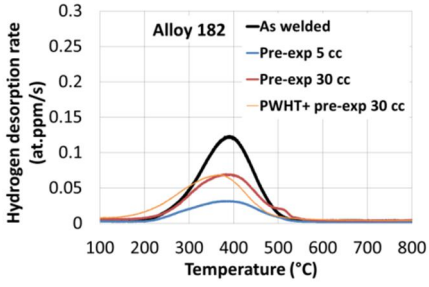

Figure 32. Thermal desorption spectra for Alloy 182 DMW samples in as-welded condition, after high temperature water (300 °C) exposure ("pre-exp", 5 and 30 cm^3 H_2/kg H_2O) and after PWHT and high temperature (300 °C) water exposure (30 cm^3 H_2/kg H_2O). The heating rate in the measurements was 6 K/min.

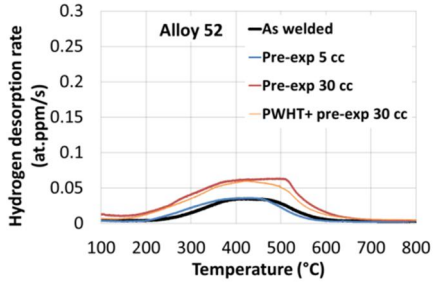

Figure 33. Thermal desorption spectra for Alloy 52 DMW samples in as-welded condition, after high temperature water (300 °C) exposure ("pre-exp", 5 and 30 cm^3 H_2/kg H_2O) and after PWHT and high temperature water (300 °C) exposure (30 cm^3 H_2/kg H_2O). The heating rate in the measurements was 6 K/min.

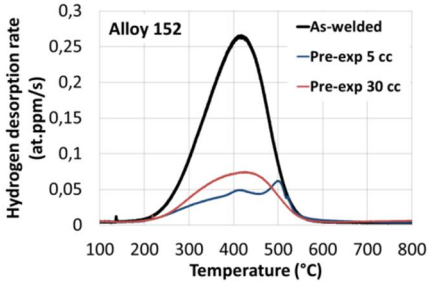

Figure 34. Thermal desorption spectra for Alloy 152 DMW samples in as-welded condition and after high temperature water (300 °C) exposure ("pre-exp", 5 and 30 cm^3 H_2/kg H_2O). The heating rate in the measurements was 6 K/min.

Table 7. Hydrogen content measurements for Alloys 182, 152 and 52. 30 days high temperature water (300 °C) exposure (pre-exp) was performed in hydrogenated PWR water (30 cm^3 H_2/kg H_2O).

Sample	Hydrogen content (wt ppm)
Alloy 182 (As-welded)	2.2
Alloy 152 (As-welded)	5.3
Alloy 52 (As-welded)	1.3
Alloy 182 (Pre-exp 30 cc)	1.5
Alloy 152 (Pre-exp 30 cc)	1.6

As-welded Alloy 182 was further studied in order to determine the activation energy for hydrogen desorption. Heating rates (φ) of 2, 4, 6, 8 and 10 K/min were chosen. It was assumed based on the literature (e.g., Ai et al., 2013) that the higher the heating rate is the higher is the desorption peak, but that was not the case in all the conducted measurements in this study, as can be seen in Figure 35, where the TDS spectra for different heating rates are presented. However, the results show consistently that higher heating rates result in higher temperatures of the TDS peak maxima. Thus, activation energy was successfully determined and the result is presented in Figure 36 for as-welded Alloy 182. According to the calculations that were based on TDS measurements the hydrogen activation energy (E_T) needed to escape from the trap site to the normal lattice site is 40.0 ± 3.7 kJ/mol.

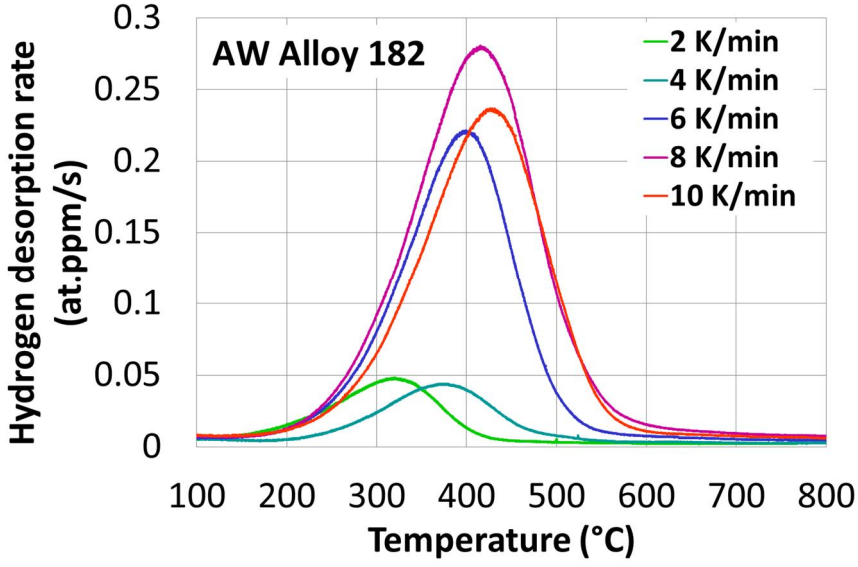

Figure 35. Thermal desorption spectra for DMW Alloy 182 samples in as-welded condition measured with heating rates of 2, 4, 6, 8 and 10 K /min.

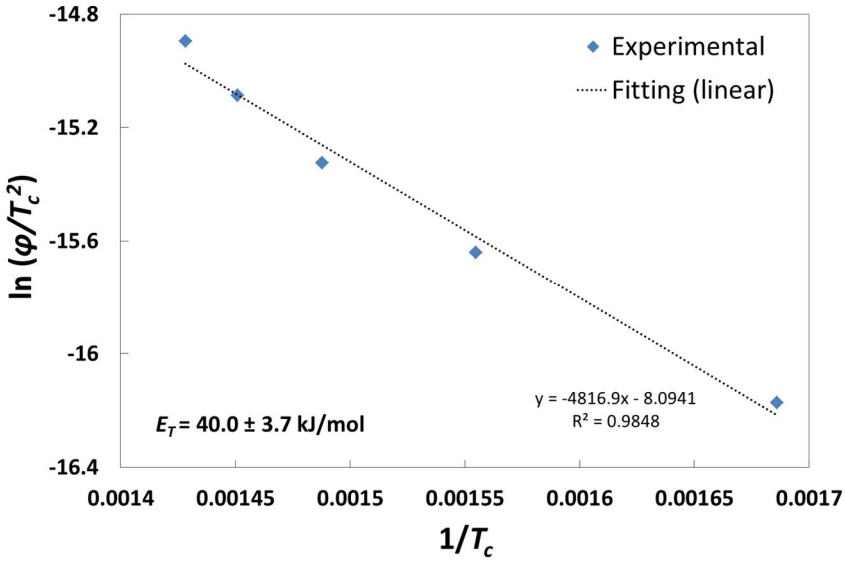

Figure 36. Determination of the activation energy and its 95% confidence interval according to method by Lee & Lee (1984) for hydrogen desorption from the ramped TDS results for Alloy 182 DMW.

The heating rates of 3, 6 and 9 K/min were used for specimens of Alloy 52 DMW that were post-weld heat treated and exposed to high temperature hydrogenated water (30 cm^3 H_2/kg H_2O) for 30 days prior to the TDS measurements. It seems that the curve for each measurement is possibly sum of more than just one peak (Figure 37). In the TDS curve tested with 9 K/min at least two separate peaks are clearly distinguished.

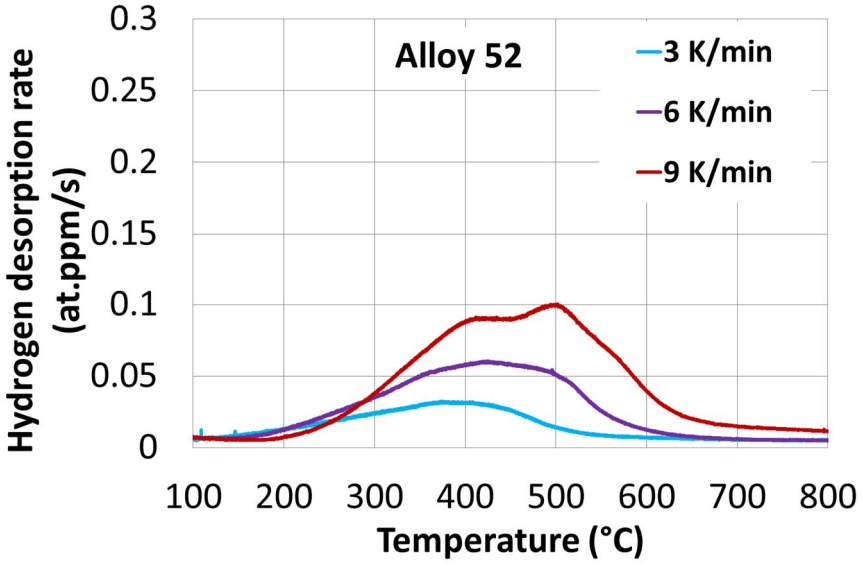

Figure 37. Thermal desorption spectra for Alloy 52 DMW samples (Aalto NGW mock-up) after PWHT and 30 days pre-exposure at 300 °C water measured with three different heating rates: 3, 6 and 9 K/min.

The peaks were further studied by calculating a mathematical curve fitting for each result (3, 6 and 9 K/min) and determining Gaussian curves representing the different parts of the fitting curve. The results for curve fittings are presented in Figure 38, a), b) and c). The temperatures of the Gaussian curve peaks are then used according to Lee & Lee (1984) in order to calculate the activation energies for the peaks representing different trapping sites. The results for the determination of activation energies for hydrogen desorption are presented in Figure 39. The activation energies representing the two traps in Alloy 52 DMW were calculated to be 26.7 ± 2.8 kJ/mol for the higher temperature peaks (right peaks) and 18.4 ± 2.7 kJ/mol for the lower temperature peaks (left peaks).

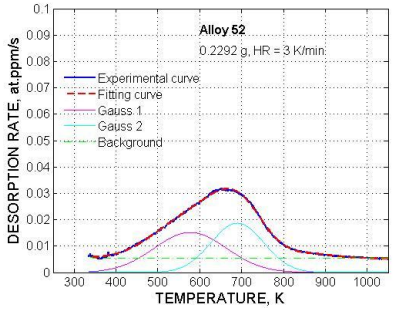

a)

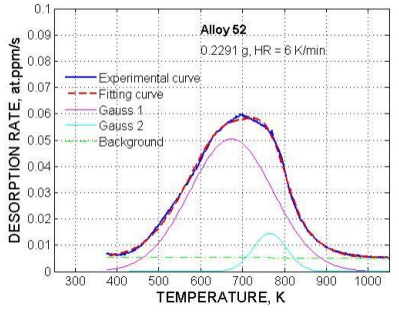

b)

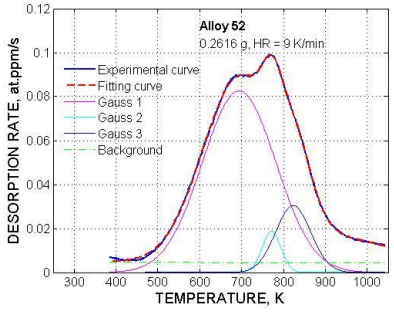

c)

Figure 38. Gaussian curve fittings for Alloy 52 DMW TDS measurements conducted with heating rates 3 (a), 6 (b) and 9 K/min (c).

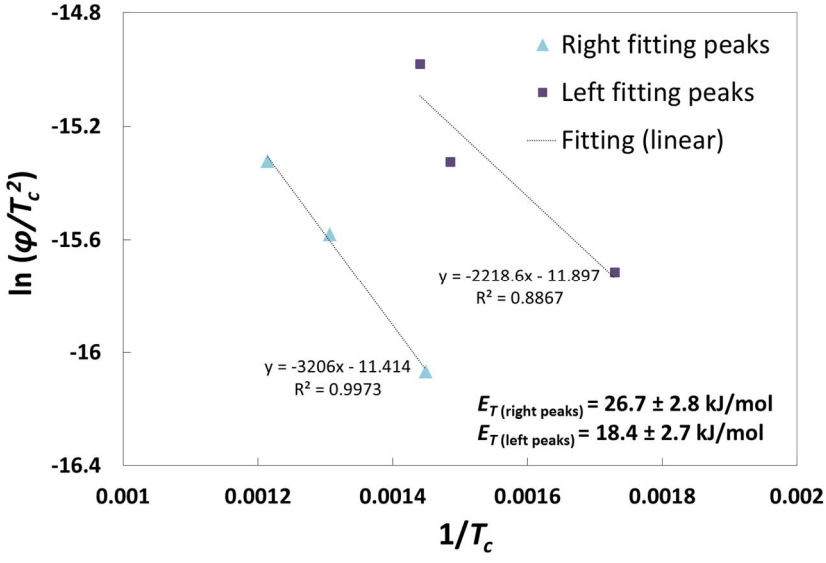

Figure 39. Determination of the activation energies and their 95% confidence intervals according to method by Lee & Lee (1984) for hydrogen desorption from the ramped TDS results for PWHT + 30 cm^3 H_2/kg H_2O pre-exposed Alloy 52 DMW.

5.4 Optical microscopy

The cross-sections of the studied weld metals showed complex appearance with varying grain size in optical microscopy. The optical microscope images for all-weld metal Alloys 182, 82, 152 and 52 are presented in Figures 40–43, respectively. Grain boundaries were clearly visible after etching in Alloy 52 but less observable in the other studied alloys. However, it was observed that the dendrite orientations usually exhibit considerable changes from grain to grain.

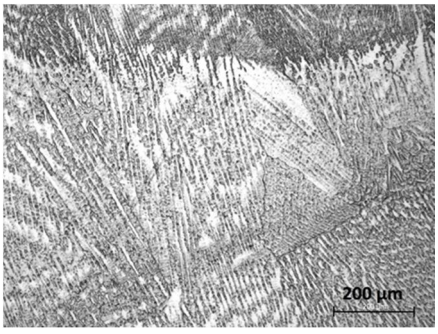

Figure 40. Optical microscope image of the all-weld metal test block Alloy 182 cross-section.

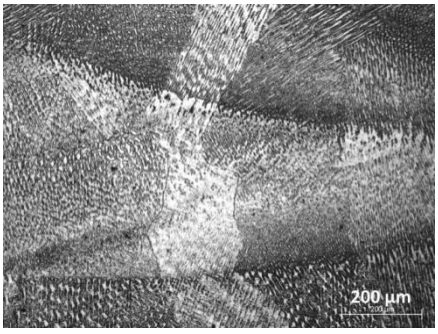

Figure 41. Optical microscope image of the all-weld metal test block Alloy 82 cross-section.

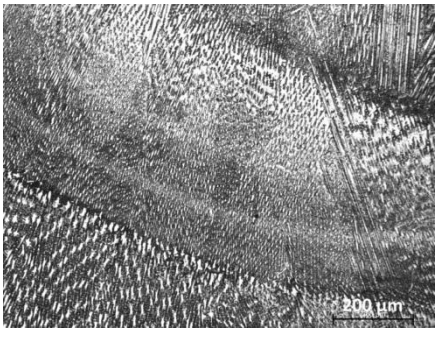

Figure 42. Optical microscope image of the all-weld metal test block Alloy 152 cross-section.

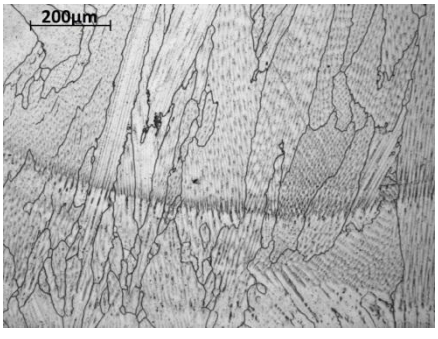

Figure 43. Optical microscope image of the all-weld metal test block Alloy 52 cross-section.

5.5 EDS line scans

The dilution of the dissimilar metal weld test blocks was studied by performing EDS line scans over the weld cross-sections. The results of EDS analyses are presented for dissimilar metal weld materials Alloy 182 (Aalto 182 mock-up) in Figure 44, Alloy 152 (KAIST mock-up) in Figure 45 and Alloy 52 (Aalto NGW mock-up) in Figure 46. The chemical composition of the test block is relatively close to the nominal composition in case of Aalto 182 and KAIST mock-up when measured a few millimetres away from the fusion line towards the weld. However, in Aalto NGW mock-up (Alloy 52) dilution of nickel is significant in the weld (~10% lower than nominal) and respectively the iron content of the weld is significantly larger than the nominal iron content in Alloy 52.

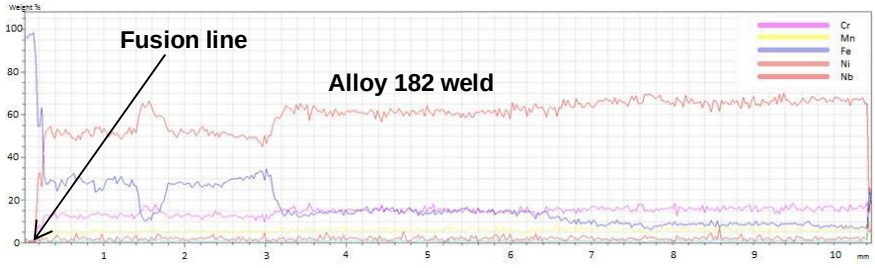

Figure 44. EDS analysis of the chemical composition profile of the DMW Alloy 182 (Aalto Alloy 182 mock-up). The nominal contents of Ni, Cr and Fe in Alloy 182 are 68 %, 15.7 % and 6.7 %, respectively.

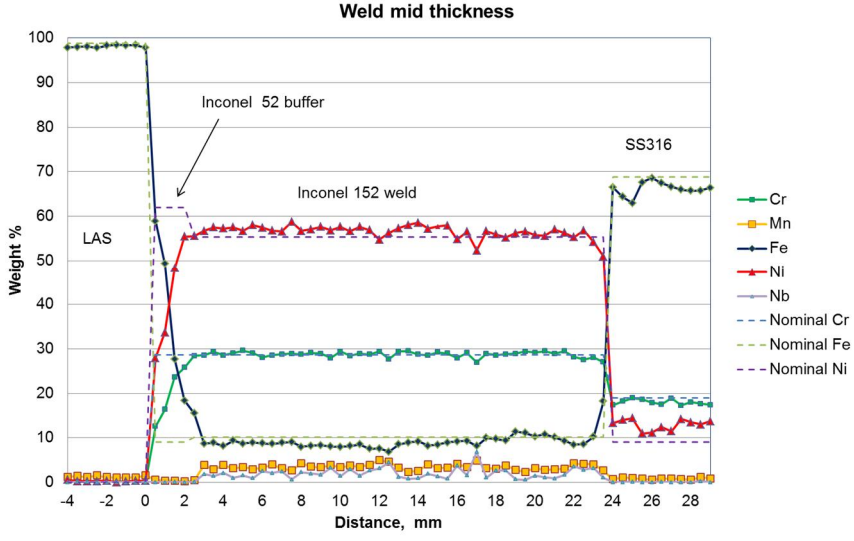

Figure 45. EDS analysis of the chemical composition profile of the DMW Alloy 152 (KAIST mock-up).

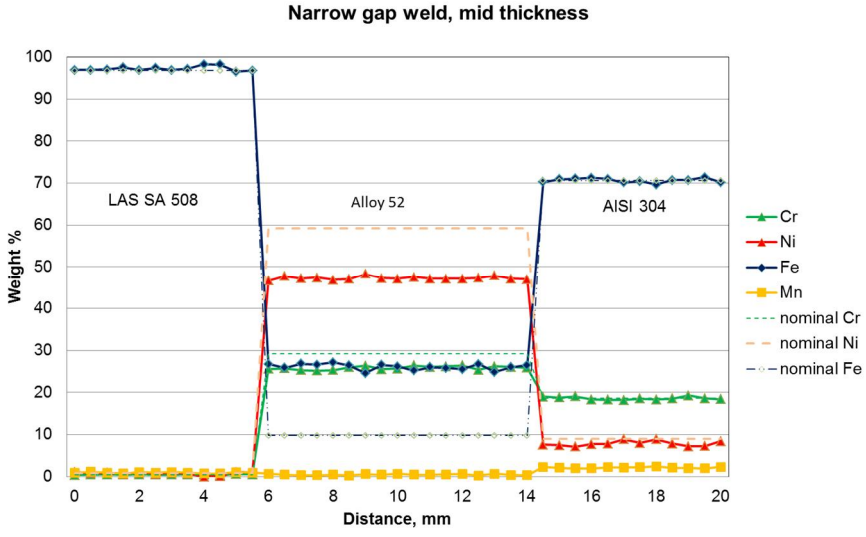

Figure 46. EDS analysis of the chemical composition profile of the DMW Alloy 52 (Aalto NGW mock-up). The EDS analysed sample was in post-weld heat treated (PWHT) condition.

5.6 Fractography

The SEM images presented in this chapter have been taken of fracture surfaces of specimens tested with high hydrogen content in the water, 100 cm^3 H_2/kg H_2O. These specimens were chosen for the study because they exhibit more features of hydrogen-related fracture than the specimens tested with lower hydrogen contents in the water. Alloys 182 and 52 were J-R tested at both AW and PWHT conditions and thus both conditions are also represented in this chapter. In addition, both all-weld metal and DMW specimens of Alloys 182 and 52 were studied. The presented images of Alloy 82 are from all-weld metal specimens and the images of Alloy 152 are from KAIST mock-up.

Intergranular or interdendritic fracture surfaces of the studied samples of Alloys 182 and 82 show a tortuous appearance. Also the intergranular fracture surfaces of Alloy 52 are macroscopically uneven but locally smoother than those of Alloy 182 when observed in a higher magnification.

It was observed that most of the interdendritic fracture surfaces of both Alloys 182 and 52 exhibited a fine structure containing small Cr carbides, although the features found on Alloys 182 and 52 were not exactly similar with each other. These kinds of structures were found on all of the studied fracture surfaces on ID fracture areas, although it was not clearly observable in locations where the topography of the surface was rough or tilted from the viewing angle. EDS (Energy-Dispersive X-ray Spectroscopy) analyses were performed in various locations of an Alloy 52 sample fracture surface in order to investigate the possibility that the structure would merely be an oxide formed on the fracture surface after the actual J-R –test. However, the analyses from ID areas having the studied structure did not show higher oxygen contents than the analyses from the other areas.

Secondary cracking occurred at various locations of the fracture surface of majority of the specimens. Secondary cracks were more common in the part of the fracture surface where an angle between the orientation of dendrites and the maximum principal stress was present.

A general observation in the SEM study was that the fracture morphology and J-R test results were found to correlate with each other. In specimens where the fracture resistance values were in the lower end of the range of the results the dominant fracture type was intergranular or interdendritic (IG/ID). On the other hand, the higher fracture resistance values were detected to correspond to fracture surface features typical of ductile fracture, such as dimples and shear failure. Examinations in microscopic scale, by using large magnifications, provide information on the possible hydrogen trapping sites of the material. The studied features of the inclusions and precipitates included e.g. morphology, density and distribution. When this morphological information obtained using SEM and TEM is supplemented with chemical analyses by applying EDS, the different inclusions and precipitates can be identified based on literature.

5.6.1 Alloy 182 fractography

Fracture surfaces of as-welded and post-weld heat treated specimens were examined by using SEM. In addition, the two different Alloy 182 materials that were J-R tested, i.e. DMW and all-weld metal, were also examined in order to study the possible microstructural differences of these materials. The J-R test behaviour of the two Alloy 182 materials was found to be similar when tested in AW condition in hydrogenated low temperature water, but yet they were found to exhibit some different features on the fracture surfaces.

5.6.1.1 As-welded (AW) Alloy 182 specimens

The fracture surfaces presented here are from the specimens tested with hydrogen content 100 cm^3 H_2/kg H_2O. The fracture surfaces of the investigated AW all-weld metal Alloy 182 specimens are dominated by interdendritic or intergranular fracture with some ligaments consisting of dimples, as shown in Figure 47, a) and b). The crack has grown mainly along dendrite or grain boundaries. The dendrite orientation changes along the fracture surface.

More detailed observation of the fracture surface shows that there are different types of precipitates on the interdendritic surface. The larger precipitates, appearing light in the SEM, were found to contain Nb (Figure 47 c)). Different types of smaller precipitates containing Cr or Ti were also observed, as mixed oxides containing Al and Si. Signs of plastic deformation were observed in various locations on the interdendritic fracture surfaces. Figure 47 d) illustrates slip bands on the fracture surface. The extension of slip bands is hindered by precipitates, such as the carbide seen in the middle of the figure. Small globular carbides (~30–200 nm in diameter) were observed as well as small pits that seem to fit to the size of the carbides (Figure 47 d)). EDS map analysis of an IG/ID fracture surface area of all-weld metal Alloy 182 is presented in Figure 48. The EDS analysis indicates that there is a large amount of small Cr-rich carbides on the fracture surface and thus the small carbides observed in Figure 47 d) are probably mostly Cr-rich. However, another EDS analysis, presented in Figure 49, indicates that there are also some small Nb-rich carbides that are in the same size scale with the Cr-rich carbides.

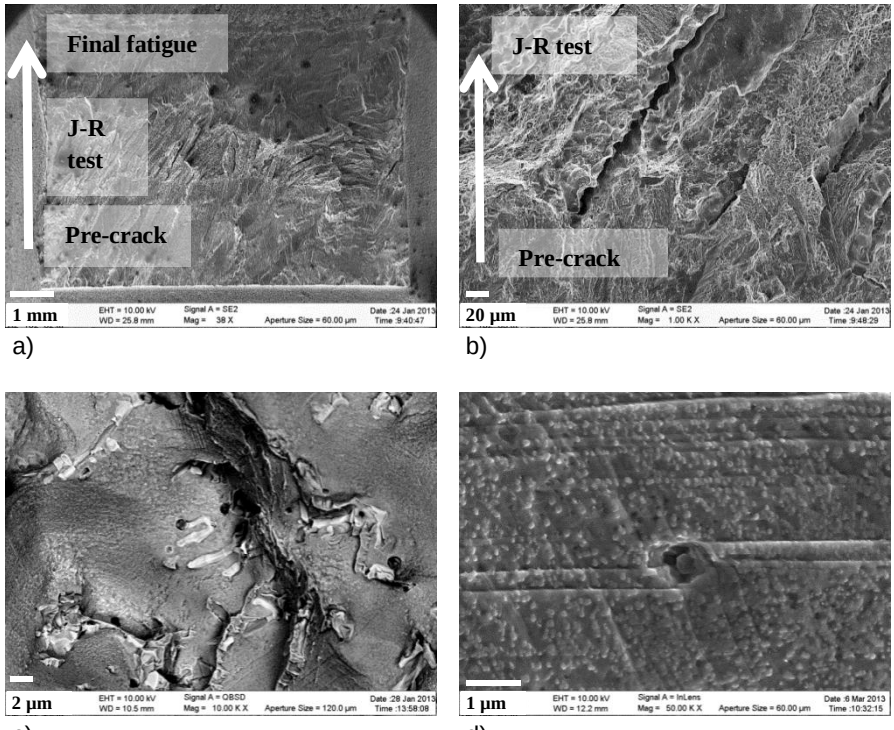

Figure 47. The fracture surface of as-welded all-weld metal Alloy 182 specimen tested in hydrogenated (100 cm^3 H_2/kg H_2O) low temperature water. Crack growth direction is upwards in the images. A general view of the fracture surface is presented in a), a secondary electron image (SE). A secondary electron (SE) image b) illustrates the transition from the fatigue pre-crack (transgranular) to IG/ID cracking. Areas of pre-crack blunting and areas of transition from pre-crack to IG/ID cracking without blunting alternate. Detailed views of the IG/ID fracture surface are presented in c), an electron back-scatter (BSE) image, and d), a high magnification secondary electron (SE) image. The IG/ID fracture surface is decorated by very small carbides, shown in d).

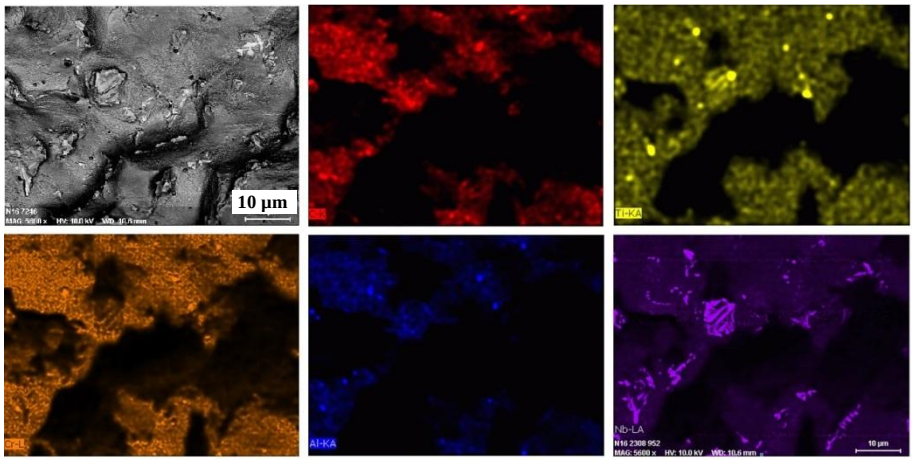

Figure 48. The results of an EDS analysis performed for IG/ID fracture surface area of Alloy 182 presented in the upper left image. The red image represents C, yellow represents Ti, orange represents Cr, blue represents Al and purple represents Nb.

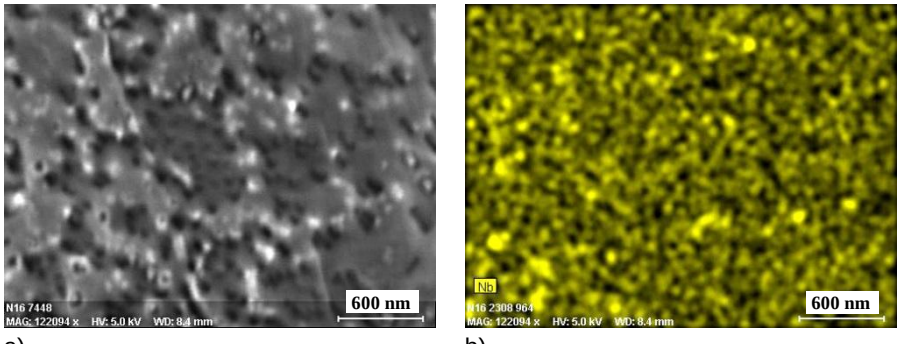

a) b)

Figure 49. An EDS map analysis performed for an area a) of the fracture surface of all-weld metal Alloy 182. The distribution of Nb is shown in b) in yellow. Some of the small carbides appear to be Nb-rich.

The fractographs of DMW Alloy 182 (Aalto 182) specimens are presented in Figure 50. The appearance of the fracture surface is diverse with alternating areas of IG/ID fracture, transgranular fracture (TG) through the dendrites and some areas of dimples, as shown in a) and b). A more detailed view of the TG fracture is presented in Figure 50 c) and a detail of that with larger magnitude from the middle of the TG area in Figure 50 d). These images show that the transgranular crack growth has a very orientated appearance, from the middle of the feature towards the edges. The local crack growth is oriented in 45 degrees angle related to the general crack growth direction. Slip lines are also clearly visible in d). The grain or dendrite boundary carbides observed on the fracture surfaces of the DMW specimens were similar to those observed in the all-weld metal specimens (Figure 47, c) and d)) with the exception of some larger tetrahedron-shaped carbides that were observed at a few locations. The size of these tetrahedron-shaped carbides was up to almost 1 µm. An area containing such carbides is presented in Figure 50, e) and f) that show an area on the both sides of the mating specimen halves.

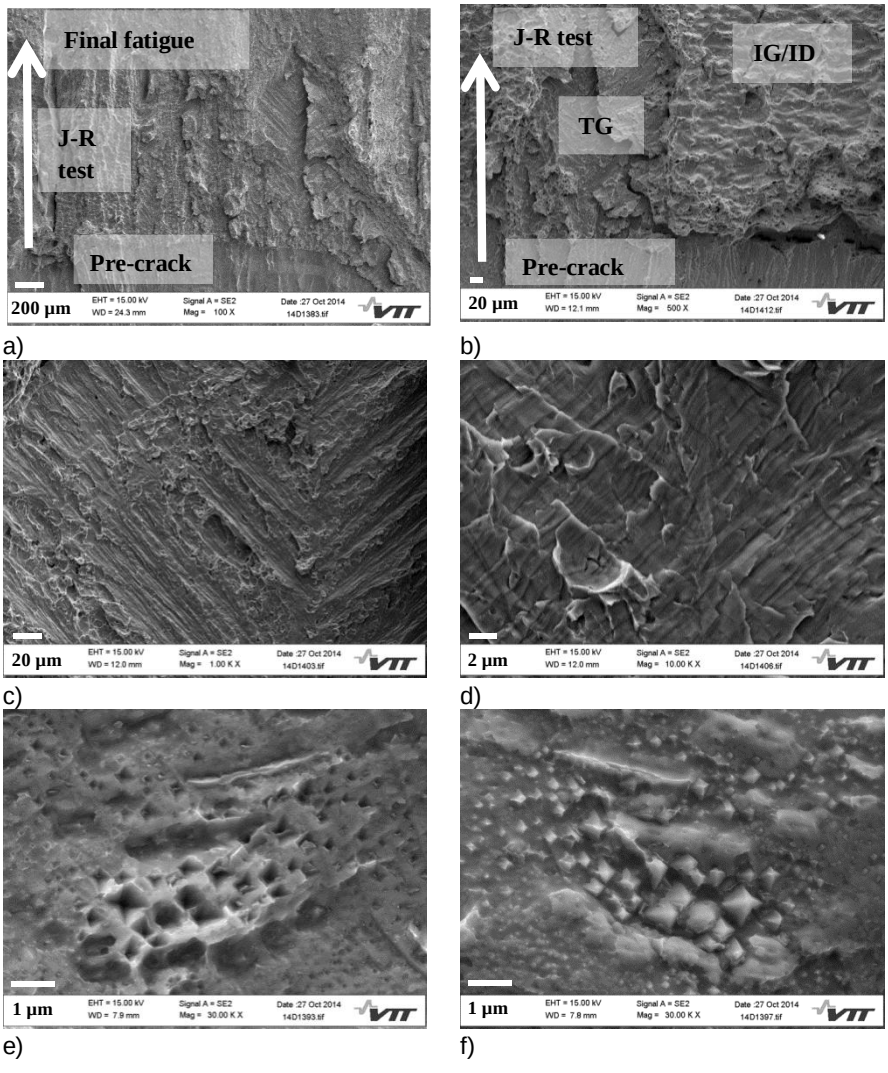

Figure 50. The fracture surface of as-welded DMW Alloy 182 specimen tested in hydrogenated (30 cm^3 H_2/kg H_2O) low temperature water. Crack growth direction is upwards in the images. A general view of the fracture surface is presented in a), a secondary electron image (SE). A secondary electron (SE) image b) illustrates the transition from the fatigue pre-crack (transgranular) to IG/ID cracking and shows areas of TG, IG/ID and dimple fracture. TG area is presented in c) and a detailed view of the area in d). Both sides of the mating halves of a specimen showing an area of larger (up to 1 µm) tetrahedron-shaped carbides is presented in e) and f). The larger carbides have remained in the specimen half presented in f). The area is surrounded by smaller carbides that exhibit a globular or a tetrahedron shape.

5.6.1.2 Post-weld heat treated Alloy 182 specimens

The fracture surfaces of the studied specimens of post-weld heat treated DMW Alloy 182 show a mixed appearance with IG/ID areas, ductile dimple areas and transgranular fracture surface areas that have an appearance that resembles chevron marks (Figure 51, a) and b)). Those areas are rather planar and feather-shaped (Figure 51 c)). The TG fracture appears to grow in 45 degree angle to the overall cracking direction. The fraction of transgranular fracture changed from specimen to specimen but some of that type of fracture was observed on each PWHT Alloy 182 fracture surface. As can be seen in Figure 51 b), that shows the fracture surface of an Alloy 182 DMW specimen, the fracture surface appearance is mixed. Both IG/ID areas, transgranular areas and ductile dimple areas are observed. The transgranular areas resemble the shape of the dendrites and the fracture surface is macroscopically quite flat within a grain.

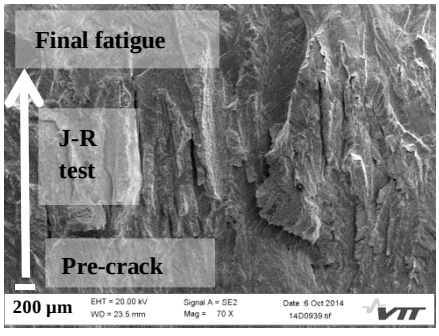

a)

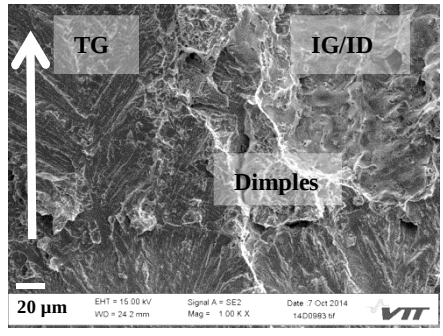

b)

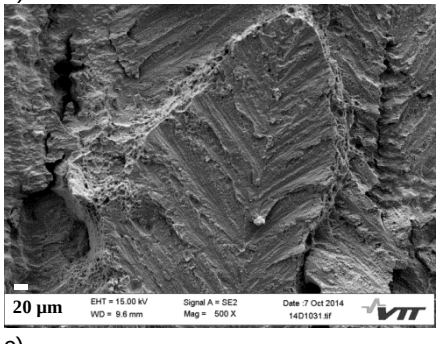

c)

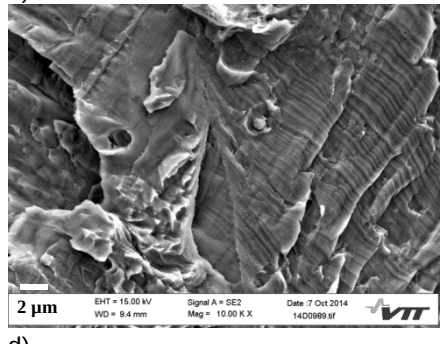

d)

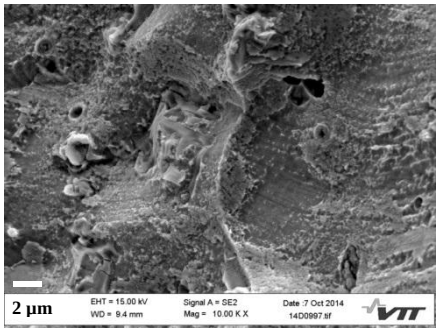

e)

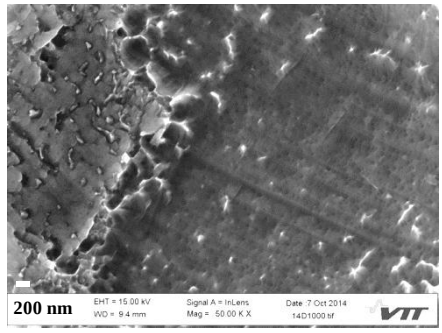

f)

Figure 51. The fracture surface of post-weld heat treated DMW Alloy 182 specimen tested in hydrogenated (100 cm^3 H_2/kg H_2O) low temperature water. Crack growth direction is upwards in the images. A general view of the fracture surface is presented in a), a secondary electron image (SE). Image b) illustrates an area at the transition from pre-crack to J-R test crack. The cracking type is intergranular or transgranular depending on the pre-crack tip location in the microstructure, and ductile ligaments have remained between those areas. The feather-like appearance of transgranular cracking is shown in c). A detailed view from the transgranular fracture surface is shown in d). Slip lines are clearly visible on the TG fracture surface. IG/ID fracture surface area is presented in e) and f). Alternating areas of carbide-rich areas and areas with small tetrahedron-shaped pits were observed. The size of the small pits and the carbides was about 50–100 nm. Some more irregular-shaped larger precipitates are also visible on the IG/ID fracture surfaces.

5.6.2 Alloy 82 fractography

The fracture surface morphology of Alloy 82 specimens tested with high hydrogen content is mostly transgranular with some intergranular or interdendritic regions. The crack growth of the Alloy 82 specimens was smaller than in the case of Alloy 182, although some relatively low J_Q values were measured also for Alloy 82. A general view in Figure 52 a) shows an uneven appearance of the fracture surface and also reveals some shapes of dendrites similar to that what was observed in DMW Alloy 182. The crack during the J-R test grows through different planes of dendrites as illustrated in Figure 52 b). The IG/ID areas were few in Alloy 82 fracture surfaces and usually they were not oriented exactly towards the crack growth direction, as in the case of Figure 52 c). Small (~100 nm) globular precipitates were observed at the IG/ID fracture surfaces as presented in Figure 52 d).

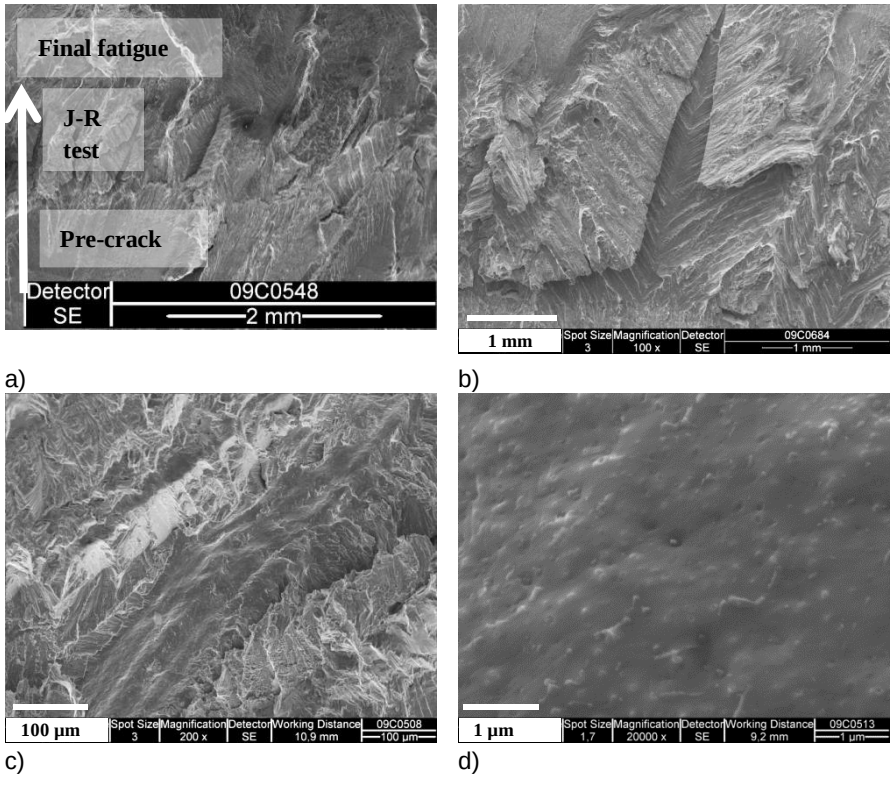

Figure 52. The fracture surface features of as-welded Alloy 82 all-weld metal specimens tested in hydrogenated (100 cm^3 H_2/kg H_2O) low temperature water. A general view of the fracture surface is presented in a), a secondary electron image (SE). A secondary electron (SE) image b) illustrates the transition from the fatigue pre-crack (transgranular) to J-R test cracking. The J-R test cracking is mostly transgranular with some areas of IG/ID cracking. An area of IG/ID fracture surface is presented in c). A higher magnification secondary electron (SE) image of the IG/ID area is presented in d). The IG/ID fracture surface is decorated by very small globular carbides, as shown in d). Crack growth direction is upwards in the images.

5.6.3 Alloy 152 fractography

The studied DMW Alloy 152 specimen fracture surface has mostly ductile appearance with a few IG/ID areas (Figure 53 a)). Typically, IG/ID cracking occurred when the pre-crack tip was at the grain/dendrite boundary when the J-R test was started (Figure 53 b)), although transition from dimple fracture to IG/ID fracture also occurred locally during the J-R test. The fracture surface consists of local areas with and without carbide-rich layer, as illustrated in Figure 52 c). The IG/ID fracture surface layer consists mostly of small tetrahedron-shaped carbides and

the areas without layer exhibit small tetrahedron-shaped pits, that are visible in Figure 53 d) and f). In addition, larger MC-type Nb carbides, such as the larger one in Figure 52 e), Ti carbides and Al oxides were also observed on the fracture surface. Slip lines were observed on the IG/ID fracture surface areas.

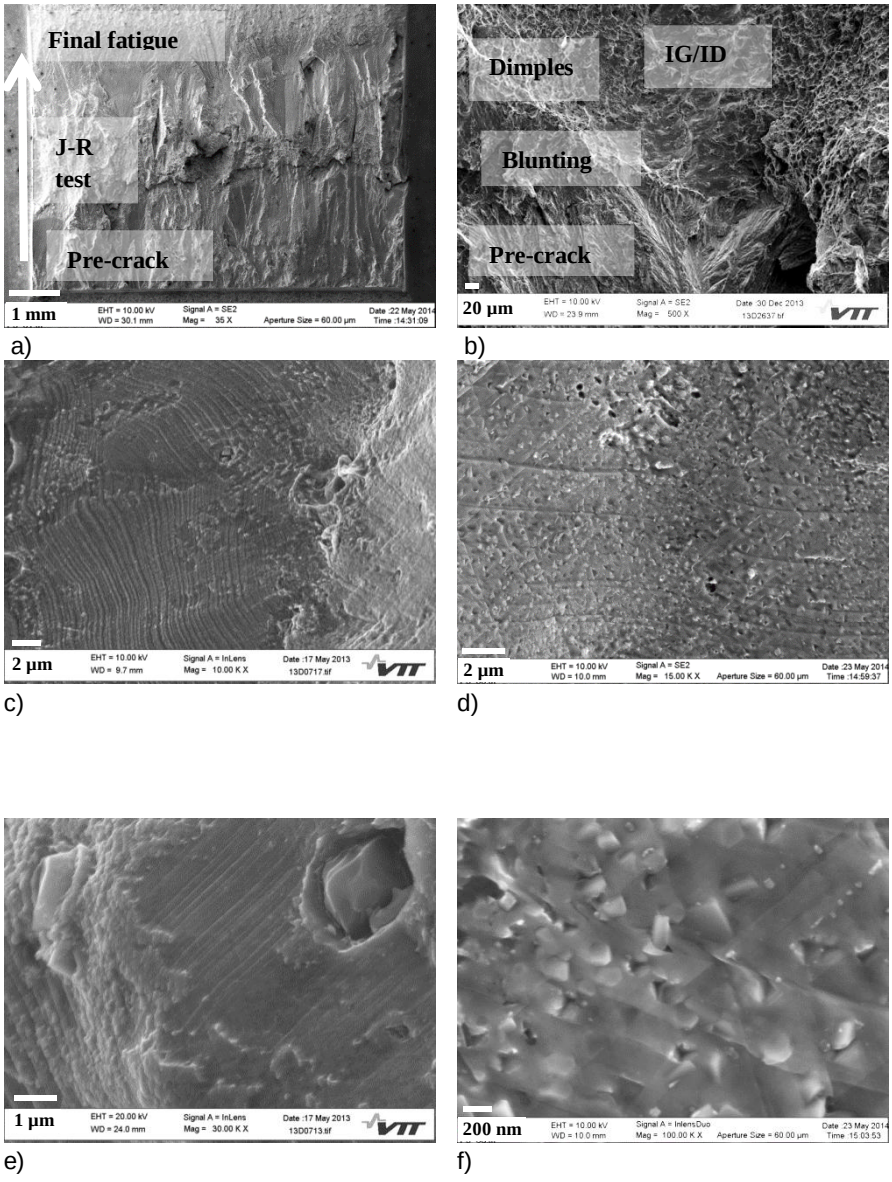

Figure 53. In a) a general view of the fracture surface of an Alloy 152 DMW spec-

imen tested in hydrogenated (100 cm^3 H_2/kg H_2O) low temperature water, secondary electron (SE) SEM image. Cracking during the test is mostly ductile dimple fracture with few areas of IG/ID fracture, and the transition from fatigue pre-crack to the different types of fracture is illustrated in b). IG/ID fracture occurs without significant blunting when the pre-crack tip location is favourable regarding the grain/dendrite boundary, as shown in b). Secondary electron (SE) SEM images c), d), e) and f) show the fine microstructure with a large amount of carbides observed on the IG/ID fracture surface. Fine tetrahedron-shaped carbides as well as small tetrahedron-shaped pits were observed on the IG/ID fracture surface. Image f) presents the $M_{23}C_6$ carbides on the IG/ID fracture surface of DMW Alloy 152.

5.6.4 Alloy 52 fractography

All-weld metal Alloy 52 samples exhibited large areas of IG/ID fracture with very few areas of ductile appearance (Figure 54 a)). Figure 54 a) shows also that the local dendrite growth direction is not parallel to the nominal global crack growth direction. This is consistent with the microstructure presented in optical microscope image Figure 43 that shows varying grain size and orientations. Details of the fracture surface showing the transition from the transgranular pre-crack to IG/ID cracking are presented in Figure 54 b).

The IG/ID fracture surfaces of Alloy 52 exhibited large amounts of small tetrahedron-shaped $M_{23}C_6$-type Cr carbides (Figure 54 c)). The interdendritic fracture surface consists of alternating areas of carbide-rich structure and areas where the carbides have been detached and left on the opposing side of the mating fracture surface (Figure 54 d)). It appears that the crack may advance either through, below or over the tetrahedron-shaped carbides.

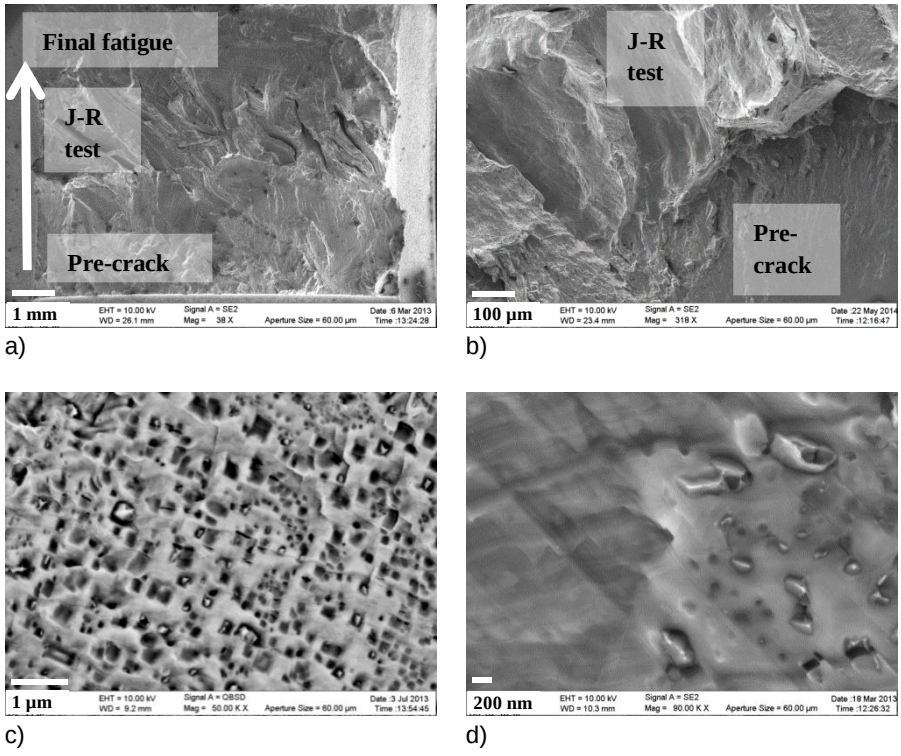

Figure 54. In a) and b) general view of the fracture surface of an Alloy 52 all-weld metal specimen tested in hydrogenated (100 cm^3 H_2/kg H_2O) low temperature water, secondary electron (SE) SEM images. Crack growth direction is upwards in the images. Secondary cracking occurs along the dendrite boundaries. Electron backscatter (BSE) c) and secondary electron (SE) d) SEM images showing the $M_{23}C_6$ carbide structure on the fracture surface of Alloy 52 all-weld metal. Image c) presents variation of the carbide size and details of the carbides. Largest of them show cracking of the carbide. Image d) illustrates the fine fracture surface structure consisting of alternating areas of carbide-rich structure and areas where the carbides have been detached and left on the opposing side of the mating fracture surface.

The SEM examined Alloy 52 DMW sample tested with 100 cm^3 H_2/kg H_2O (J_Q 150 kJ/m^2) exhibited only some areas of IG/ID fracture and large areas with ductile appearance (Figure 54 a)). The transition from the transgranular pre-crack to ductile dimple fracture or IG/ID cracking is illustrated in Figure 54 b). Transition from pre-crack to IG/ID cracking occurs typically when there is a similar orientation between the fatigue pre-crack and the grain/dendrite boundary. Such an area of similar orientation is presented in Figure 56 c). There is a large amount of carbides present also in the IG/ID fracture surface of the Alloy 52 DMW specimen. The size of carbides, that most probably are $M_{23}C_6$, ranges between about 50 to 200 nm.

Both halves of an Alloy 52 specimen tested in 55°C hydrogenated water (100 cm^3 H_2/ kg H_2O) were carefully examined in order to study if the structure of the fracture surface was matching on the opposing sides of the fractured specimen. Figure 55 illustrates both sides of the fracture surface of a sample at the same location. The specimen halves appear to match almost exactly with each other except for some differences that are caused by plastic deformation. Figure 55 shows that there is a very thin layer-like structure containing sharp tetrahedron-shaped carbides on the IG/ID surface and the structure sporadically changes from dendrite to dendrite. Furthermore, the tetrahedron-shaped carbides observed on the fracture surface leave a mark of plastic deformation to the fracture surface of the mating specimen half, when they are detached from the IG/ID surface.

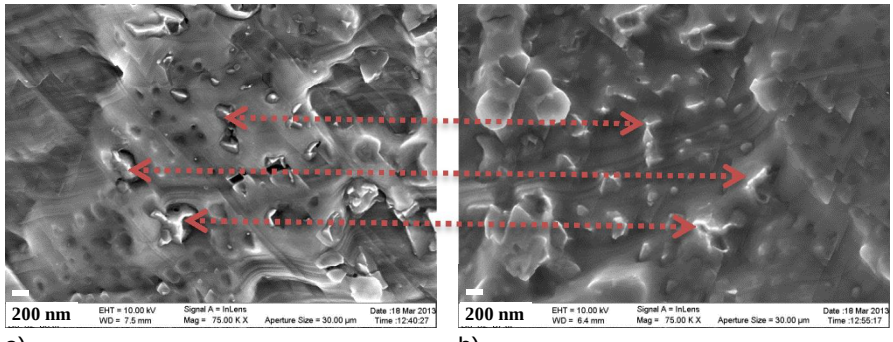

a) b)

Figure 55. A comparison of the both sides of the mating fracture surfaces of Alloy 52, a) and b). The secondary electron (SE) SEM image illustrates how the tetrahedron-shaped carbides, shown in a), exhibit signs of local plastic deformation when they have detached from the opposing fracture surface, side b).

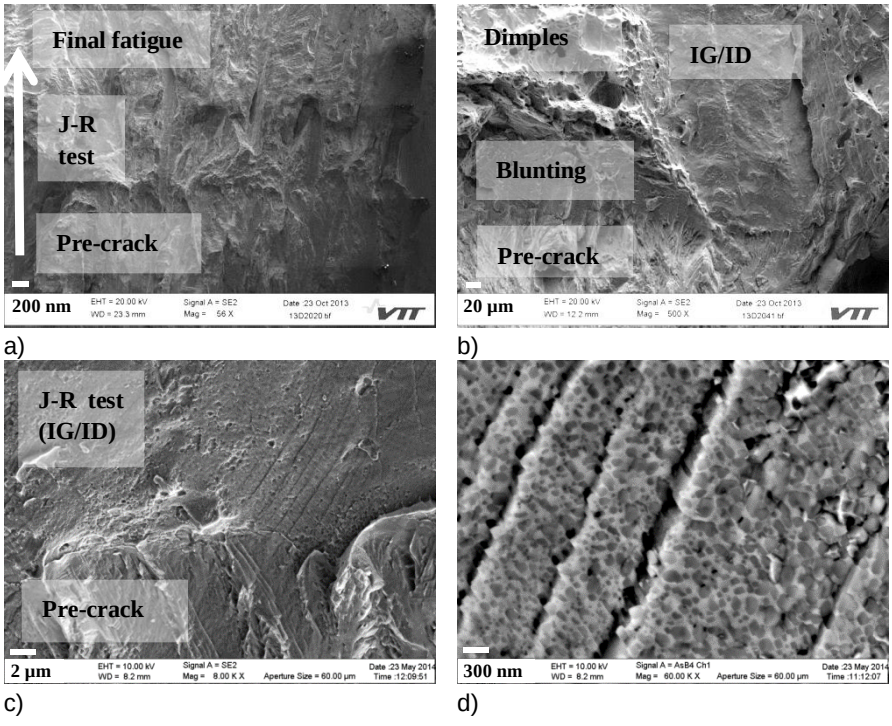

Figure 56. In a) and b) general view of the fracture surfaces of an Alloy 52 DMW specimen tested in hydrogenated (100 cm^3 H_2/kg H_2O) low temperature water, secondary electron (SE) SEM images. Crack growth direction is upwards in the images. Cracking during the test is mostly ductile dimple fracture with some areas of IG/ID fracture. IG/ID fracture occurs without significant blunting when there is a similar orientation between the pre-crack tip and grain/dendrite boundary, as shown in b) and c). Secondary electron (SE) c) and electron back-scatter (BSE) d) SEM images show the fine microstructure with a large amount of carbides observed on the IG/ID fracture surface. Image d) illustrates the $M_{23}C_6$ carbide structure on the IG/ID fracture surface of Alloy 52 DMW.

EDS spot analyses were performed in order to confirm that the small carbides observed on the IG/ID areas of the fracture surfaces of Alloy 52 are Cr carbides. Although the spot is larger than the carbide particles, the relative difference between the particles and the matrix can be used as guidance when selecting between potential carbide types. The spot analyses were measured from an area similar to that presented in Figure 56 d). The results are presented in Figure 57 a) and b). The red curves represent the spot analysis of the matrix and the blue curves represent the spot analysis of a small carbide. The curves show that the

carbides contain more Cr and less Ni and Fe than the matrix, indicating that the particles are Cr carbides.

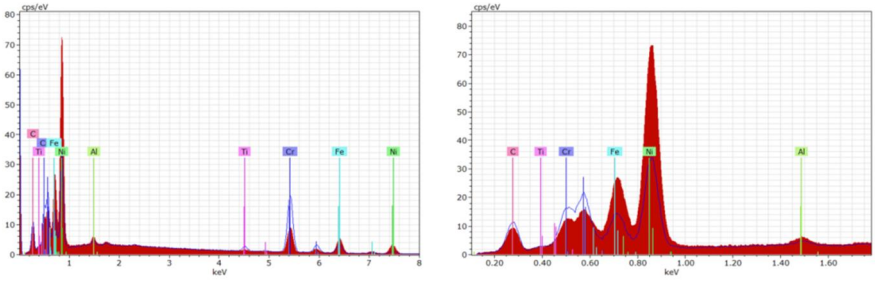

a) b)

Figure 57. EDS spot analyses from IG/ID fracture surface area. The whole EDS spectrum is presented in a) and a detail of the spectrum taken from the low voltage range in b). The red curves represent the matrix and the blue curves represent the carbide.

5.7 EBSD study on TEM samples

The TEM samples of as-welded Alloy 182 and 52 DMWs were studied using EBSD (electron backscatter diffraction) in order to examine the differences between dendrite and solidification grain boundaries. Euler maps were determined in order to examine the grain and dendrite orientations and angular differences.

The results for DMW Alloy 182 are presented in Figure 58 where an Euler map is shown with the corresponding EBSD pattern quality map. It was observed that Alloy 182 DMW exhibited boundaries of only one kind of appearance. This was observed also when the sample was studied with SEM (Figure 59). The boundaries, that are believed to be solidification grain boundaries, show a tortuous appearance with large grain boundary precipitates. Intragranular precipitates or inclusions and fine intergranular precipitates are also visible.

The EBSD results for Alloy 52 DMW are presented using two different magnifications in Figures 60 and 61. Solidification grain boundaries and dendrite boundaries are clearly visible in the pattern quality maps of Alloy 52 DMW and thus comparison with Euler maps, that show the grain orientation differences, helps to attain information regarding distinction between the different boundaries. The Euler maps of the DMW sample of Alloy 52 demonstrate that the dendrite boundaries, that are clearly visible in the EBSD pattern quality maps, are low angle boundaries and in fact they are not even clearly visible in Euler maps.

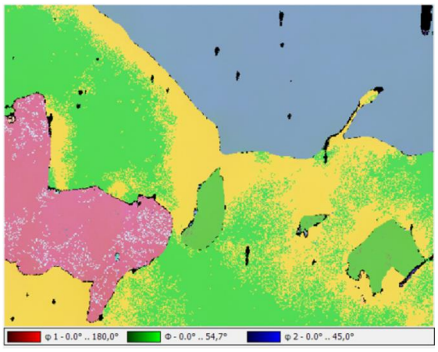

a)

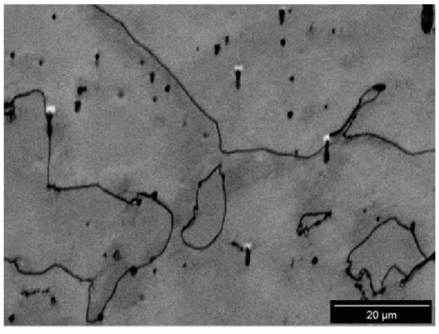

b)

Figure 58. EBSD results for an area of a TEM sample surface of Alloy 182 DMW. Euler map in a) and EBSD pattern quality map in b) illustrating the grain orientations and grain boundaries. Dendrite boundaries are not clearly visible.

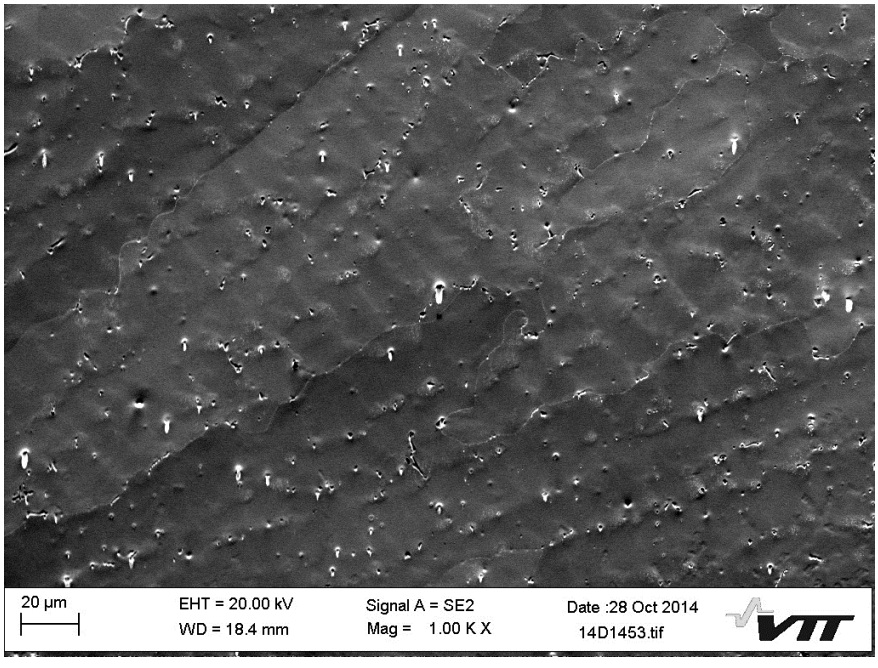

Figure 59. A SEM image of secondary electrons from the surface of a TEM sample of as-welded Alloy 182 DMW. The specimen was tilted in order to enhance the surface morphology. The figure illustrates the tortuous grain boundary structure of Alloy 182 including a large amount of MC-type primary carbides.

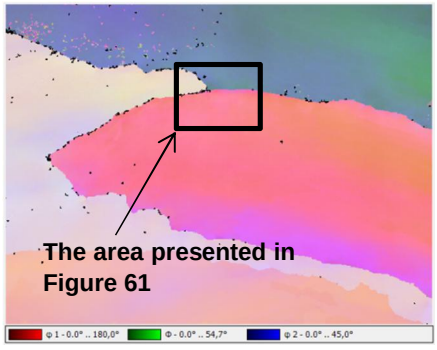

a)

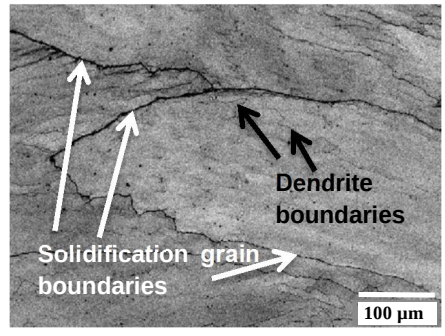

b)

Figure 60. EBSD results for an area of a TEM sample surface of Alloy 52 DMW. The Euler map, showing the differently orientated grains, is presented in a) and the EBSD pattern quality map in b). The solidification grain boundaries and dendrite boundaries are visible in pattern quality map.

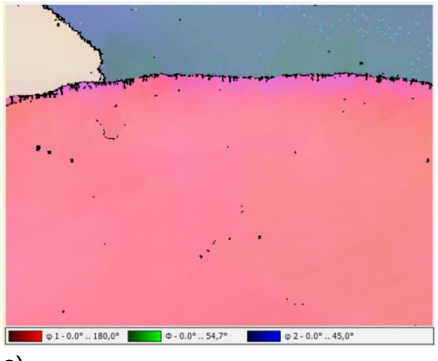

a)

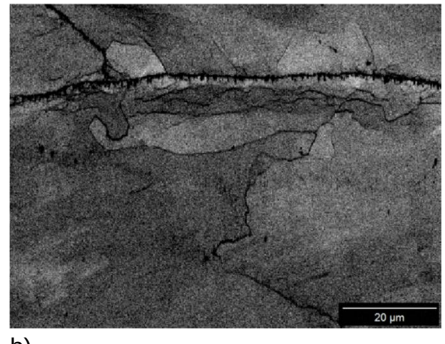

b)

Figure 61. EBSD results for a smaller area of a sample surface of Alloy 52 DMW. The Euler map, showing the differently orientated grains, is presented in a) and the EBSD pattern quality map in b). The grain and dendrite boundaries are visible in pattern quality map. The dendrite boundaries exhibit small angular differences and they are poorly distinguished in the Euler map.

5.8 TEM examinations

TEM was performed for DMW samples of Alloys 182 and 52 in both as-welded and post-weld heat treated conditions. The main focus of the study was to charac-

terize the grain and dendrite boundaries. The grain boundary carbides were analysed by using TEM EDS.

5.8.1 TEM of Alloy 182 DMW

The grain and dendrite boundaries showed a few different features in the Alloy 182 AW sample. Most of the dendrite boundaries were decorated by small precipitates as illustrated in Figure 62. Using a larger magnification (Figure 63) it can be seen that those precipitates sometimes exhibit an irregular shape and sometimes some geometrical shapes can be observed. However, the appearance of the carbides depends on the viewing angle and in some cases it was observed by tilting the TEM specimen that the same carbides seemed irregular shaped from an angle and more geometric from another angle. It is also notable that both surfaces of the studied boundaries appear to be closely attached, i.e., the material has not been etched more from the boundary zone compared to the matrix in sample preparation. The small precipitates were analysed by using TEM EDS and they were found to contain Nb. No increased Cr contents were measured from the precipitates compared to the matrix, thus the precipitates are most likely MC-type Nb carbides. There were also boundaries, where almost no carbides were detected, as shown in Figure 65. Some small irregular-shaped precipitates were detected at these boundaries.

The features observed in the post-weld heat treated sample of Alloy 182 were somewhat different compared to the as-welded material. Unlike in the AW sample, there were boundaries where Cr-rich, tetrahedron-shaped carbides were observed. The precipitates in Figure 67 were analysed by using EDS and the vast majority of them were detected to contain large amounts of Cr. Tetrahedron-shaped Cr-rich $C_{23}M_6$ carbides are distinctively illustrated in Figure 68. Some precipitates were also Nb-rich, such as the dark appearing thin carbide on the lower right of Figure 68. It was also evident that the grain boundary area was etched away due to the sample preparation, where Cr-rich tetrahedron-shaped carbides were observed.

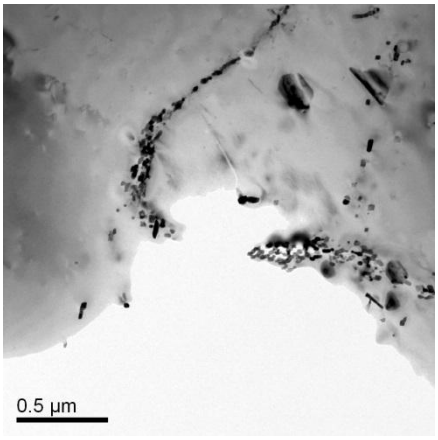

Figure 62. A TEM image of a typical dendrite or grain boundary observed in Alloy 182 in AW state. The boundary contains a large amount of precipitates that according to EDS are Nb-rich carbides.

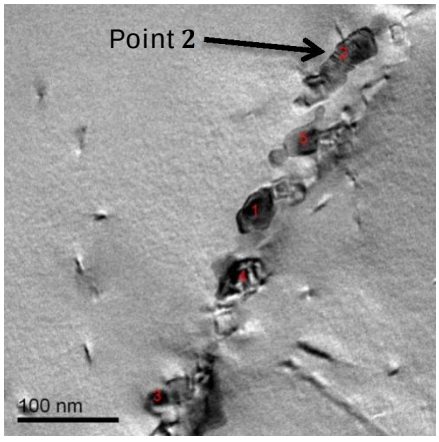

Figure 63. A TEM image from a typical dendrite or grain boundary observed in Alloy 182 in AW state with higher magnification. The boundary, most probably dendrite boundary, is decorated by almost continuous carbides that were analysed to be Nb-rich (points 1–5).

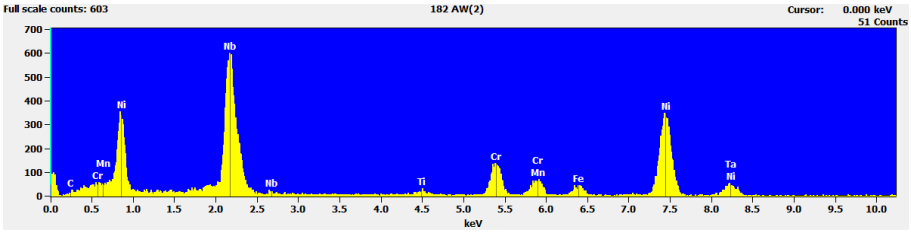

Figure 64. A TEM EDS analysis of a carbide, measured from the point 2 in Figure 63.

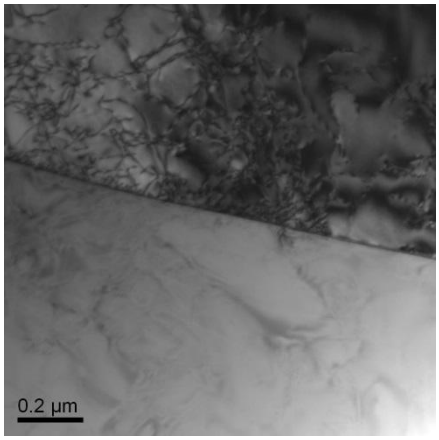

Figure 65. A TEM image of a grain boundary observed in as-welded Alloy 182. Only very few small carbides were detected on this boundary.

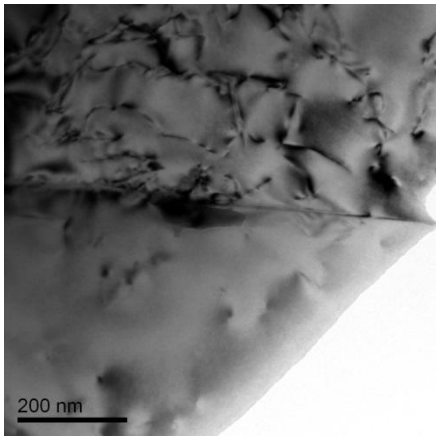

Figure 66. A higher magnification TEM image showing a grain boundary of AW Alloy 182 where just a few precipitates were detected. The carbide appearing dark in the middle of the picture at the grain boundary contains Nb and appears to have an irregular shape.

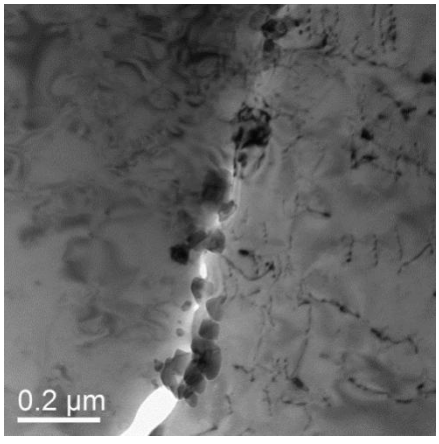

Figure 67. A TEM image showing a grain boundary of PWHT Alloy 182 with precipitates. The majority of the precipitates were detected to be Cr-rich carbides.

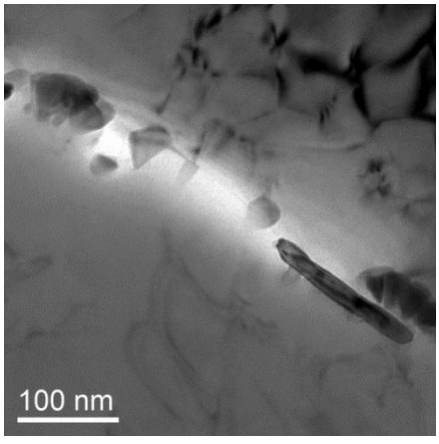

Figure 68. A larger magnification TEM image showing a grain boundary of PWHT Alloy 182 with precipitates. The majority of the precipitates were detected to be Cr-rich carbides. A rod-like Nb-rich carbide, appearing dark in the image and oriented along the grain boundary, was also observed.

5.8.2 TEM of Alloy 52 DMW

The grain boundaries of the samples of Alloy 52 were decorated by tetrahedron-shaped precipitates that were analysed to be Cr-rich. Such grain boundary is presented in Figure 69 and a detail of the same grain boundary showing tetrahedron-shaped carbides and a smaller Ti-rich carbide in Figure 70. The Cr-rich carbides, which most probably are $M_{23}C_6$ -type, grow sometimes their tips pointing towards right and sometimes towards left in Figure 69. The size of the Cr-rich carbides was measured to be in the range of 100–300 nm. The Ti-rich carbides were smaller than 100 nm. The EDS analyses of the different types of carbides are presented in Figures 71 and 72.

Post-weld heat treatment did not seem to have a significant effect on the grain boundary morphology of Alloy 52 based on the performed TEM examinations. The $M_{23}C_6$ carbides that can be seen in Figure 73 are typically in the same size range as the ones observed in the AW state material, although some carbide growth was observed at some locations.

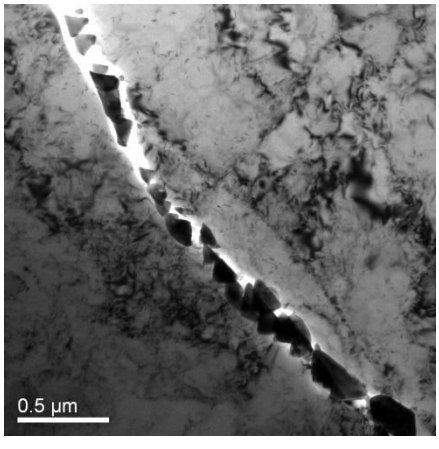

Figure 69. A TEM image of a grain boundary of as-welded Alloy 52.

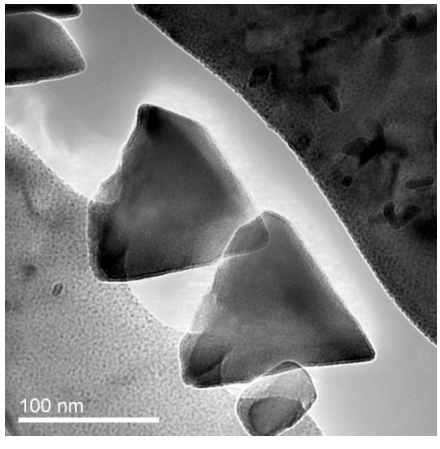

Figure 70. A TEM image of carbides observed at a grain boundary of as-welded Alloy 52. The tetrahedron-shaped carbides were detected to be Cr-rich and the smaller carbide is Ti-rich.

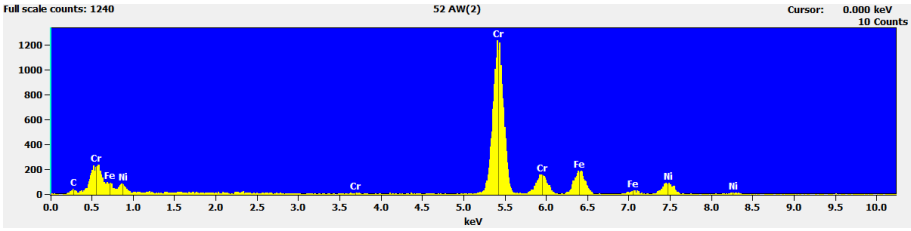

Figure 71. A TEM EDS analysis of a tetrahedron-shaped precipitate shown in Figure 70. The precipitate is Cr-rich.

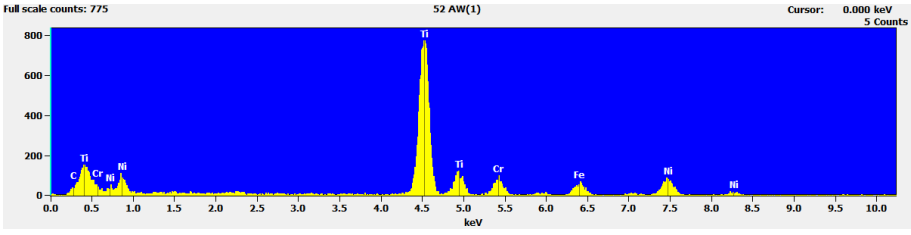

Figure 72. A TEM EDS analysis of a smaller precipitate next to a tetrahedron-shaped precipitate shown in Figure 70. The precipitate is Ti-rich.

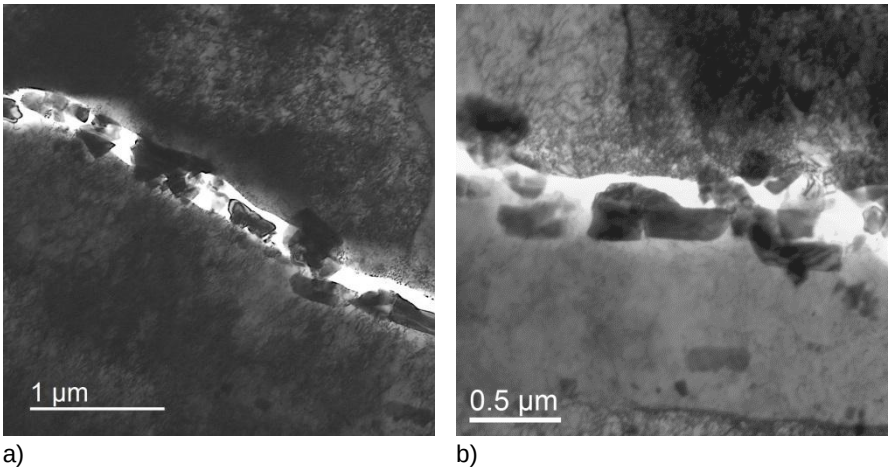

a) b)

Figure 73. A TEM images (shown in a) and b)) of a grain boundary of post-weld heat treated Alloy 52 showing Cr-rich $M_{23}C_6$ carbides.

6 Discussion

6.1 J-R tests

The fracture resistance of nickel-based Alloy 182/82 and Alloy 152/52 weld metals decreases in hydrogenated low-temperature water, as has been previously reported by a few researchers but most extensively by Mills and Brown. Even low hydrogen contents (5 cm^3 H_2/kg H_2O) are sufficient to cause intergranular/interdendritic cracking and decrease the fracture resistance of Alloy 182 (Herms et al., 2009). The results of this study confirm the degrading effect of hydrogen on fracture resistance of nickel-based alloy weld metals. It has also been shown in this study that higher hydrogen content results in lower J_Q values. As presented in Figure 74, all the studied nickel-based alloy weld metals showed a similar trend, regarding the effect of hydrogen content of the water, but to a different extent. Thus, a general observation is that fracture resistance of all the studied nickel-based alloys is decreased by hydrogenated low temperature water, although in the case of Alloy 52 high hydrogen contents are needed in order to induce LTCP. Alloy 182 exhibits the highest susceptibility to LTCP, whereas higher Cr Alloys 152 and 52 exhibit higher fracture resistance values, in general. However, when tested with 100 cm^3 H_2/kg H_2O, all-weld metal Alloy 52 specimens showed extensive IG cracking and J_Q values that were similar to those of Alloy 182.

The effect of pre-exposure at the reactor operation temperature to the LTCP susceptibility has not been extensively studied thus far. Herms et al. (2009) reported that pre-exposure at 320 °C for 250 or 1000 h did not have a significant effect on the LTCP behavior of Alloys 182 and 152 at low hydrogen contents (3–5 cm^3 H_2/kg H_2O). In the present study low hydrogen content (5 cm^3 H_2/kg H_2O) pre-exposure (30 days, about 720 h) was studied for DMW specimens of Alloy 152, and the attained results were somewhat similar with or without the pre-exposure, although there was a slight increase in the average fracture resistance values due to the pre-exposure (Figure 28). Pre-exposure was studied with a moderate hydrogen content (30 cm^3 H_2/kg H_2O) for DMW specimens of Alloys 182, 152 and 52 and the results obtained with and without pre-exposure are compared in Figure 75. Alloys 182 and 152 showed a slight increase of the fracture resistance due to the high temperature pre-exposure. DMW material NGW Alloy 52 was also studied

in the same environments with Alloys 182 and 152, but no effects of the environment could be measured due to the limitations of the test equipment.

When all the obtained results for the different pre-exposures (24 h and 30 days at 300 °C) with different hydrogen contents of the water are compared with the results obtained without pre-exposure, a clear trend can be observed. It seems that at least for Alloys 182 and 152 the high temperature water pre-exposure increases the fracture resistance of the material regardless of the hydrogen content of the environment (Figures 26 and 28). This result indicates that the hydrogen content of the water and the amount of trapped hydrogen in the material both play important roles in the reduction of the fracture resistance. The diverging behavior of Alloy 82 (Figure 27) is unclear, but it may be due to significant scatter of the obtained results for this material.

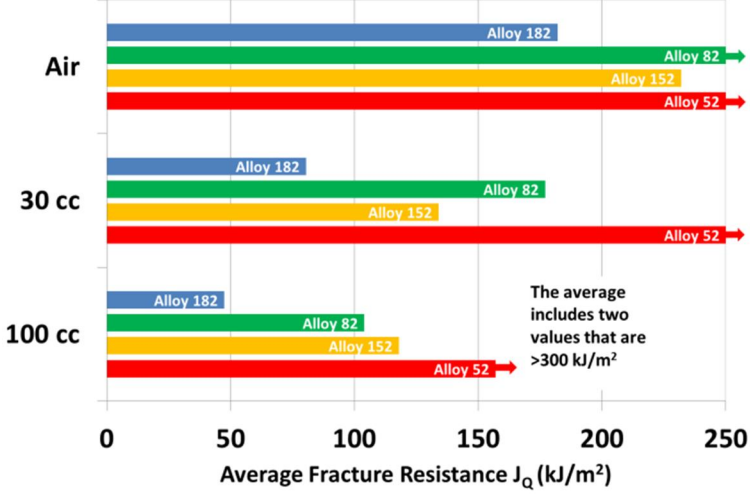

Figure 74. Average fracture resistance (J_Q) values for Alloys 182, 82, 152 and 52 tested in room temperature air and in 55 °C water (200 ppm H_3BO_3 and 2.1 ppm LiOH) with hydrogen contents of 30 and 100 cm^3 H_2/kg H_2O.

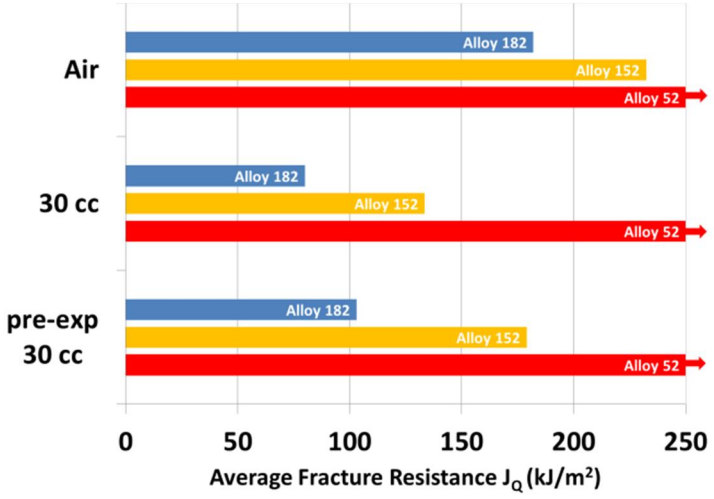

Figure 75. Average fracture resistance (J_Q) values for Alloys 182, 152 and 52 tested in room temperature air and in 55 °C water (200 ppm H_3BO_3 and 2.1 ppm LiOH) with hydrogen content 30 cm^3 H_2/kg H_2O, with and without pre-exposure to high temperature (300 °C) hydrogenated (30 cm^3 H_2/kg H_2O) water. Only DMW samples are included in this graph, except for the air tests of Alloys 182 and 52 which were measured with all-weld metal specimens.

The effect of Post-Weld Heat Treatment (PWHT) was studied for DMW specimens of Alloys 182 and 52. Hydrogen contents of 30 and 100 cm^3 H_2/kg H_2O were applied. The obtained results for both AW and PWHT specimens of Alloy 182 are compared in Figure 76 in terms of average fracture resistance. The fracture toughness behaviour of the different materials has been evaluated in this study by comparing fracture resistance J_Q values. However, J_Q (or J_{IC}) is a parameter that is very sensitive to the pre-crack tip location relative to the microstructure and also to possible crack propagation measurement inaccuracy. Therefore, J_{1mm}, i.e. the value of J-integral at Δa of 1 mm, is sometimes used for DMW materials (Hänninen et al., 2014) and basically it can be used for any kind of structural materials (Wallin, 2011) to describe the fracture resistance of a specimen because the *dJ/da* of the J-R curve typically decreases with increasing Δa, as schematically illustrated in Figure 17. When comparing the J_Q values of Alloy 182 in AW and PWHT conditions, the AW samples exhibit somewhat lower susceptibility to hydrogen-induced LTCP in both applied environments, although the difference in J_Q between AW and PWHT material state is marginal. On the contrary, PWHT specimens of Alloy 182 exhibit higher fracture resistance when J_{1mm} values are considered. This is due to a higher tearing resistance of PWHT specimens and also due to slightly different shape of the J-R curve observed for AW and PWHT specimens, which may be related to the different mechanism of fracture observed in the SEM study (TG vs. IG/ID). When the fracture occurs partly with a transgranular

mechanism, as in the case of DMW Alloy 182, the energy required for initiation of the stable crack growth is not significantly different than when the fracture occurs with an intergranular mechanism. However, in specimens where TG fracture occurs alongside with IG/ID fracture the tearing resistance is higher than in specimens that exhibit fully IG/ID fracture in the J-R test.

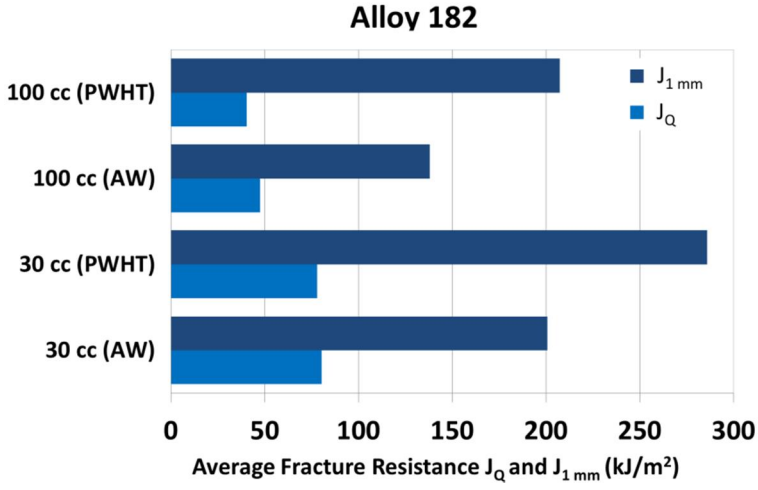

Figure 76. Comparison of J-R test results (J_Q and $J_{1\ mm}$ values) of Alloy 182 specimens in both AW and PWHT conditions.

6.1.1 Scatter of fracture resistance (J_Q) values

The obtained fracture resistance (J_Q) and tearing modulus (T at Δa=0.5 mm) values sometimes vary significantly within parallel tests, i.e. within tests conducted for the same material in the same environment. It is assumed that there are at least a few different parameters affecting the scatter.

The most important factor in scatter is probably the inhomogeneity of the tested weld metals. Welds are always inhomogeneous regarding local thermal history and microstructure. The location of the fatigue pre-crack tip regarding the microstructure has an effect on the crack initiation toughness J_{IC} (or J_Q) because the amount of the pre-crack tip blunting prior to onset of the stable crack growth is essential for the attained J_{IC} or J_Q value, which becomes evident from Figure 17. In the case of nickel-based alloy weld metals, the scatter in environment-affected J-R test results depends on pre-crack tip location and local dendrite and grain orientation. It was observed in this study that intergranular cracking occurs most likely at locations where the fatigue pre-crack tip is favourably located compared to the microstructure and grain orientation. This observation is similar to what has

been observed in SCC crack growth tests with CT specimens of Alloy 82 (Guerre et al., 2011). In multipass welds it is difficult to determine the exact location of the pre-crack tip prior to testing regarding microstructure and grain orientation. The SCC crack growth test results obtained for Alloy 182 in simulated PWR environment by Bamford et al. (1999) clearly show that the SCC cracks grow significantly faster along the dendrite growth direction, i.e. T-S and L-S orientations, than when the crack grows across the dendrites (T-L and L-T orientations). Having a look at Figure 19 (welding sequence of the all-weld metal test blocks) and Figures 20–22 (cross-sections of the DMW samples), and considering the local microstructural variations, it is obvious that the local dendrite orientation may vary significantly from specimen to specimen and from a pre-crack tip region to another. Thus, a nominal orientation of L-S or T-S does not tell the whole truth in this case but has of course relevance if a larger number of results are considered for each orientation.

The slopes of the J-R curves of different nickel-based alloy weld metals vary markedly even in the blunting line part within a test series conducted at a certain environment because of two reasons: firstly because the tested materials have different flow stress values, and secondly because the transition from transgranular fatigue pre-crack into IG cracking occurs in many cases without significant blunting, which is illustrated for example in Figure 56 b).

Scatter is a typical feature for austenitic materials in J-R testing, as can be observed from the data obtained for austenitic type 304 and 316 stainless steels that is plotted in graph presented in Figure 77 (originally presented by Mills, 1997). The graph shows that nominally similar materials can exhibit a very large scatter in J_{IC} values (from below 200 to almost 2000 kJ/m^2) as well as in dJ/da. In the case of wrought metals, heat-to-heat variability is associated with material orientation (Figure 78), differences in the density and morphology of inclusions that serve as microvoid nucleation sites and, to some extent, matrix strength.

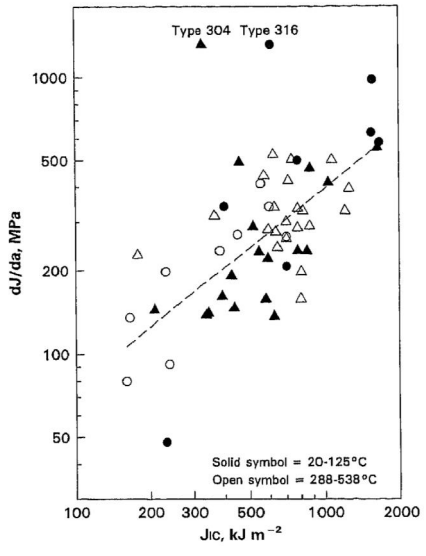

Figure 77. Scatter of the results obtained for austenitic stainless steels type 304 and 316 in J-R tests (Mills, 1997).

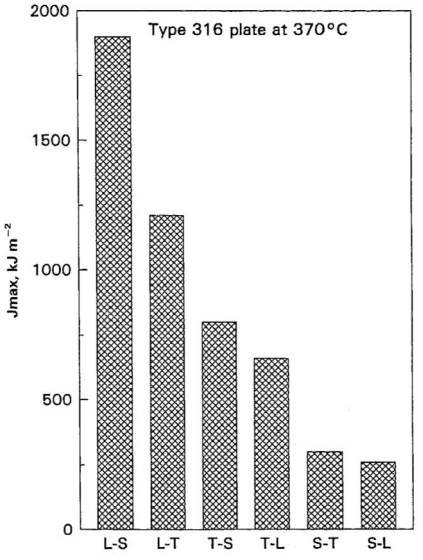

Figure 78. Effect of crack orientation on J_{max}, which corresponds to value of J at maximum load (Mills, 1997).

Scatter in this study is believed to be caused by inhomogeneity of the test materials for a large part, but actually scattering of J-R test results occurs even in homogeneous materials. Wallin (2011) presents tearing resistance data obtained from multi-specimen J-R tests for three different ductile homogeneous materials. All three materials show that the proportional scatter of the tearing resistance is large in the beginning of crack growth and decreases towards a constant value for larger crack growths. When the scatter of the tearing resistance data is considered as cumulative distributions it appears that the scatter is approximately normally distributed.

Determination of J_{IC} or J_Q is very sensitive to inaccuracy of crack length measurement. Thus, the final crack lengths measured by applying potential drop method were always corrected by using an image of the fracture surface. However, the cracking path is not following a straight plane as assumed when measuring the actual crack growth from a flat projection, whether it is an image or a view through a microscope. J-integral essentially measures the absorbed energy that is needed for crack propagation, and in the case of this study the difference between the true length of a cracking path and the length measured from a projection image of a crack may vary significantly because welds usually exhibit uneven fracture surfaces.

6.1.2 Differences between the all-weld metal and DMW results

Both all-weld metal and DMW specimens of Alloys 182, 152 and 52 were tested with 30 cm^3 H_2/kg. It was observed that both all-weld metal Alloy 182 and dissimilar metal weld Aalto 182 behaved very similarly in J-R tests. The J-R response of Alloy 152 was also consistent regardless of the test block, i.e., all-weld metal or DMW, although the scatter of the J_Q values was larger in the case of Alloy 152 than in Alloy 182.

Brown and Mills (1999) observed that all of the nominally similar EN52 weld metal specimens they tested did not exhibit a susceptibility to LTCP. Only 3 of the total of 8 tested specimens fractured with an intergranular mechanism. Also in this study the J-R test response and LTCP susceptibility varied for Alloy 52 specimens. All of the 3 all-weld metal specimens tested with hydrogen content 100 cm^3 H_2/kg H_2O showed significant LTCP susceptibility with fracture surfaces consisting almost completely of intergranular cracking. However, only one of the 3 DMW specimens tested with hydrogen content 100 cm^3 H_2/kg H_2O exhibited intergranular cracking and the fracture surface of the most LTCP susceptible specimen showed only partly intergranular appearance. Scatter may have an impact on these results as well, since the macroscopic appearance of Alloy 52 is uneven, as seen in Figure 54 a) and the grain size varies significantly, as seen in Figure 43. Nonetheless, if the results for 24 h pre-exposed all-weld metal Alloy 52 specimens, tested in 55 °C water with 100 cm^3 H_2/kg H_2O, are taken into account, it seems that the all-weld metal specimens are more susceptible to LTCP than DMW specimens. However, the limited amount of tests does not provide a possibility for a statistical assessment.

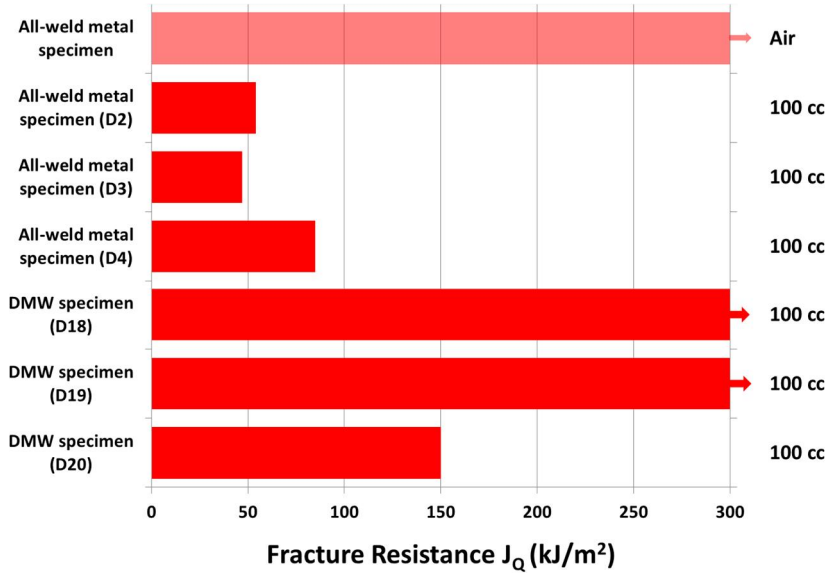

Figure 79. Comparison of the J-R test results obtained for all-weld metal and dissimilar metal weld specimens of Alloy 52.

6.2 Hardness measurements

The measured Vickers hardness values did not show large differences, although the hardness of the KAIST 152 was somewhat higher than the other obtained HV1 values, which indicates that the residual strains may be higher in that material than in all-weld metal Alloy 152. The carbon content of KAIST 152 is also slightly higher than that of all-weld metal Alloy 152 (0.025 in KAIST 152, 0.02 in all-weld metal Alloy 152) and that has some effect on the Vickers hardness. Post weld heat treatment had an opposite effect on Alloy 182 and 52 DMWs. The decrease of hardness of NGW Alloy 52 (203 → 191 HV1) is believed to be caused by relaxation, whereas the increase of the hardness of Aalto Alloy 182 (208 → 227) is probably caused by carbide growth. However, the effect of PWHT on the Vickers hardness was quite small and measurements from the different parts of the test material blocks, even when measured at the mid-thickness of the weld, may result in varying results. In addition, the different materials of Alloy 152, i.e. all-weld metal and KAIST DMW, did not exhibit a clear difference in J-R tests. The comparable results obtained for the different materials of Alloy 152 in low temperature water with 30 and 100 cm^3 H_2/kg H_2O were very similar, as can be seen in Figures 91–94.

6.3 Cracking path of Alloys 182 and 52

It was observed that in both Alloys 182 and 52 the fracture surface consisted of areas where carbides were densely distributed and of areas that showed small carbide-sized pits and some signs of carbide detachment that had involved significant plastic deformation (Figures 51 f) of Alloy 182 and 54 d) of Alloy 52).

6.3.1 Cracking path of Alloy 182

Cracking during the J-R tests occurred mostly along the grain or dendrite boundaries in Alloy 182 all-weld metal when tested in low temperature water with high hydrogen content. A carbide-rich fracture surface layer was observed, particularly in the case of PWHT specimens of Alloy 182 DMW, as presented in Figure 51 e) and f). IG/ID fracture surface of the AW Alloy 182 specimens consists of areas of rather small (~30–200 nm in diameter), globular carbides and areas of carbide-shaped pits, as shown in Figure 80.

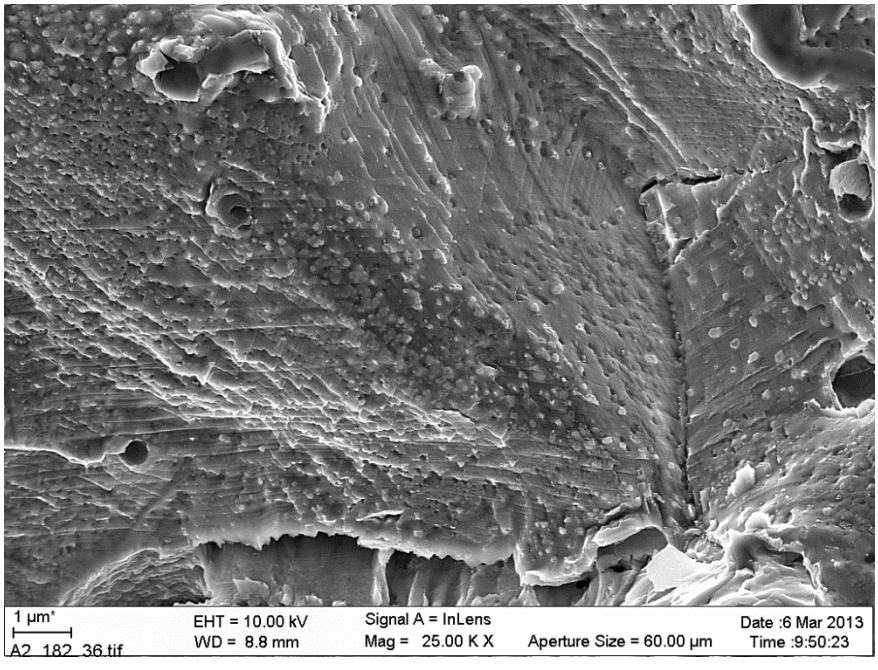

Figure 80. SEM image (SE) of the fracture surface of AW Alloy 182 all-weld metal tested in low temperature water with high hydrogen content (100 cm^3 H_2/kg H_2O). Small globular carbides as well as carbide-shaped pits can be seen on the IG/ID fracture surface. The carbide size ranges from about 50 nm to 200 nm.

Transgranular cracking was found to occur in Alloy 182 DMW tested with 30 and 100 cm^3 H_2/kg H_2O. Similar fracture surface appearance was observed for all-weld metal Alloy 82 specimens at some locations. This kind of surface appearance was never uniform, but consisted of alternating areas of IG/ID and TG fracture. Somewhat similar cracking was observed also by Mills et al. (2001) for annealed Alloy 82H weld metal (Figure 81 a)). The TG cracking observed in this study for Alloy 82 all-weld metal (Figure 81 b)) and Alloy 182 DMW has a similar appearance (TG areas in Figure 50 b)).

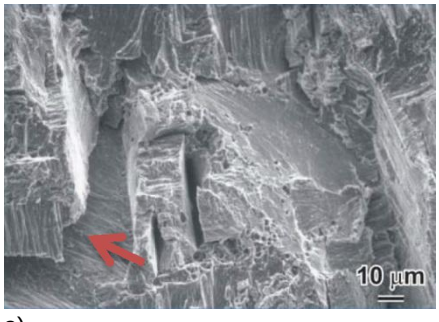

a)

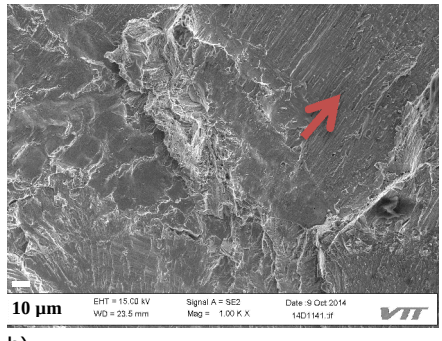

b)

Figure 81. A comparison of SEM images of TG fracture observed by Mills et al. (2001) for annealed Alloy 82H weld metal (in a) and that observed in this study for as-welded Alloy 82 weld metal (in b).

6.3.2 Cracking path of Alloy 52

The cracking observed in the J-R tests conducted in low temperature water with high hydrogen content was predominately intergranular or interdendritic, although in some cases very high fracture resistance (J_Q) and corresponding ductile appearance on the fracture surface was maintained.

The fracture surfaces of the specimens corresponding to lower J_Q values can be studied at three main levels. In a general view (Figure 82) the appearance of the fracture surface is uneven including steep forms and many different planes on which the fracture occurs. In addition, secondary cracking is observed in some specimens. The orientation of the grains changes to some extent from specimen to specimen due to slight differences of the pre-crack locations in weld thickness direction and varying shape of the weld beads in a multipass weld, which is also evident on the fracture surfaces. It is already clear from this general view that the fracture type is intergranular or interdendritic, because the fracture seems to follow the boundaries and no dimples are observed.

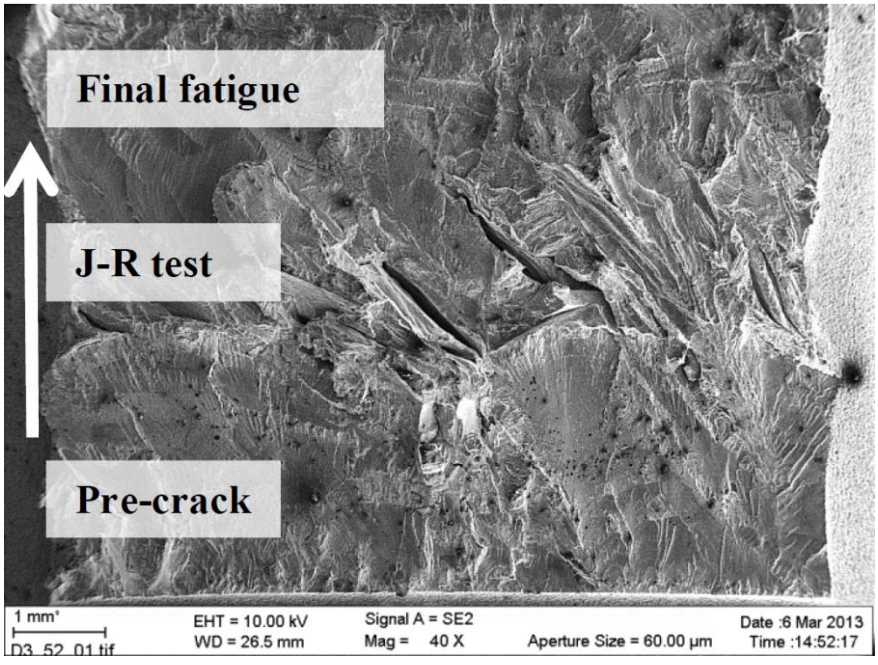

Figure 82. A general view of the fracture surface of an all-weld metal Alloy 52 specimen (D3) tested in low temperatutre (55 °C) water with high hydrogen content (100 cm^3 H_2/kg H_2O).

When the fracture surfaces are studied in a moderate magnification (Figure 83), more features of the fracture surface become visible. The IG/ID fracture surfaces are rather smooth at an area of each grain/dendrite. This local smooth appearance can be a feature of a grain boundary more than that of a dendrite boundary, which would tend to have a more tortuous appearance. The crack advances along the grain boundaries leaving some ligaments which fracture in a ductile manner when the crack tip opens and the strain of the ligaments reaches the material ductility limit.

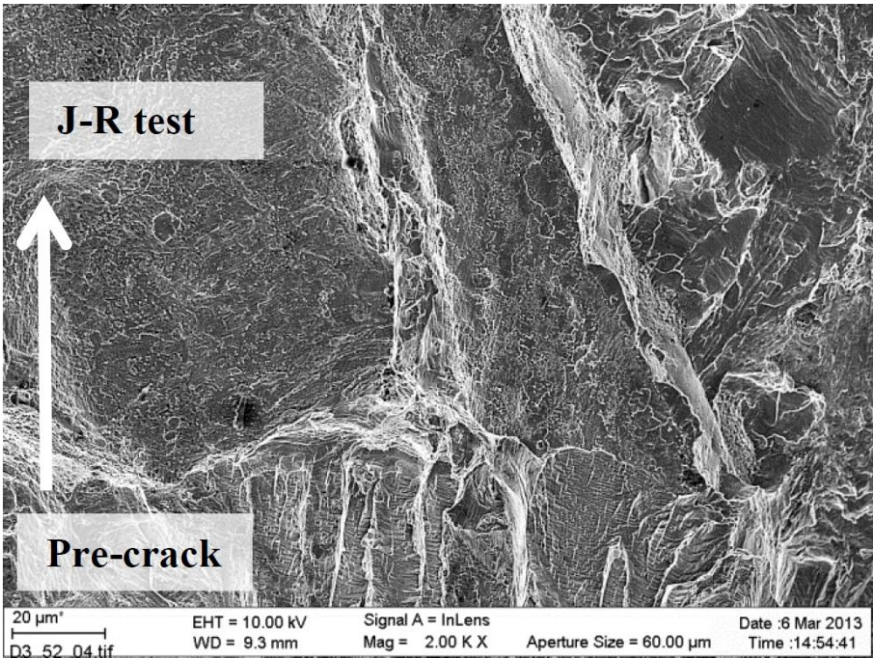

Figure 83. A moderate magnitude view of the fracture surface from the area of transition from fatigue pre-crack to J-R test region. The image is taken from an Alloy 52 specimen (D3) tested in low temperatutre (55 °C) water with high hydrogen content (100 cm^3 H_2/kg H_2O).

The intergranular fracture surfaces of Alloy 52 weld metal specimens have features at a very small scale that can only be detected in high magnification SEM or TEM. The intergranular fracture surfaces of Alloy 52 were observed to have a layer-like structure in a scale of some 100–300 nm. The crack deviates from side to side of the grain boundary structure leaving areas of a carbide-rich layer to the both sides of the generated surface. This structure is present at the both sides of the opposing specimen halves and they match with each other very precisely. As seen in SEM images (Figure 55), the intergranular fracture surface structure of Alloy 52 includes a large amount of tetrahedron-shaped precipitates and a smaller amount of sporadically located, very small globular precipitates. The fracture surface structure is illustrated also in the 3D images shown in Figures 84 and 85.

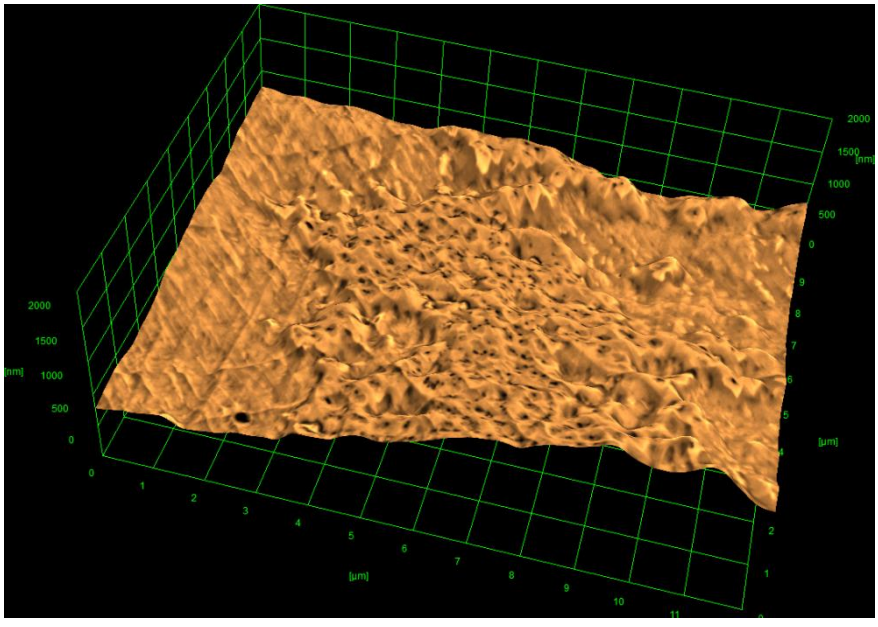

Figure 84. A 3D SEM image illustrating the carbide-rich layer at the intergranular fracture surface. The image is taken from an Alloy 52 specimen (D3) tested in low temperatutre (55 °C) water with high hydrogen content (100 cm^3 H_2/kg H_2O).

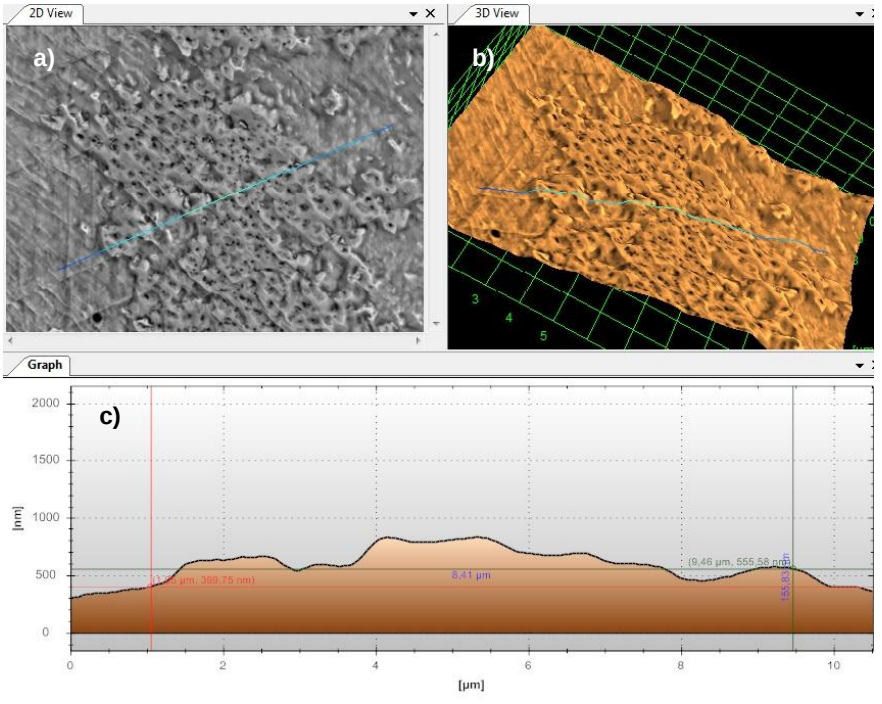

Figure 85. A SEM illustration of the intergranular fracture surface layer showing a 2D view of a selected fracture surface area a), a 3D view of the same area b) and a line profile graph over the surface layer c). The graph is drawn along the blue-green line presented in a) and b). The image is taken from an Alloy 52 specimen D3 tested in low temperatutre (55 °C) water with high hydrogen content (100 cm^3 H_2/kg H_2O).

6.4 Fractography and microstructural features of LTCP

The LTCP susceptibility of nickel-based alloys is affected by the microstructure of the material. Since it has been shown by Brown and Mills that both hydrogen from the water and from hydrogen precharging result in a dramatic reduction of toughness (Brown & Mills, 2002), the microstructural features governing hydrogen trapping and accumulation during loading are of great interest.

6.4.1 Grain boundary tortuosity

The intergranular or interdendritic fracture surface appearance was observed in this study to be different in Alloys 182 and 52. The IG/ID fracture surfaces of Alloy 52 specimens have a fine structure with macroscopically rather smooth appear-

ance, whereas the IG/ID fracture surfaces of Alloy 182 have more tortuous appearance. SEM images showing the typical intergranular fracture surface appearances of Alloys 182 and 52 are presented in Figure 86 a) and b), respectively.

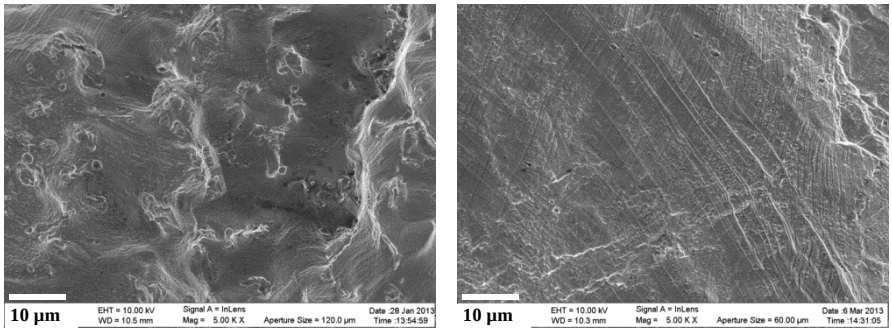

a) b)

Figure 86. SEM images showing a comparison of the IG/ID fracture surface morphologies of Alloys 182 a) and 52 b), tested in low temperature water with high hydrogen content (100 cm^3 H_2/kg H_2O). The appearance of the fracture surface of Alloy 182 is more tortuous than that of Alloy 52. Large Nb-rich carbides are present at the fracture surface of Alloy 182.

Similar comparison of Alloys 182 and 52 regarding the grain boundary tortuosity has been presented by Collins et al. (2004) with the exception that they presented images of cross-sections. Filler metals that contain sufficient amount of Nb will form NbC precipitates at the end of solidification. Since the NbC carbides form at the end of the solidification, they tend to pin the grain boundaries and thus grain boundary migration does not occur (Ramirez & Lippold, 2004).

Ramirez and Lippold formulated a theory for ductility-dip cracking (DDC). The grain boundary pinning plays a crucial role and explains the different DDC behaviour of Alloys 82 and 52. The effect of grain boundary pinning on the strain accumulation is schematically presented in Figure 87. In the case where no grain boundary carbides form, the grain boundaries are quite straight and the strain will accumulate at grain boundary triple points due to grain boundary sliding, as shown in Figure 87 a). In the case where the grain boundaries are straight and there are also intergranular precipitates, as in Figure 87 b), the strain will accumulate to the triple points and to the carbide-matrix interfaces. Primary carbides that precipitate at the grain boundaries, for example in Alloys 82 and 182, pin the grain boundaries and thus prevent grain boundary migration. The tortuous grain boundaries that result from grain boundary pinning provide the mechanical locking of the boundaries that effectively oppose grain boundary sliding. Strain distribution is different in the case of tortuous grain boundaries, as shown in Figure 87 c) (Ramirez & Lippold, 2004).

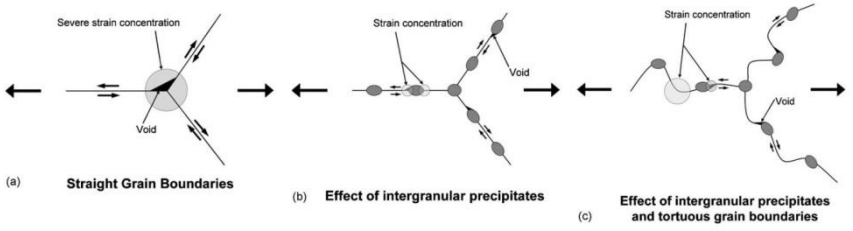

Figure 87. A schematic presentation of grain boundary strain accumulation as a function of boundary geometry and precipitation behavior (Ramirez & Lippold, 2004).

McCracken (2014) observed that increasing number of reheating cycles increases the DDC susceptibility of Alloy 52 welds. In that study wash passes were applied at some locations of a narrow groove weld in order to simulate multiple reheat cycles. Strong DCC response was observed in the weld layers below wash layers. Computer simulation was performed by SysWeld and that further confirmed that regions of high accumulative plastic strain were locations where DDC occurred.

Stress and strain distributions may have a significant effect to LTCP phenomenon in nickel-based weld metals because hydrogen accumulates to stress fields in the material (Pressoyre, 1983). If the residual strain is more evenly distributed to the grain boundaries of the weld metal, it may decrease the DDC susceptibility but it can increase the LTCP susceptibility. When crack propagates during J-R testing in low temperature hydrogenated water, hydrogen accumulates to the crack tip region and lowers the cohesion forces between metal atoms thus causing local embrittlement of the material (Mills et al., 1999). If the hydrogen is somewhat evenly distributed at the grain boundaries it does not need to diffuse long distances in order to reach the crack tip region and cause degradation of the fracture resistance. In addition, the strain concentration zones can serve as locations for hydrogen accumulation during loading in a J-R test specimen. It is assumed that the diverging LTCP behaviour of Alloys 182 and 52 may be at least partly explained by the different hydrogen trapping and accumulation properties of the materials due to grain boundary tortuosity.

6.4.2 Observations from the TEM study

The TEM study for Alloy 182 consisted of DMW samples that were in both AW and PWHT conditions. A fundamental difference between the observations made of AW and PWHT samples was that the grain or dendrite boundary carbides were constantly Nb-rich in the AW sample, whereas both Cr-rich and Nb-rich carbides were observed in the PWHT specimen. The tetrahedron-shaped carbides ob-

served in the PWHT specimen were Cr-rich and the Nb-rich carbides were rod-like or irregular-shaped. However, tetrahedron-shaped carbides were observed also in AW Alloy 182 fracture surface in SEM study. Making general conclusions about what are the typical carbides in AW and PWHT conditions is not reasonable based on TEM observations that cover a very limited volume of material.

The grain boundary carbides observed in Alloy 52 DMW were Cr-rich and Ti-rich. The grain boundary areas consistently showed an etched appearance, which indicates Cr depletion at the grain boundary region that was about 100–200 nm wide. Alloy 52 did not exhibit noticeable differences between the AW and PWHT conditions in the TEM study. Some indications of slight growth of $M_{23}C_6$ carbides were observed. Based on the TEM study it appears that the effect of PWHT on the grain boundary structure of Alloy 52 is very limited.

6.4.3 Carbide coherency

Yonezawa et al. (1993) showed that the coherent and incoherent carbides have different effect on IGSCC behaviour of Alloy X-750. In their study material with incoherent carbides cracked in SSRT tests performed in hydrogenated high temperature water, whereas material with coherent carbides did not crack. Hydrogen content (up to 40 cm^3 H_2/kg H_2O) of the water did not have an effect on IGSCC susceptibility in simulated PWR water, thus it was concluded that the carbide coherency is the dominating factor in the IGSCC susceptibility of Alloy X-750. The main reason for this kind of behaviour is that incoherent precipitates trap more hydrogen than coherent precipitates. Young and Scully (1997) studied hydrogen trapping in Alloy 600 and they also observed that coherent $M_{23}C_6$ carbides were weaker traps than incoherent pseudo-hexagonal M_7C_3 carbides. The comparison of coherent and incoherent TiC carbides in steel by Wei and Tsuzaki (2006) resulted in similar observation, i.e. the trapping activation energy and the binding energy increase as the incoherency of the carbides increases. Based on these results it can be concluded that incoherent primary carbides of MC-type are probably stronger traps for hydrogen than coherent $M_{23}C_6$ carbides. This explains the larger amounts of trapped hydrogen measured in Alloys 182 and 152 than in Alloy 52 that does not contain Nb and thus does not contain a significant amount of primary carbides.

Young et al. (2007) studied the ductility dip cracking (DDC) susceptibility of different Alloy 52 weld metals. In that study they presented a theory for ductility dip cracking that is schematically illustrated in Figure 88. According to Young et al. DDC of Alloy 52 is caused by local stresses that derive from $M_{23}C_6$ carbide precipitation. The carbide precipitation generates local stresses because of the lattice misfit between coherent $M_{23}C_6$ carbide and the matrix.

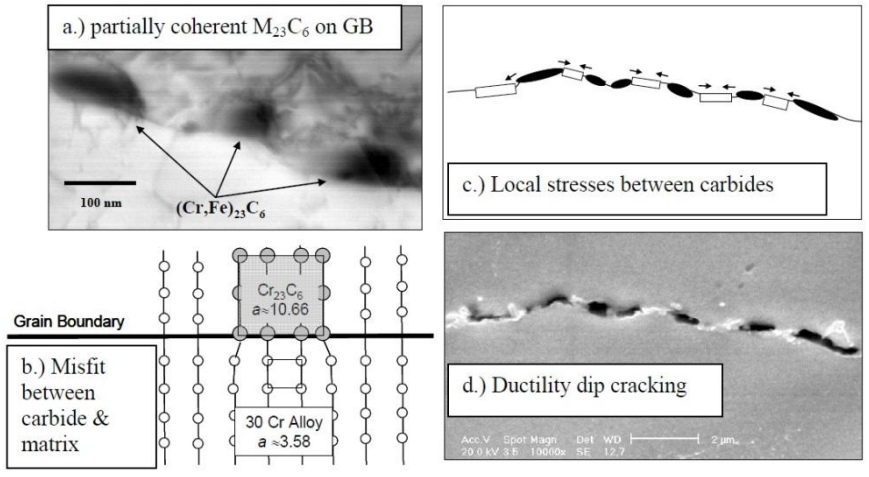

Figure 88. The origin of ductility dip cracking in Alloy 52 weld metal according to Young et al. (2007).

This kind of behaviour is interesting also in LTCP point of view because the carbide precipitation induces stresses and hydrogen accumulates to stress zones. These stress zones would be locations for hydrogen uptake from the water in the case of Alloy 52 and explain the LTCP susceptibility of Alloy 52 when tested with high hydrogen contents.

6.4.4 Cracking of MC-type carbides

The MC-type carbides that form during solidification are typically relatively large and irregular in shape. The SEM examinations of the fracture surfaces of Alloy 182 evidence that these Nb-rich primary carbides tend to crack during J-R testing, as seen in Figure 89. Yonezawa (2013) concludes that cracking of primary carbides during crack growth testing of Alloy 690 is a factor that accelerates IGSCC. When the specimen is loaded in a J-R test and the carbide cracking begins to occur, sharp cracks and voids form and they can absorb hydrogen from the surrounding material. During the test more hydrogen diffuses into the metal when the specimen is loaded in hydrogenated low temperature water and, eventually the primary carbides and the surrounding deformed matrix with high dislocation density may reach high levels of hydrogen concentration. This mechanism may increase the LTCP susceptibility of Alloy 182, where large primary carbides are commonly observed.

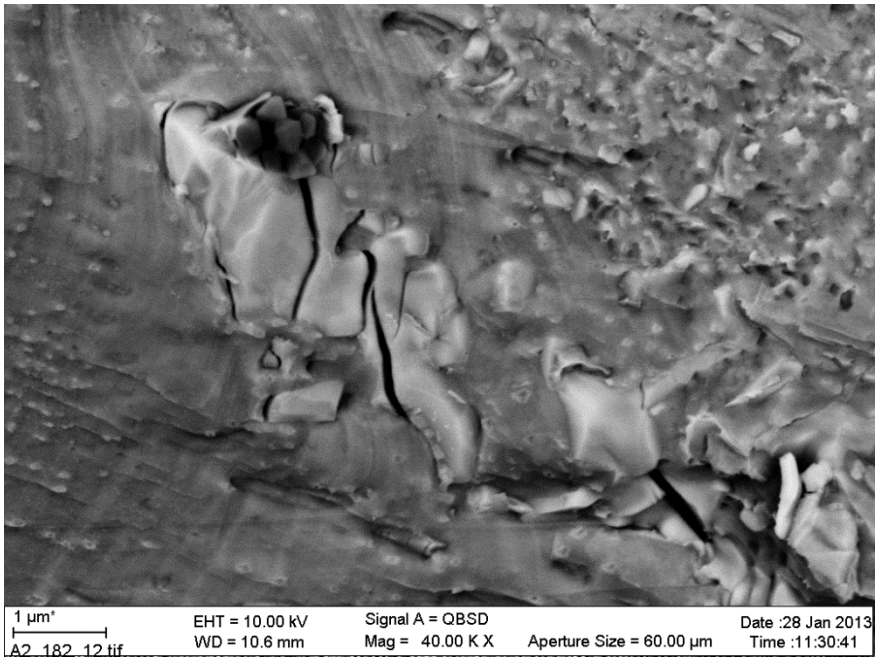

Figure 89. SEM (BSE) image showing cracking of the Nb-rich MC-type carbides on the fracture surface of Alloy 182.

6.5 Hydrogen measurements

A general observation from the both bulk hydrogen content measurements and TDS results is that the welding method and the hydrogen content of the as-welded materials are interrelated. Shielded Metal Arc Welded (SMAW) materials Alloys 182 and 152 exhibit larger amounts of hydrogen in as-welded condition than Gas Tungsten Arc Welded (GTAW) Alloy 52. However, one must bear in mind that assumptions on hydrogen content of the material that are made based on TDS measurements are not absolutely reliable because of relatively small amount of inhomogeneous material studied in a TDS measurement. That was observed in the case of Alloy 182 that was tested twice with heating rate 6 K/min. The first result, shown in Figure 32, shows a maximum desorption rate that is slightly more than half of what was obtained in another measurement for the same material, presented in Figure 35. However, the maximum peak temperature is located at about 400 °C in both measurements. It was also noticed that the alloys containing more hydrogen also contained Nb and thus large Nb-rich MC-type carbides that are strong traps for hydrogen.

The bulk hydrogen content measurements presented in Table 7 show that the hydrogen contents of Alloys 182 and 152 actually decrease as a result of 30 days pre-exposure in 300 °C hydrogenated (30 cm^3 H_2/kg H_2O) water. This gives support to the assumption that trapped hydrogen has an effect on LTCP and clarifies the relationship between the hydrogen content of the material and the fracture resistance, as it was shown earlier that high temperature pre-exposure increased the fracture resistance of Alloys 182 and 152. The results obtained from the thermal desorption measurements show that the trapped hydrogen is partly outgassed from the trapping sites during the pre-exposure. The maximum hydrogen desorption rates for as-welded Alloys 182 and 152 are located slightly below and above 400 °C, respectively. The desorption curve for as-welded Alloy 52 is significantly lower than those of as-welded Alloys 182 and 152, but the maximum desorption rate temperature for as-welded Alloy 52 seems to be similar to that of as-welded Alloy 152. The total amount of hydrogen is decreased to ~1/3 of the original value as a result of pre-exposure (5 cm^3 H_2/kg H_2O) for Alloys 182 and 152.

The analysis of thermal desorption measurements is a mean to characterize the microstructural trapping sites of the material. All the studied alloys contain trapped hydrogen, which releases at the temperatures of about 400 °C and 500 °C. Pre-exposed alloys manifest a complicated shape of the thermal desorption peak or multiple peaks which are caused by the presence of multiple types of trapping sites. Possible trapping positions of hydrogen are grain boundaries, precipitates, dislocations, voids, inclusions, and interstitial positions. The activation energy for hydrogen desorption obtained in this study for as-welded Alloy 182 DMW was 40.0 ± 3.7 kJ/mol. The calculated value was somewhat lower than the value obtained by Young et al. for as-welded Alloy 182 all-weld metal (67.7 kJ/mol, in Young et al., 1997) and similar to that obtained by Ai et al. for solution heat treated and aged Monel K-500 (41.2 ± 1.7 kJ/mol, in Ai et al., 2013), although the trapping in the case of Monel K-500 is due to γ' precipitates. Alloy 52 exhibits two different trapping sites that are lower energy traps compared to that of Alloy 182.

Some unusual small peaks were observed on occasion in TDS curves. These peaks that occurred in some measurements but not in others for a certain material are believed to be caused by impurity inclusions or weld defects. This kind of peak is present for example in the TDS curve of Alloy 152 measured after pre-exposure with 5 cm^3 H_2/kg H_2O at about 500 °C, but not in the curve measured after pre-exposure with 30 cm^3 H_2/kg H_2O. In addition, it was observed for both Alloys 182 and 52 that there was a small peak at about 500 °C, when measured after pre-exposure with 30 cm^3 H_2/kg H_2O, but that peak does not occur in post-weld heat treated samples. This peak was not observed to occur in AW samples either. Thus, it is assumed that these peaks are also caused by hydrogen trapped occasionally in some weld defects or inclusions.

6.6 Role of grain boundary carbides in LTCP

LTCP behaviour of the studied Alloy 182, 82, 152 and 52 weld metals was found to be somewhat different for each material. Alloys 182, 152 and 52 were most extensively studied. The studied alloys can be divided based on their chemical composition to higher and lower Cr alloys, and on the other hand to alloys containing Nb and to alloys that do not contain Nb. The general impression, that is attained when all the results are evaluated as a whole is, that the key effect of the chemical composition on LTCP behaviour is the grain/dendrite boundary carbide structure. In addition to chemical composition, thermal history has a significant effect on the carbide precipitation and thus on LTCP behaviour of nickel-based weld metals.

As was shown by hydrogen content measurements (bulk and TDS), Alloys 182 and 152 containing Nb contained a higher amount of hydrogen than Alloy 52 in which Nb is not alloyed. This is also partly due to the different welding technique. Activation energies for hydrogen desorption from the trapping sites were observed to be different for Alloy 182 and 52 welds. In Alloy 182 there was one dominating trapping site which was a higher energy trap than the two different traps that were observed in Alloy 52. The study by Yonezawa et al. (1993) shows that incoherent carbides are stronger traps than the coherent ones and for Alloy X-750 stress corrosion cracking occurred only in materials with incoherent carbides. Hence, in Alloy 182 the hydrogen trapping is probably governed by intergranular Nb-rich MC-type carbides, whereas trapping in Alloy 52 is caused by two different types of carbides that can be Cr-rich $M_{23}C_6$ and very fine Ti-rich MC-type carbides, of which the fine MC-type carbides will account for the higher energy trap. The trapped hydrogen then induces decohesion at the grain boundaries during J-R testing. The grain boundary carbides and the dislocation networks around them can also act as locations of hydrogen accumulation when the specimen is loaded.

6.7 Subjects for further studies

A variety of techniques was utilized and a significant amount of data was generated in this study. The results obtained within this study extend the understanding of the phenomena occurring in nickel-based alloy weld metals in hydrogenated low temperature water. However, there are some areas where further studies are desirable.

Transmission electron microscopy was applied in examining the grain boundary carbides but the study was limited. Since the literature shows that there is a relation between the grain boundary carbides and SCC susceptibility, the TEM examinations could be followed by a study of determining the orientation of the carbides relative to the matrix.

Welding parameters and thermal history seem to have an effect on the LTCP behaviour of Alloy 52, since the results for all-weld metal specimens and DMW

specimens were somewhat different. The effect of thermal ageing on the fracture resistance behaviour of Alloy 52 would be of great interest considering the long-term operation and structural integrity of nuclear power plants, where Alloy 52 is used.

This study concentrated in fracture mechanical testing and microscopy. The results and knowledge obtained from the results of this study could be further utilized by creating a FEM model that could illustrate and predict the fracture behaviour of different austenitic materials in hydrogenated water.

It was observed during this study that the fracture surfaces of the weld metal specimens exhibit a macroscopically uneven appearance. This results in slightly false assumptions in J-integral calculations where the final crack length is measured from the projection and not from the actual cracking path along the surface. The actual cracking paths could be measured using 3D topography and the more accurate J-R curves could then be determined by applying FEM and giving input of Δa versus force-displacement.

7 Conclusions

1. Hydrogen decreases the fracture resistance of Alloys 182, 82, 152 and 52 significantly in low temperature water with high hydrogen contents (100 cm^3 H_2/kg H_2O). Alloy 182 is the most susceptible material to LTCP, and it exhibits a significant reduction of fracture resistance already with hydrogen content of 30 cm^3 H_2/kg H_2O. The degrading effect of hydrogen on LTCP resistance of nickel-based Alloy 182, 82, 152 and 52 weld metals in low temperature water has been clearly demonstrated.

2. Specimens of Alloy 52 DMW behaved in varying manner when tested with high hydrogen content, in both AW and PWHT conditions. Some specimens of Alloy 52 were observed to exhibit rather low J_Q values, similar to those of Alloy 182, when tested with highest hydrogen content. The inhomogeneous microstructure and varying grain size of Alloy 52 provides an explanation to this kind of behaviour because the pre-crack tip location regarding microstructure varies.

3. High temperature pre-exposure (300 °C) was shown to have a rather slight but a systematic increasing effect on fracture resistance of Alloy 182 and 152 weld metals tested in low temperature water regardless of the hydrogen content of the water.

4. Hydrogen trapping has a degrading effect on fracture resistance of Alloy 182 and 152 weld metals. Bulk hydrogen content measurements show that pre-exposure in high temperature water (30 days at 300 °C) decreases the amount of trapped hydrogen and slightly increases the fracture resistance when compared to the results obtained for as-welded samples.

5. Pre-exposed alloys manifest a diverging shape of the TDS curves with single peak or multiple peaks, which is caused by the presence of multiple types of trapping sites. Different activation energies for hydrogen de-

sorption were determined for DMW Alloys 182 and 52 which indicates that the hydrogen trapping is caused by different carbides of the alloys.

6. Reduction of fracture resistance in J-R test results is typically observed on the fracture surfaces of the studied materials as a change in the type of fracture. Higher J_Q values correspond to fracture surfaces exhibiting mainly ductile dimple cracking, whereas specimens with lower J_Q values show large areas of IG/ID cracking.

7. Alloy 52 usually exhibits significant plastic deformation when the small tetrahedron-shaped carbides are detached from the fracture surface, whereas the small carbides in Alloy 182 detach from the ID fracture surface without notable plastic deformation. This indicates on the differences in the cohesion strength between the carbides and matrix of Alloy 182 and 52 weld metals.

8. The IG/ID fracture surfaces of Alloy 52 manifest a complex surface structure. Crack propagation deviates between two parallel planes of a Cr-depleted zone near the grain boundary. The width of the grain boundary zone fits well with the Cr-rich $M_{23}C_6$ carbide size.

9. Alloy 182 DMW tested with moderate and high hydrogen contents exhibited a transgranular (or transdendritic) cracking mechanism that is believed to be hydrogen-induced based on its macroscopically planar appearance and somewhat low J_Q values. Cracking occurred in the dendrite growth direction <100>.

10. The different LTCP behaviour of Alloy 182 and 52 weld metals is believed to be caused mainly by different types of carbides affecting the hydrogen-induced fracture. The carbides may have an effect on hydrogen distribution at the grain/dendrite boundaries and the availability of hydrogen close to the crack tip.

11. Post-weld heat treatment slightly increases the J_{1mm} values and tearing modulus of DMW Alloy 182 tested in hydrogenated low temperature water but does not have a clear effect on J_Q.

8 References

Ahonen, M., Ehrnstén, U., Saukkonen, T., Todoshchenko, O. & Hänninen, H. 2013. Low Temperature Crack Propagation (LTCP) Susceptibility of Nickel-Based Alloy 182, 152 and 52 Weld Metals in PWR Primary Water. In: Proceedings of the 16th International Conference on Environmental Degradation of Materials in Nuclear Power Systems - Water Reactors. Asheville, North Carolina, August 11-15, 2013. USA: Omnipress (CD-ROM).

Ahonen, M., Ehrnstén, U. & Hänninen, H. 2014. The Effect of Microstructure on Low Temperature Crack Propagation (LTCP) Susceptibility of Nickel-Based Alloy 182, 152 and 52 Weld Metals in PWR Primary Water. In: Proceedings of the 8th Fontevraud Conference, Avignon, France, September 15-18, 2013. France: SFEN (CD-ROM).

Ai, J.-H., Ha, H. M., Gangloff, R. P. & Scully, J. R. 2013. Hydrogen Diffusion and Trapping in a Precipitation-Hardened Nickel-Copper-Aluminum Alloy Monel K-500 (UNS N05500). Acta Materialia, 61 (2013), pp. 3186-3199.

Anderson, T. L. 2005. Fracture Mechanics Fundamentals and Applications, 3rd Edition. USA: CRS Press, 610 p. ISBN 1-4200-5821-5 (eBook - PDF).

Andresen, P. 1987. Effect of Dissolved Oxygen, Solution Conductivity and Stress Intensity on the Interdendritic Stress Corrosion Cracking of Alloy 182 Weld Metal. In: Proceedings of Corrosion/87. San Francisco, California, March 9-13, 1987. Paper No. 85. 12 p.

Andresen, P. L., Morra, M. M., Hickling, J., Ahluwalia, A. & Wilson, J. 2007. PWSCC of Alloys 690, 52 and 152. In: Proceedings of the 13th International Symposium on Environmental Degradation of Materials in Nuclear Power Systems - Water Reactors, Whistler, Canada, April 19-23, 2007. Canada: CNS-SNC (CD-ROM).

Angelo, J. E., Moody N. R. & Baskes, M. I. 1995. Trapping of Hydrogen to Lattice Defects in Nickel. Modelling and Simulation in Materials Science and Engineering, 3 (1995), pp. 289-307.

Bamford, W. H., Foster, J. P. & Pathania, R. S. 1999. An Investigation of Alloy 182 Stress Corrosion Cracking in Simulated PWR Environment. In: Bruemmer, S., Ford, P. & Was, G. (Eds.). Proceedings of the 9th International Symposium on Environmental Degradation of Materials in Nuclear Power Systems – Water Reactors. Newport Beach, California, August 1-5, 1999. USA: TMS, pp. 279-296. ISBN 0-87339-475-5.

Baty, D. L., Hayner, G. O., Clevinger, G. S., & Garner, G. L. 1984. Metallurgical Factors Affecting the Failure of Alloy X-750 Holddown Springs. In: Roberts, J. T. A. & Berry, W. (Eds.). Proceedings of the International Symposium on Environmental Degradation of Materials in Nuclear Power Systems – Water Reactors. Myrtle Beach, South Carolina, August 22-24, 1983. USA: NACE, pp. 151-178. ISBN 0-915567-00-8.

Berge, P. 1988. Can PWR U-Tube Steam Generators Work Safely? In: Theus, G. J. & Weeks, J. R. (Eds.). Proceedings of 3rd International Conference on Environmental Degradation of Materials in Nuclear Power Systems – Water Reactors. Traverse City, Michigan, August 30-September 3, 1987. USA: The Metallurgical Society, Inc. pp. 49-54. ISBN 0-87339-030-X.

Birnbaum, H. K. & Sofronis, P. 1994. Hydrogen-Enhanced Localized Plasticity – a Mechanism for Hydrogen Related Fracture. Materials Science and Engineering, A176 (1994), pp. 191-202.

Bose, S. K. & Grabke, H. J. 1978. Diffusion Coefficient of C in Fe-Ni Austenite in the Temperature Range 950-1100 °C. Zeitschrift fur Metallkunde, 69 (1), pp. 8-15.

Brody, H. D. & Flemings, M. C. 1966. Solute Distribution in Dendritic Solidification. Transactions of AIME, 236 (5), pp. 615-624.

Brown, C. M. & Mills, W. J. 1999. Effect of Water on Mechanical Properties and Stress Corrosion Behavior of Alloy 600, Alloy 690, EN82H Welds, and EN52 Welds. Corrosion, 55 (2), pp. 173-186.

Brown, C. M. & Mills, W. J. 2002. Fracture Toughness of Alloy 690 and EN52 Welds in Air and Water. Metallurgical and Materials Transactions A, 33A (6), pp. 1725-1735.

Brown, C. M. & Mills, W. J. 2005. Load Path Effects on the Fracture Toughness of Alloy 82H and 52 Welds in Low Temperature Water. In: Allen, T.R. (Ed.) Proceedings of the 12th International Symposium on Environmental Degradation of Materials in Nuclear Power Systems – Water Reactors. Salt Lake City, Utah, August 14-18, 2005. USA: TMS (CD-ROM).

Brown, C. M. & Mills, W. J. 2007. Effect of Defect Acuity on the Fracture Behavior of Alloy 82H Welds in Low Temperature Water. In: Proceedings of the 13th International Symposium on Environmental Degradation of Materials in Nuclear Power Systems - Water Reactors, Whistler, Canada, April 19-23, 2007. Canada: CNS-SNC (CD-ROM).

Bruemmer, S. M., Vetrano, J. S. & Toloczko, M. B. 2007. Microstructure and SCC Crack Growth of Nickel-Base Alloy 182 Weld Metal in Simulated PWR Primary Water. In: Proceedings of the 13th International Symposium on Environmental Degradation of Materials in Nuclear Power Systems - Water Reactors, Whistler, Canada, April 19-23, 2007. Canada: CNS-SNC (CD-ROM).

Buisine, D., de Bouvier, O., Rupa, N., Thebault, Y., Barbe, V. & Pitner, P. 2010. French Steam Generator Tubes: An Overview of Degradations. In: Proceedings of the 7th Fontevraud Conference, Avignon, France, September 26-30, 2010. France: SFEN (CD-ROM).

Collins, M. G., Ramirez, A. & Lippold, J. C. 2004. An Investigation of Ductility-Dip Cracing in Ni-Based Weld Metals – Part 3. Welding Journal, 83 (2), pp. 39s-49s.

Copson, H. R. 1959. Effect of Composition on Stress Corrosion Cracking of Some Alloys Containing Nickel. In: Rhodin, T. N. (Ed.). Physical Metallurgy of Stress-Corrosion Fracture. New York: Interscience, pp. 247-272.

Coriou, H., Grall, L. & Vettier, S. 1960. Corrosion fissurante sous contrainte de l'Inconel dans l'eau à haute temperature. In: Third Saclay Metallurgy Colloquium. North Holland, p. 161.

Cronvall, O. 2011. Structural Integrity Study Concerning LTCP Phenomenon. VTT Research Report no. VTT-R-00055-11. 42 p.

Davis, J. R. (Ed.). 2000. ASM Speciality Handbook: Nickel, Cobalt, and Their Alloys. USA: ASM, 442 p. ISBN 0-87170-685-7.

Demma, A., McIlree, A. & Herrera, M. 2005. Low Temperature Crack Propagation Evaluation in Pressurized Water Reactor Service. In: Allen, T.R. (Ed.) Proceedings of the 12th International Symposium on Environmental Degradation of Materials in Nuclear Power Systems – Water Reactors. Salt Lake City, Utah, August 14-18, 2005. USA: TMS (CD-ROM).

DuPont, J. N., Robino, C. V., Mader, A. R., Notis, M. R. & Michael, J. R. 1988. Solidification of Nb-Bearing Superalloys: Part I. Reaction Sequences. Metallurgical and Material Transactions A, 29A, pp. 2785-2796.

DuPont, J. N., Lippold J. C. & Kiser, S. D. 2009. Welding Metallurgy and Weldability of Nickel-Base Alloys. USA: John Wiley and Sons, Inc. Hobocken, N.J. ISBN 987-0-470-08714-5. 440 p.

EPRI Technical Update Report: Materials Reliability Program, Resistance to Primary Water Stress Corrosion Cracking of Alloys 690, 52, and 152 in Pressurized Water Reactors (MRP-111). 2004. EPRI Project managers Hickling, J. & King, C. Palo Alto, CA, USA.

Fish, J. S., Lewis, N., Yang, W. J. S., Perry, D. J. & Thompson, C. D. 1997. AEM Investigations on Primary Water SCC in Nickel Alloys. In: McIlree, A. R. & Bruemmer, S. M. (Eds.) Proceedings of the 8th International Symposium on Environmental Degradation of Materials in Nuclear Power Systems – Water Reactors. Amelia Island, Florida, August 10-14, 1997. USA: ANS, pp. 266-273. ISBN 0-894488-626-8.

Grove, C. A. & Petzold, L. D. 1985. Mechanisms on Stress-Corrosion Cracking of Alloy X-750 in High-Purity Water. J. Materials for Energy Systems, 7 (2), pp. 147-162.

Guerre, C., Duhamel, C., Sennour, M., Crépin, J. & Le Calvar, M. 2011. SCC Crack Growth Rate of Alloy 82 in PWR Primary Water Conditions – Effect of a Thermal Treatment. In: Busby, J. T., Ilevbare, G. & Andresen, P. L. (Eds.). Proceedings of the 15th International Symposium on Environmental Degradation of Materials in Nuclear Power Systems – Water Reactors. Colorado Springs, Colorado, August 7-11, 2011. USA: TMS (CD-ROM).

Herms, E., Raquet, O., De Curières, I. & Joly, P. 2009. LTCP of Alloy 182/152 Tested in PWR Primary Water. In: Proceedings of the 14th International Symposium on Environmental Degradation of Materials in Nuclear Power Systems - Water Reactors. Virginia Beach, Virginia, August 23-27, 2009. USA: ANS (CD-ROM).

Heubner, U., Kohler, M. & Prinz, B. 1988. Determination and the Solidification Behavior of Some Selected Superalloys. In: Retchman, S., Duhl, D. N. Maurer, G., Antolovich, S. & Lund, C. (Eds.). Superalloys 1988, Proceedings of the Sixth International Symposium on Superalloys. Champion, Pennsylvania, September 18-22, 1988. USA: ANS, pp. 437-447. ISBN 0-87339-076-8.

Hilkes, J., Neesen, F. & Caballero, S. 2004. Electrodes for Welding 9% Nickel Steel. Welding Journal, 83 (1), pp. 30-37.

Honeycombe, R. W. K. & Bhadesia, H. K. D. H. 1995. Steels: Microstructure and Properties, 2nd edition. Great Britain: Edward Arnold, a member of the Hodder Headline PLC, 324 p. ISBN 0-304-58946-9.

Hosoi, K., Hattori, S., Urayama, Y., Masaoka, I & Sasaki, R. 1984. Relation between Susceptibility to Stress Corrosion Cracking in High Temperature Water and Microstructure of Inconel X-750. In: Roberts, J. T. A. & Berry, W. (Eds.). Proceedings of the International Symposium on Environmental Degradation of Materials in Nuclear Power Systems – Water Reactors. Myrtle Beach, South Carolina, August 22-24, 1983. USA: NACE, pp. 334-344. ISBN 0-915567-00-8.

Hosoya, K., Ballinger, R., Prybylowski, J. & Hwang, I. S. 1988. Microstructural Role in Environmentally Assisted Cracking of Ni-Base Alloys. Corrosion, 44 (11), pp. 838-852.

Hänninen, H., Brederholm, A., Saukkonen, T., Gripenberg, H., Toivonen, A., Ehrnsten, U. & Aaltonen, P. 2007. Hot Cracking and Environment-assisted Cracking Susceptibility of Dissimilar Metal Welds. VTT Research Notes 2399. Espoo: VTT Technical Research Centre of Finland. 181 p.

Hänninen, H., Brederholm, A., Sarikka, T., Mouginot, R., Holmström, P., Saukkonen, T., Toivonen, A., Karjalainen-Roikonen, P., Nevasmaa, P., Keinänen, H., Leskelä, E., Ahonen, M., Ehrnstén, U. & Aaltonen, P. 2014. Structural Integrity of Ni-base Alloy Welds. VTT Technology 175. Espoo: VTT Technical Research Centre of Finland. 257 p. ISBN 978-951-38-8259-4.

Jeng, S. L., Lee, H. T., Rehbach, W. P., Kuo, T. Y., Weirich, T. E. & Mayer, J. P. 2005. Effects of Nb on the Microstructure and Corrosive Property in the Alloy 690–SUS 304L Weldments. Materials Science and Engineering A, 397 (1-2), pp. 229-238.

Joo, H. & Takeuchi, H. 1994. Cast Structure of Inconel 713C Alloy. Tokai Daigaku Kiyo, 34 (1), pp. 203-209.

Kaneda, J., Horiuchi, T., Kuniya, J., Nagase, H. & Koshiishi, M. 2007. Investigation of Precipitation and Segregation on Grain Boundaries in Ni-Based Alloys and Welds. In: Proceedings of the 13th International Symposium on Environmental Degradation of Materials in Nuclear Power Systems - Water Reactors, Whistler, Canada, April 19-23, 2007. Canada: CNS-SNC (CD-ROM).

Kekkonen, T., Aaltonen, P. & Hänninen, H. 1985. Metallurgical Effects on the Corrosion Resistance of a Low Temperature Sensitized Welded AISI Type 304 Stainless Steel. Corrosion Science, 25 (8/9), pp. 821-836.

Kiser, S. 1990. Nickel-Alloy Consumable Selection for Severe Service Conditions. Welding Journal, 69(1), pp. 30-35.

Kou, S. 2003. Welding Metallurgy, 2nd Edition. 2003. USA: John Wiley & Sons, Inc., 461 p. ISBN 0-471-43491-4.

Lee, H. G. & Lee, J.-Y. 1984. Hydrogen Trapping by TiC Particles in Iron. Acta Metallurgica et Materialia, 32 (1), pp. 131-136.

Lee, H. T., Jeng, S. L., Yen, C. H. & Kuo, T. Y. 2004. Dissimilar Welding of Nickel-Based Alloy 690 to SUS 304L with Ti Addition. Journal of Nuclear Materials, 335 (1), pp. 59-69.

Lippold, J., Clark, W. A. T. & Tumuluru, M. 1992. An Investigation of Weld Metal Interfaces. The Metal Science of Joining. The Metals, Minerals and Materials Society, Warrendale, PA, pp. 141-146.

Lippold, J., Ramirez, A. & Sowards, J. 2004. New Insight into the Mechanism of Ductility Dip Cracking in Nickel-Based Weld Metals. IIW Doc. No. IX-2123-04. 15 p.

Lippold, J. C. & Kotecki, D. J. 2005. Welding Metallurgy and Weldability of Stainless Steels. USA: John Wiley and Sons, Inc., Hobocken, N.J., ISBN 0-47147379-0.

Lundin, C. D. 1982. Dissimilar Metal Welds – Transition Joints Literature Review. Welding Journal, 61 (2), pp. 58-63.

McCracken, S. 2014. Weld Mockups for Characterization and CGR Testing. Presented in: EPRI Alloy 690/52/152 Primary Water Stress Corrosion Cracking Research Collaboration Meeting, Tampa, California. December 2-4, 2014.

McIllree, A., Demma, A., Peng, J. & King, P. 2006. Effects of Hydrogen and Temperature on the Fracture Resistance of Weld Metals 182 and 152 in Simulated PWR Shutdown Environment. Proceedings of the 6th Fontevraud Conference, 18-22 September 2006, Fontevraud Royal Abby, France (CD-ROM).

Mills, W. J. 1997. Fracture toughness of type 304 and 316 stainless steels and their welds. International Materials Reviews, 42 (2), pp. 45-82.

Mills, W. J., Lebo, M. R. & Kearns, J. J. 1999. Hydrogen Embrittlement, Grain Boundary Segregation, and Stress Corrosion Cracking of Alloy X-750 in Low- and High-Temperature Water. Metallurgical and Materials Transactions A, 30 A (6), pp. 1579-1596.

Mills, W. J. & Brown, C. M. 1999. Fracture Behavior of Nickel-Based Alloys in Water. In: Bruemmer, S., Ford, P. & Was, G. (Eds.). Proceedings of the 9th International Symposium on Environmental Degradation of Materials in Nuclear Power Systems – Water Reactors. Newport Beach, California, August 1-5, 1999. USA: TMS, pp. 279-296. ISBN 0-87339-475-5.

Mills, W. J. & Brown, C. M. 2001. Fracture Toughness of Alloy 600 and EN82H Weld in Air and Water. Metallurgical and Materials Transactions A, 32A (5), pp. 1161-1174.

Mills, W. J., Brown, C. M. & Burke, M. G. 2001. Effect of Microstructure on Low Temperature Cracking Behavior of EN82H Welds. In: Proceedings of the 10th International Symposium on Environmental Degradation of Materials in Nuclear Power Systems - Water Reactors. Lake Tahoe, Nevada, August 5-9, 2001. USA: NACE International (CD-ROM).

Moody, N. R., Robinson, S. L. & Perra, M. W. 1993. Internal Hydrogen Effects of Thresholds for Crack Growth in the Iron-Based Superalloy IN930. Engineering Fracture Mechanics, 39 (6), pp. 941-954.

Morra, M., Othon, M., McCracken, S., Sutton, B. & Ahluwalia, A. 2014. Analysis of Narrow Groove 52M Welds SA508 to 316L amd SA508 to Alloy 690. Presented in: EPRI Alloy 690/52/152 Primary Water Stress Corrosion Cracking Research Collaboration Meeting, Tampa, California. December 2-4, 2014.

Mouginot, R. & Hänninen, H. 2013. Microstructures of nickel-base alloy dissimilar metal welds. Aalto University publication series Science + Technology. Helsinki: Unigrafia Oy. 178 p. ISBN 978-952-60-5065-2.

Nelson, T. W., Lippold, J. C. & Mills, M. J. 1999. Nature and Evolution of the Fusion Boundary in Ferritic-Austenitic Dissimilar Metal Weld Metals, Part 1 – Nucleation and Growth. Welding Journal, 78, pp. 329s-337s.

Nibur, K. A., Bahr, D. F. & Somerday, B. P. 2006. Hydrogen Effects on Dislocation Activity in Austenitic Stainless Steel. Acta Materialia, 54, pp. 2677-2684.

Nibur, K. A., Somerday, B. P., Balch, D. K. & San Marchi, C. 2009. The Role of Localized Deformation in Hydrogen-Assisted Crack Propagation in 21Cr–6Ni–9Mn Stainless Steel. Acta Materialia, 57, pp. 3795-3809.

Oriani, R. A. 1993. The Physical and Metallurgical Aspects of Hydrogen in Metals. In: Passell, T. O. & McKubrel, M. C. H., ICCF4, Fourth International Conference on Cold Fusion. Lahaina, Maui, December 1993. USA: ANS.

Pasupathi, V., Perrin, J., Farmelo, D., Smith, G. & Weiss, S. 1980. Investigation of Inconel safe-end failure in Duane Arnold. Trans. ANS 34, pp. 232-233.

Peckner, D. & Bernstein, I. M. 1977. Handbook of Stainless Steels. USA: McGraw-Hill. 800 p. ISBN 0-07-049147-X.

Peng, Q. J., Hou, J., Yonezawa, T., Shoji, T., Zhang, Z.M., Huang, F., Han, E.-H. & Ke, W. 2012. Environmentally Assisted Crack Growth in One-Dimensionally Cold Worked Alloy 690TT in Primary Water. Corrosion Science, 57 (2012), pp. 81-88.

Peng, Q., Yamauchi, H. & Shoji, T. 2003. Dendrite Boundary Microchemistry in Alloy 182 Weld Metal. In: Proceedings of the 11th International Symposium on Environmental Degradation of Materials in Nuclear Power Systems - Water Reactors, Stevenson, Washington, August 10-14, 2003. USA: ANS (CD-ROM).

Pressoyre, G. M. 1983. Hydrogen Traps, Repellers, and Obstacles in Steel; Consequences on Hydrogen Diffusion, Solubility, and Embrittlement. Metallurgical Transactions A, 14A (10), pp. 2189-2193.

Ramirez, A. J. & Lippold, J. C. 2004a. High Temperature Behavior of Ni-Base Weld Metal: Part I – Ductility and Microstructural Characterization. Materials Science and Engineering A, 380, pp. 259-271.

Ramirez, A. J. & Lippold, J. C. 2004b. High Temperature Behavior of Ni-Base Weld Metal: Part II – Insight into the Mechanism for Ductility-Dip Cracking. Materials Science and Engineering A, 380, pp. 245-258.

Rao, G., Moffatt, G. & McIlree, A. 2002. Metallurgical Investigation of Cracking in the Reactor Vessel Alpha Loop Hot Leg Nozzle to Pipe Weld and the V. C. Summer Station. In: Proceedings of Fontevraud 5, Contribution of Material Investigation to the Resolution of Problems Encountered in Pressurized Water Reactors. Fontevraud, France, September 23-27, 2002. France: SFEN, pp. 29 - 41.

Richards, N. & Chaturvedi, M. 2000. Effect of Minor Elements on Weldability of Ni-Base Superalloys. International Metals Reviews, 45 (3), pp. 109-129.

Sakima, K., Suzuki, H. & Fujiwara, H. Research and Evaluation of Low Temperature Crack Propagation of Ni Base Alloys in Actual Plants. In: Busby, J. T., Ilevbare, G. & Andresen, P. L. (Eds.). Proceedings of the 15th International Symposium on Environmental Degradation of Materials in Nuclear Power Systems – Water Reactors. Colorado Springs, Colorado, August 7-11, 2011. USA: TMS (CD-ROM).

Shah, V. & MacDonald, P. (Eds.). 1993. Aging and Life Extension of Major Light Water Reactor Components. Netherlands: Elsevier, 941 p. ISBN 0-444-89448-9.

Shoji, T., Ito, Y., Lu, Z. & Yonezawa, T. 2007. Mechanistic Understanding of Low Temperature Crack Propagation for Alloy 690 in Hydrogenated Water. In: Proceedings of the 13th International Symposium on Environmental Degradation of Materials in Nuclear Power Systems - Water Reactors, Whistler, Canada, April 19-23, 2007. Canada: CNS-SNC (CD-ROM).

Skeldon, P. & Hurst, P. 1988. Environmentally Assisted Cracking of Inconel X-750. Proceedings of 3rd International Conference on Environmental Degradation of Materials in Nuclear Power Systems – Water Reactors. Traverse City, Michigan, August 30-September 3, 1987. USA: The Metallurgical Society, Inc. pp. 703-710. ISBN 0-87339-030-X.

Sirois, E. & Birnbaum, H. K. 1992. Effects of Hydrogen and Carbon on Thermally Activated Deformation in Nickel. Acta Metallurgica et Materialia, 40 (6), pp. 1377-1385.

Symons, D. M. & Thompson, A. W. 1997. The Effect of Hydrogen on the Fracture Toughness of Alloy X-750. Metallurgical and Materials Transactions A, 28A, pp. 817-823.

Symons, D. M. 1999. The effect of hydrogen on the fracture toughness of alloy X-750 at elevated temperatures. Journal of Nuclear Materials, 265, pp. 225-231.

Symons, D. M. 2001. A comparison of internal hydrogen embrittlement and hydrogen environment embrittlement of X-750. Engineering Fracture Mechanics, 68, pp. 751-771.

Thomas, L. E., Olzsta, M. J., Johnson, B. R. & Bruemmer, S. M. 2009. Microstructural Characterization of Primary Stress-Corrosion Cracks in Alloy 182 Welds from PWR Components and Laboratory Tests. In: Proceedings of the 14th International Symposium on Environmental Degradation of Materials in Nuclear Power Systems - Water Reactors. Virginia Beach, Virginia, August 23-27, 2009. USA: ANS (CD-ROM).

Troiano, A. R. 1960. The Role of Hydrogen and Other Interstitials in the Mechanical Behavior of Materials. Trans ASM, 52, pp. 54-80.

Wallin, K. 2011. Fracture Toughness of Engineering Materials: Estimation and Application. UK: EMAS Publishing, 543 p. ISBN 0-9552994-6-2.

Webb, G. L. & Burke M. G. 1995. Stress Corrosion Cracking Behavior of Alloy 600 in High Temperature Water. In: Airey, G. et al. (Ed.). Proceedings of the 7th International Symposium on Environmental Degradation of Materials in Nuclear Power Systems – Water Reactors. Breckenridge, Colorado, August 7-10, 1995. USA: NACE International, pp. 41-56. ISBN 1-877914-95-9.

Wei, F. G. & Tsuzaki, K. 2006. Quantitative Analysis on Hydrogen Trapping of TiC Particles in Steel. Metallurgical and Materials Transactions A, 37A, pp. 331-353.

Welty, C. S. & Blomgren, J. C. 1990. Steam Generator issues. In: Cubicciotti, D. (Ed.). Proceedings of 4th International Conference on Environmental Degradation of Materials in Nuclear Power Systems – Water Reactors. Jekyll Island, Georgia, August 6-10, 1989. USA: NACE. pp. 1.27-1.36. ISBN 1-877914-04-5.

Yonezawa, T., Onimura, K, Sakamoto, N., Sasaguri, N., Nakata, H. & Susukida, H. 1984. Effect of Heat Treatment on Stress Corrosion Cracking Resistance of High Nickel Alloys in High Temperature Water. Proceedings of the International Symposium on Environmental Degradation of Materials in Nuclear Power Systems – Water Reactors. Myrtle Beach, South Carolina, August 22-24, 1983. USA: NACE, pp. 151-178. ISBN 0-915567-00-8.

Yonezawa, T. & Onimura, K. 1989. Effect of Chemical Compositions and Microstructure on the Stress Corrosion Cracking Resistance of Nickel Base Alloys in High Temperature Water. Proceedings of the EVALMAT, Kobe, Japan, 89-1, pp. 235-242.

Yonezawa, T., Yamaguchi, Y. & Iijima, Y. 1993. Electron Micro Autoradiographic Observations of Tritium Distribution on Alloy X750. In: Gold, R. E. & Simonen, E. P. (Eds.). Proceedings of 6th International Conference on Environmental Degradation of Materials in Nuclear Power Systems – Water Reactors. San Diego, California, August 1-5. USA: TMS. ISBN 0-87339-258-2.

Yonezawa, T. 2008. The Possibility of Metallurgical Effects on LTCP of Alloy 690 and its Weld Metal in Hydrogenated Water. Presented in: EPRI MRP Expert Panel Meeting on Low Temperature Crack Propagation, Los Angeles, California. November 14, 2008.

Yonezawa, T. 2012. Nickel Alloys: Properties and Characteristics. In: Konings, R. J. M. (Ed.). Comprehensive Nuclear Materials. Germany: Elsevier Science, 600 p. ISBN 9780080560335.

Yonezawa, T. 2013. The Effects of Fabrication Process and Cold Working on PWSCCGR of TT Alloy 690 in Simulated PWR Primary Water. Presented in: EPRI Alloy 690/52/152 Primary Water Stress Corrosion Cracking Research Collaboration Meeting, Tampa, Florida. December 3-6, 2013.

Yonezawa, T. 2014. Stress Corrosion Cracking Growth Rate of TT Alloy 690 and Its Weld Joint in Simulated PWR Primary Water. Presented in: EPRI Alloy 690/52/152 Primary Water Stress Corrosion Cracking Research Collaboration Meeting, Tampa, Florida. December 2-5, 2014.

Yonezawa, T., Watanabe, M. & Hashimoto, A. 2015. The Effects of Metallurgical Factors on PWSCC Crack Growth Rates in TT Alloy 690 in Simulated PWR Primary Water. Metallurgical and Materials Transactions A, 46A, pp. 2768-2780.

Young, B., McIlree, A. & King, P. 2005. Reduction of Toughness for Weld Metal in a PWR Primary Water Environment with Varying Dissolved Hydrogen, Lithium and Boric Acid Concentrations. In: Allen, T.R. (Ed.) Proceedings of the 12th International Symposium on Environmental Degradation of Materials in Nuclear Power Systems – Water Reactors. Salt Lake City, Utah, August 14-18, 2005. USA: TMS (CD-ROM).

Young, G. A. & Scully, J. R. 1997. Evidence that Carbide Precipitation Produces Hydrogen Traps in Ni-17Cr-8Fe Alloys. Scripta Materialia, 36 (6), pp. 713-719.

Young, G. A., Lewis, N. & Hanson, M. 2001. Microstructural and Microchemical Characterization of Dual Step Aged Alloy X-750 and it Relationship to Environmentally Assisted Cracking. In: Proceedings of the 10th International Symposium on Environmental Degradation of Materials in Nuclear Power Systems - Water Reactors. Lake Tahoe, Nevada, August 5-9, 2001. USA: NACE International (CD-ROM).

Young, G. A., Battige, C., Lewis, N., Penik, M., Kikel, J., Silvia, A. & McDonald, C. 2003. Factors Affecting the Hydrogen Embrittlement Resistance of Ni-Cr-Mn-Nb Welds. Proc. of 6th International Trends in Welding Research Conference, 15-19 April 2002, Pine Mountain, GA, ASM international, pp. 666-671.

Young, G. A, Capobianco, R. A., Etien III, R. A., Mullen, J. V., Leveillee, S & Sander, P. C. 2007. Development of a Highly Weldable and Corrosion Resistant Nickel-Chromium Filler Metal. In: Proceedings of the 13th International Symposium on Environmental Degradation of Materials in Nuclear Power Systems - Water Reactors, Whistler, Canada, April 19-23, 2007. Canada: CNS-SNC (CD-ROM).

Young, G. A., Richey, E. & Morton, D. S. 2012. Hydrogen Embrittlement of Nickel-Based Alloys in Nuclear Power Systems. In: Gaseous Hydrogen Embrittlement of Materials in Energy Technologies: Mechanisms, Modelling and Future Developments. In: Gangloff, R. P. & Somerday, B. P. (Eds.), pp. 149-176. USA: Woodhead Publishing, 520 p. ISBN 978-0-85709-536-7.

9 ANNEX

9.1 J-R test results for as-welded (AW) specimens

9.1.1 Air tests

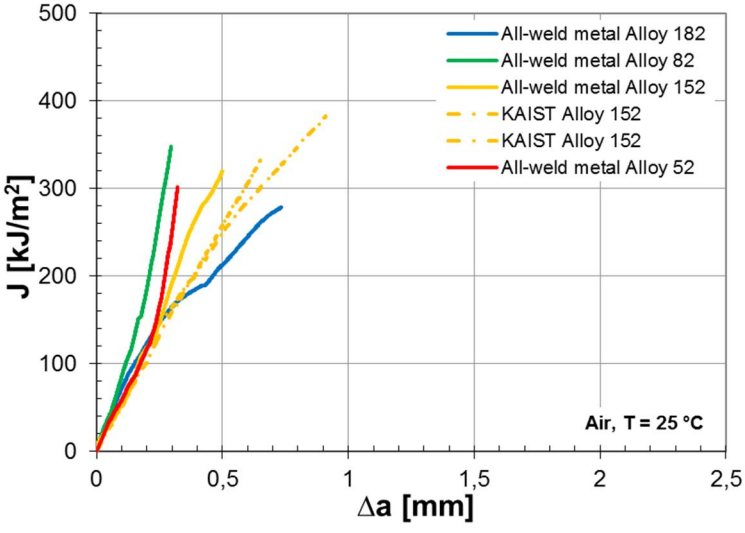

Figure 90. The J-R curves of the air tests for Alloys 182, 82, 152, and 52. The tested specimens were cut from all-weld metal test blocks except for Alloy 152 that was additionally tested by using two dissimilar metal weld (KAIST Alloy 152) specimens.

Table 8. Fracture resistance J_Q and tearing modulus T values for the air tests.

Material	J_Q (kJ/m^2)	$T_{0.5mm}$
Alloy 182 (All-weld metal)	182	212
Alloy 82 (All-weld metal)	>300	-
Alloy 152 (All-weld metal)	304	-
Alloy 152 (KAIST Alloy 152)	197	224
Alloy 152 (KAIST Alloy 152)	196	202
Alloy 52 (All-weld metal)	>300	-

9.1.2 100 cm^3 H_2/kg H_2O tests for AW specimens

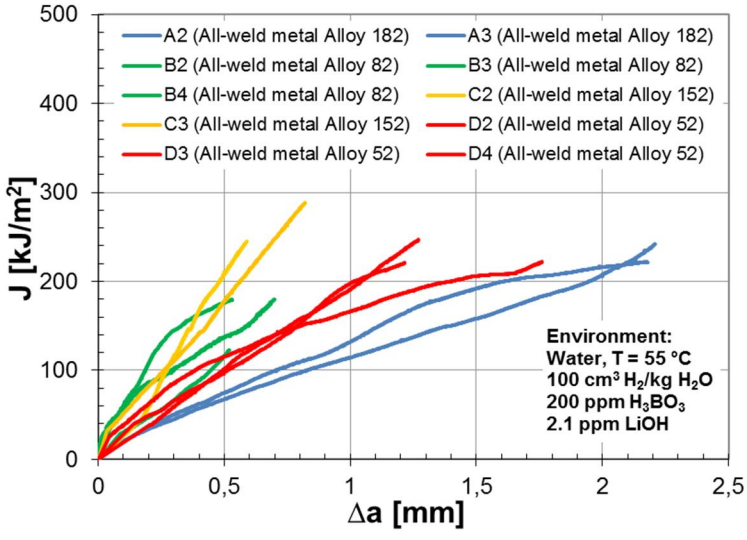

Figure 91. J-R curves for all-weld metal specimens of Alloys 182 (blue), 82 (green), 152 (yellow), and 52 (red), tested in hydrogenated low temperature water with high hydrogen content (100 cm^3 H_2/kg H_2O).

Table 9. Fracture resistance J_Q and tearing modulus T values for the tests conducted for all-weld metal specimens in low temperature water with high hydrogen content (100 cm^3 H_2/kg H_2O).

Specimen	J_Q (kJ/m^2)	$T_{0.5mm}$
A2 (All-weld metal Alloy 182)	53	97
A3 (All-weld metal Alloy 182)	42	98
B2 (All-weld metal Alloy 82)	100	112
B3 (All-weld metal Alloy 82)	57	285
B4 (All-weld metal Alloy 82)	155	95
C2 (All-weld metal Alloy 152)	124	284
C3 (All-weld metal Alloy 152)	113	270
D2 (All-weld metal Alloy 52)	54	200
D3 (All-weld metal Alloy 52)	47	257
D4 (All-weld metal Alloy 52)	85	135

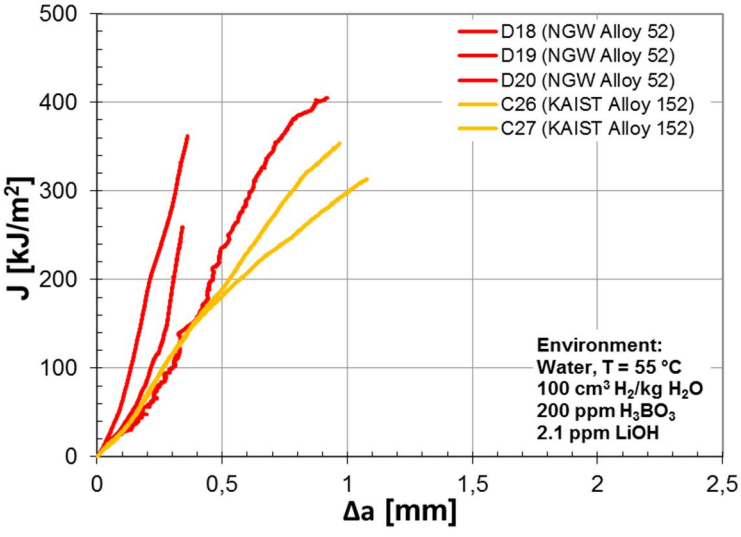

Figure 92. J-R curves for dissimilar metal weld (DMW) mock-up specimens of Alloys 152 (yellow) and 52 (red), tested in hydrogenated low temperature water with high hydrogen content (100 cm^3 H_2/kg H_2O).

Table 10. Fracture resistance J_Q and tearing modulus T values for the tests conducted for dissimilar weld metal specimens in low temperature water with high hydrogen content (100 cm^3 H_2/kg H_2O).

Specimen	J_Q (kJ/m^2)	$T_{0.5mm}$
C26 (KAIST Alloy 152)	118	238
C27 (KAIST Alloy 152)	118	190
D18 (NGW Alloy 52)	>300	-
D19 (NGW Alloy 52)	>300	-
D20 (NGW Alloy 52)	150	313

9.1.3 30 cm^3 H_2/kg H_2O tests for AW specimens

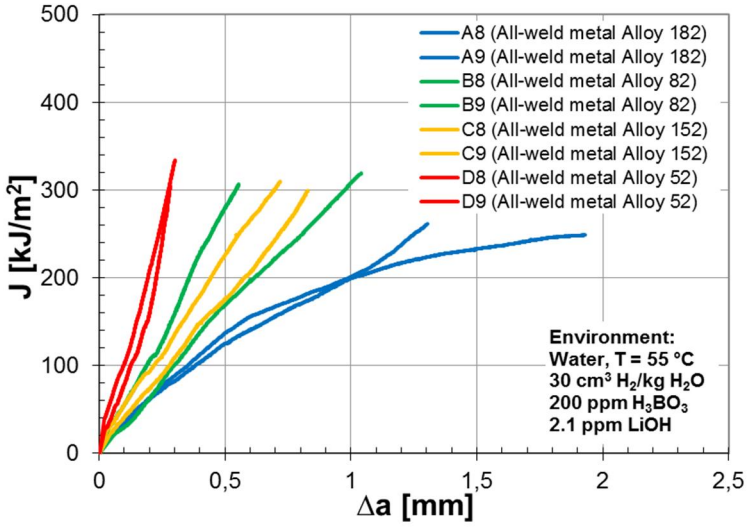

Figure 93. J-R curves for all-weld metal specimens of Alloys 182 (blue), 82 (green), 152 (yellow), and 52 (red), tested in hydrogenated low temperature water with moderate hydrogen content (30 cm^3 H_2/kg H_2O).

Table 11. Fracture resistance J_Q and tearing modulus T values for the tests conducted for all-weld metal specimens in low temperature water with moderate hydrogen content (30 cm^3 H_2/kg H_2O).

Specimen	J_Q (kJ/m^2)	$T_{0.5mm}$
A8 (All-weld metal Alloy 182)	84	177
A9 (All-weld metal Alloy 182)	78	124
B8 (All-weld metal Alloy 82)	252	391
B9 (All-weld metal Alloy 82)	102	217
C8 (All-weld metal Alloy 152)	108	122
C9 (All-weld metal Alloy 152)	151	296
D8 (All-weld metal Alloy 52)	>300	-
D9 (All-weld metal Alloy 52)	>300	-

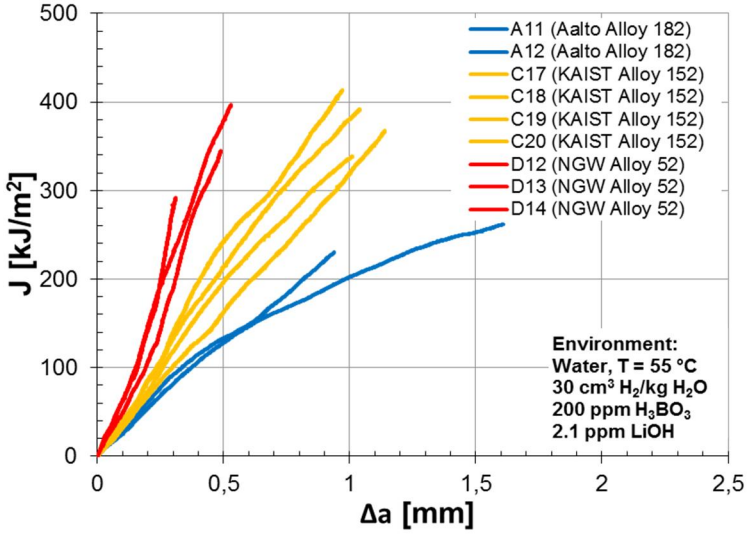

Figure 94. J-R curves for dissimilar metal weld (DMW) specimens of Alloys 182 (blue), 152 (yellow), and 52 (red), tested in hydrogenated low temperature water with moderate hydrogen content (30 cm^3 H_2/kg H_2O).

Table 12. Fracture resistance J_Q and tearing modulus T values for the tests conducted for dissimilar weld metal specimens in low temperature water with moderate hydrogen content (30 cm^3 H_2/kg H_2O).

Specimen	J_Q (kJ/m^2)	$T_{0.5mm}$
A11 (Aalto Alloy 182)	87	115
A12 (Aalto Alloy 182)	73	160
C17 (KAIST Alloy 152)	96	250
C18 (KAIST Alloy 152)	169	258
C19 (KAIST Alloy 152)	128	252
C20 (KAIST Alloy 152)	149	261
D12 (NGW Alloy 52)	>300	-
D13 (NGW Alloy 52)	>300	-
D14 (NGW Alloy 52)	>300	-

9.1.4 5 and 0 cm^3 H_2/kg H_2O tests for AW specimens of Alloy 152

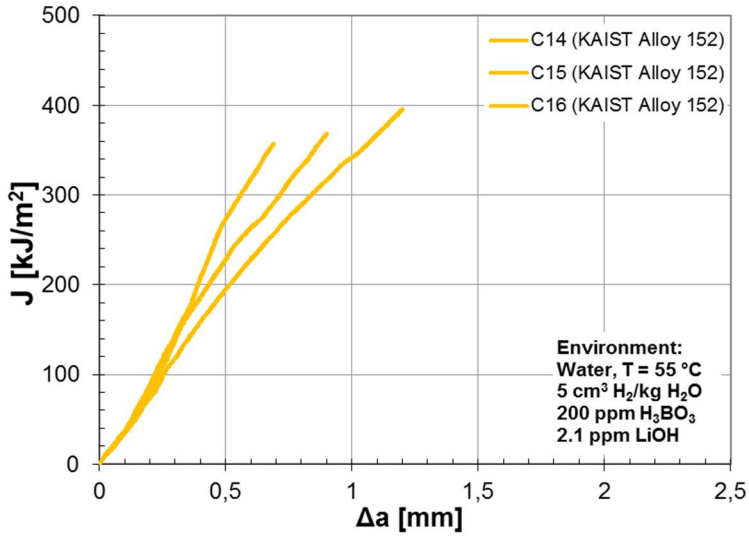

Figure 95. J-R curves for dissimilar metal weld (DMW) specimens of Alloy 152 tested in hydrogenated low temperature water with low hydrogen content (5 cm^3 H_2/kg H_2O).

Table 13. Fracture resistance J_Q and tearing modulus T values for the tests conducted for dissimilar weld metal specimens of Alloy 152 in low temperature water with low hydrogen content (5 cm^3 H_2/kg H_2O).

Specimen	J_Q (kJ/m^2)	$T_{0.5mm}$
C14 (KAIST Alloy 152)	174	283
C15 (KAIST Alloy 152)	123	235
C16 (KAIST Alloy 152)	165	281

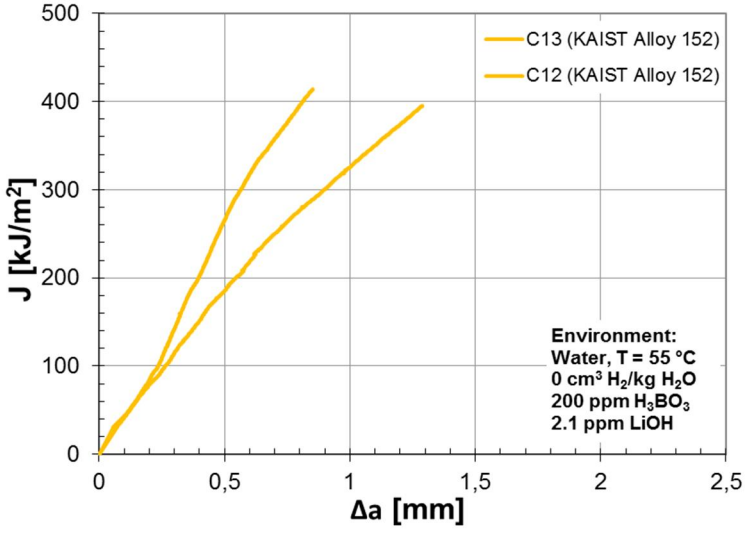

Figure 96. J-R curves for dissimilar metal weld (DMW) specimens of Alloy 152 tested in low temperature water without hydrogen addition.

Table 14. Fracture resistance J_Q and tearing modulus T values for the tests conducted for dissimilar weld metal specimens of Alloy 152 in low temperature water without hydrogen addition.

Specimen	J_Q (kJ/m^2)	$T_{0.5mm}$
C12 (KAIST Alloy 152)	192	417
C13 (KAIST Alloy 152)	109	229

9.1.5 100 cm^3 H_2/kg H_2O 24h pre-exposure tests for AW specimens

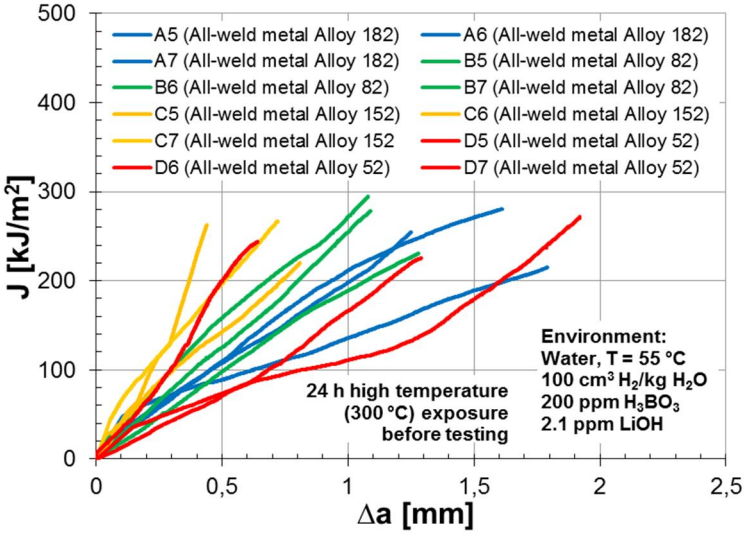

Figure 97. J-R curves for all-weld metal specimens of Alloys 182 (blue), 82 (green), 152 (yellow), and 52 (red), tested in hydrogenated low temperature water with high hydrogen content (100 cm^3 H_2/kg H_2O) after 24h pre-exposure to high temperature (300 °C) hydrogenated water.

Table 15. Fracture resistance J_Q and tearing modulus T values for the tests conducted for all-weld metal specimens in low temperature water with high hydrogen content (100 cm^3 H_2/kg H_2O) after 24 h pre-exposure to high temperature (300 °C) hydrogenated water.

Specimen	J_Q (kJ/m^2)	$T_{0.5mm}$
A5 (All-weld metal Alloy 182)	59	151
A6 (All-weld metal Alloy 182)	63	138
A7 (All-weld metal Alloy 182)	69	63
B5 (All-weld metal Alloy 82)	47	173
B6 (All-weld metal Alloy 82)	70	155
B7 (All-weld metal Alloy 82)	100	203
C5 (All-weld metal Alloy 152)	260	-
C6 (All-weld metal Alloy 152)	94	151
C7 (All-weld metal Alloy 152)	141	197
D5 (All-weld metal Alloy 52)	127	385
D6 (All-weld metal Alloy 52)	35	222
D7 (All-weld metal Alloy 52)	48	123

9.1.6 30 cm^3 H_2/kg H_2O 30 days pre-exposure tests for AW specimens

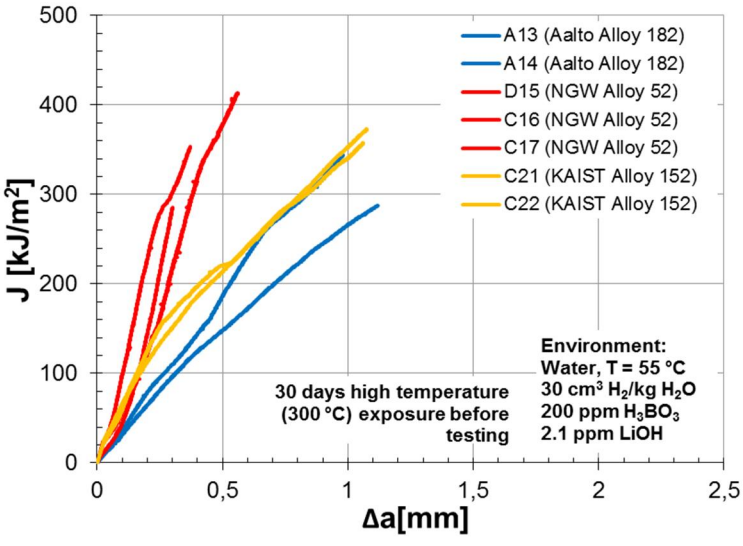

Figure 98. J-R curves for dissimilar metal weld (DMW) specimens of Alloys 182 (blue), 152 (yellow), and 52 (red), tested in hydrogenated low temperature water with moderate hydrogen content (30 cm^3 H_2/kg H_2O) after 30 days pre-exposure to high temperature (300 °C) hydrogenated water.

Table 16. Fracture resistance J_Q and tearing modulus T values for the tests conducted for all-weld metal specimens in low temperature water with moderate hydrogen content (30 cm^3 H_2/kg H_2O) after 30 days pre-exposure to high temperature (300 °C) hydrogenated water.

Specimen	J_Q (kJ/m^2)	$T_{0.5mm}$
A13 (Aalto Alloy 182)	113	408
A14 (Aalto Alloy 182)	93	173
C21 (KAIST Alloy 152)	189	72
C22 (KAIST Alloy 152)	169	187
D15 (NGW Alloy 52)	>300	-
D16 (NGW Alloy 52)	>300	-
D17 (NGW Alloy 52)	>300	-

9.1.7 5 cm^3 H_2/kg H_2O 30 days pre-exposure tests for AW specimens

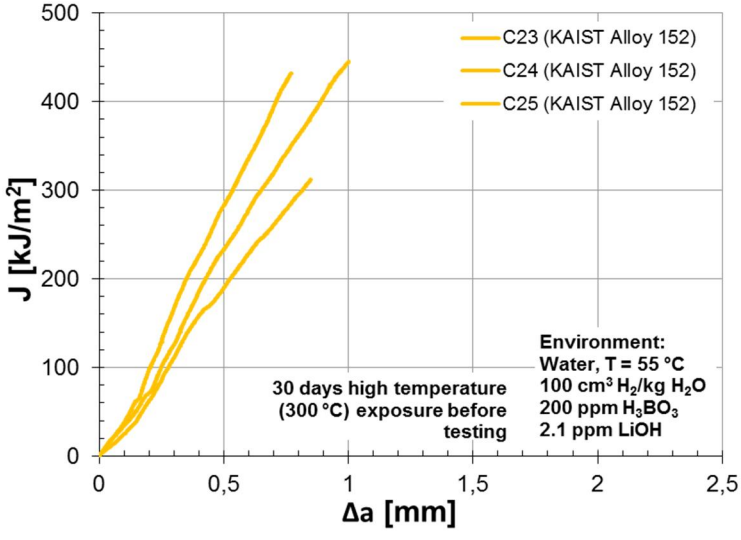

Figure 99. J-R curves for dissimilar metal weld (DMW) specimens of Alloy 152 tested in hydrogenated low temperature water with low hydrogen content (5 cm^3 H_2/kg H_2O) after 30 days pre-exposure to high temperature (300 °C) hydrogenated water

Table 17. Fracture resistance J_Q and tearing modulus T values for the tests conducted for DMW specimens in low temperature water with low hydrogen content (5 cm^3 H_2/kg H_2O) after 30 days pre-exposure to high temperature (300 °C) hydrogenated water.

Specimen	J_Q (kJ/m^2)	$T_{0.5mm}$
C23 (KAIST Alloy 152)	230	332
C24 (KAIST Alloy 152)	145	273
C25 (KAIST Alloy 152)	109	280

9.2 J-R test results for post-weld heat treated specimens

9.2.1 100 and 30 cm^3 H_2/kg H_2O tests for post-weld heat treated specimens

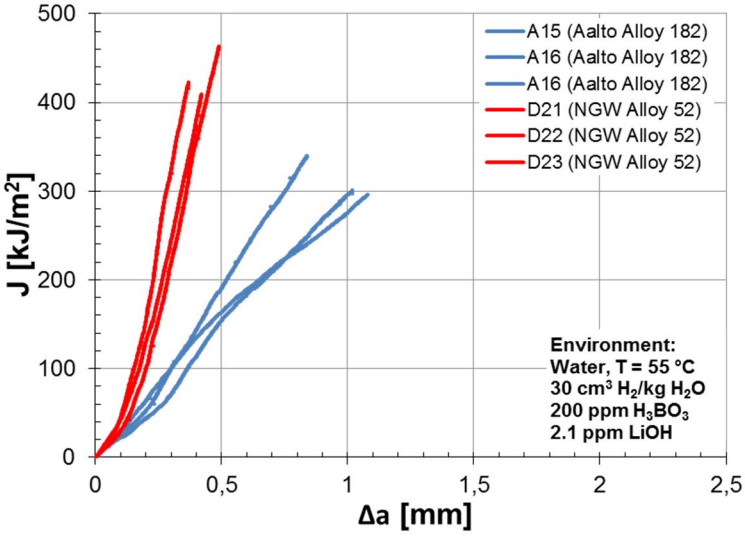

Figure 100. J-R curves for post-weld heat treated (PWHT) Alloy 182 and 52 DMW specimens tested in hydrogenated low temperature (55°C) water with moderate hydrogen content (30 cm^3 H_2/kg H_2O).

Table 18. Fracture resistance J_Q and tearing modulus T values for the tests conducted for PWHT DMW specimens in low temperature water with moderate hydrogen content (30 cm^3 H_2/kg H_2O).

Specimen	J_Q (kJ/m^2)	$T_{0.5mm}$
A15 (Aalto Alloy 182)	57	295
A16 (Aalto Alloy 182)	99	204
A17 (Aalto Alloy 182)	97	391
D21 (NGW Alloy 52)	>300	-
D22 (NGW Alloy 52)	>300	-
D23 (NGW Alloy 52)	>300	-

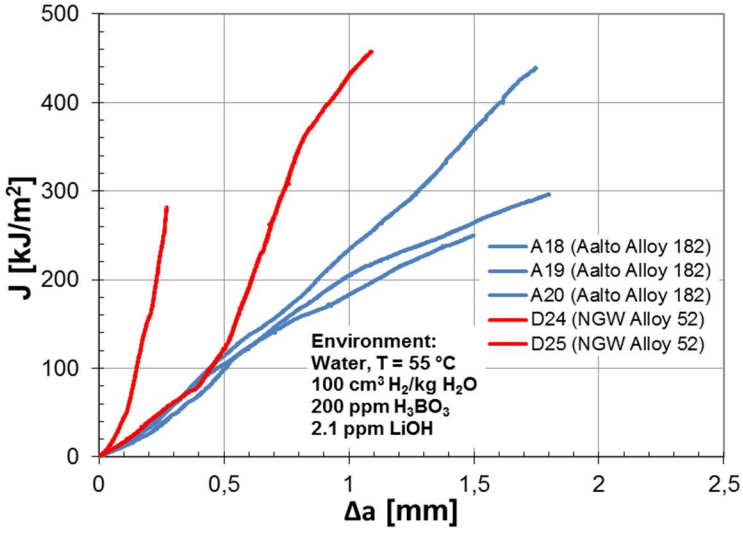

Figure 101. J-R curves for post-weld heat treated (PWHT) Alloy 182 and 52 DMW specimens tested in hydrogenated low temperature (55°C) water with high hydrogen content (100 cm^3 H_2/kg H_2O).

Table 19. Fracture resistance J_Q and tearing modulus T values for the tests conducted for PWHT DMW specimens in low temperature water with high hydrogen content (100 cm^3 H_2/kg H_2O).

Specimen	J_Q (kJ/m^2)	$T_{0.5mm}$
A18 (Aalto Alloy 182)	32	242
A19 (Aalto Alloy 182)	46	177
A20 (Aalto Alloy 182)	43	135
D24 (NGW Alloy 52)	55	479
D25 (NGW Alloy 52)	>300	-

Series title and number

VTT Science 105

Title	**Effect of microstructure on low temperature hydrogen-induced cracking behaviour of nickel-based alloy weld metals**
Author(s)	Matias Ahonen
Abstract	Various nickel-based materials are susceptible to low temperature crack propagation (LTCP) in simulated PWR (pressurized water reactor) water at a temperature range of about 50 to 150 °C. Experimental evidence from various sources shows that the hydrogen content of the water has a decreasing effect on the fracture resistance, thus LTCP is widely regarded as a hydrogen-induced phenomenon. This thesis concentrates on the LTCP phenomenon of Alloy 182, 82, 152 and 52 weld metals. The studied materials were both all-weld metals and dissimilar metal weld (DMW) mock-ups. The material conditions studied in this work were as-welded (AW), post-weld heat treated (PWHT) and high temperature water pre-exposed. The experimental work was divided in fracture mechanical testing in an environment, microstructural examination of fracture surfaces and hydrogen thermal desorption measurements. The obtained J-R test results show that Alloy 182 is the most susceptible nickel-based weld metal to LTCP, whereas Alloy 52 retains its high fracture resistance in hydrogenated water with moderate hydrogen content. The results obtained for all-weld metal Alloy 52 showed, however, a clear reduction of fracture resistance when tested at a high hydrogen content (100 cm^3 H_2/kg H_2O), whereas narrow gap mock-up Alloy 52 DMW appeared to be less susceptible to LTCP in the corresponding environment. Hydrogen concentrations of Alloy 182 and 152 weld metal samples decrease during the high temperature water exposure, even when exposed to water containing 30 cm^3 H_2/kg H_2O, and the fracture resistance values of Alloys 182 and 152 are improved. A clear relation between the low fracture resistance values and intergranular/interdendritic type of fracture was observed. The effect of grain boundary carbides and their hydrogen trapping properties are discussed based on the obtained SEM/EDS and thermal desorption spectroscopy results and a model was applied in order to determine the activation energies for hydrogen desorption of Alloys 182 and 52. The different LTCP behaviour of Alloy 182 and 52 weld metals is believed to be caused mainly by different types of carbides dominating the hydrogen-induced fracture. The carbides may have an effect on hydrogen distribution at the grain/dendrite boundaries and the availability of hydrogen close to the crack tip, by acting as trapping sites for hydrogen and by affecting the strain distribution at the grain boundary area.
ISBN, ISSN	ISBN 978-951-38-8338-6 (Soft back ed.) ISBN 978-951-38-8339-3 (URL: http://www.vttresearch.com/impact/publications) ISSN-L 2242-119X ISSN 2242-119X (Print) ISSN 2242-1203 (Online)
Date	August 2015
Language	English, Finnish abstract
Pages	132 p. + app. 13 p.
Name of the project	Environmental influence on cracking susceptibility and ageing of nuclear materials (ENVIS)
Commissioned by	
Keywords	Nickel-based weld metals, low temperature crack propagation, hydrogen trapping, fracture resistance
Publisher	VTT Technical Research Centre of Finland Ltd P.O. Box 1000, FI-02044 VTT, Finland, Tel. 020 722 111

Julkaisun sarja ja numero

VTT Science 105

Nimeke	**Mikrorakenteen vaikutus nikkeliseoshitsien vedyn aiheuttamaan murtumiseen matalissa lämpötiloissa**
Tekijä(t)	Matias Ahonen
Tiivistelmä	Useiden nikkeliseoshitsien on todettu olevan alttiita matalan lämpötilan särönkasvulle (eng., low temperature crack propagation, LTCP) simuloidussa painevesireaktoriympäristössä lämpötilavälillä 50-150 °C. Eri lähteissä esitetty kokeellinen tulosaineisto osoittaa, että vetypitoisuuden kasvaessa kyseisten materiaalien murtumisvastus alenee, joten LTCP:n uskotaan yleisesti olevan vedyn aiheuttama ilmiö. Tässä väitöstyössä keskitytään LTCP -ilmiöön nikkelivaltaisissa Alloy 182, 82, 152 ja 52 hitsiaineissa. Tutkittavat materiaalit koostuvat sekä puhtaista hitsiaineista sekä Alloy 182, 152 ja 52 hitsiaineiden tapauksessa myös eriparihitseistä. Näytteitä tutkittiin hitsauksen jälkeen, jälkilämpökäsiteltynä sekä korkealämpötilavedessä suoritetun altistuksen jälkeen. Työn kokeellinen osa jakautui murtumismekaaniseen testaukseen ympäristössä, murtopintojen ja poikkileikkausten mikroskopiatutkimuksiin sekä vedyn desorptiomittauksiin. J-R -kokeiden tulokset osoittavat Alloy 182 hitsiaineen olevan LTCP -herkin nikkelivaltainen hitsiaine, kun taas Alloy 52 säilyttää korkean murtumisvastuksen vetypitoisuudella 30 cm^3 H_2/kg H_2O. Kuitenkin myös puhtaan Alloy 52 hitsiaineen murtumisvastuksessa havaittiin selkeä aleneminen korkealla vetypitoisuudella (100 cm^3 H_2/kg H_2O). Toisaalta Alloy 52 kapearailohitsi säilytti useimpien koesauvojen tapauksessa korkean murtumisvastuksen vastaavassa runsasvetyisessä ympäristössä. Vetypitoisuusmittaukset osoittavat, että altistus korkealämpötilavedessä alentaa Alloy 182 ja 152 hitsiaineiden kokonaisvetypitoisuuksia veden vetypitoisuuden ollessa 30 cm^3 H_2/kg H_2O. Kyseisten materiaalien murtumissitkeysarvot nousevat korkealämpötilavesialtistuksen myötä. Matalampien murtumissitkeysarvojen ja rae- tai dendriittirajamurtuman välillä todettiin selvä yhteys. Raerajakarbidien toimimista vetyloukkuina arvioitiin saatujen mikroskopiatulosten pohjalta. Lisäksi työssä sovellettiin mallia vedyn desorption aktivaatioenergioiden määrittämiseksi Alloy 182 ja 52 hitsiaineissa. Kyseisten materiaalien erilaisen LTCP -käyttäytymisen uskotaan johtuvan pääasiassa niissä esiintyvistä erityyppisistä raerajakarbideista, jotka ovat keskeisessä asemassa vedyn aiheuttamassa murtumisessa. Erilaisilla karbideilla voi myös olla erilainen vaikutus vedyn jakautumiseen rae- tai dendriittirajoilla sekä vedyn saatavuuteen särön kärjen läheisyydessä, koska karbidit toimivat vetyloukkuina ja vaikuttavat raerajojen ja niiden lähialueiden deformaatiojakaumaan.
ISBN, ISSN	ISBN 978-951-38-8338-6 (nid.) ISBN 978-951-38-8339-3 (URL: http://www.vtt.fi/julkaisut) ISSN-L 2242-119X ISSN 2242-119X (Painettu) ISSN 2242-1203 (Verkkojulkaisu)
Julkaisuaika	Elokuu 2015
Kieli	Englanti, suomenkielinen tiivistelmä
Sivumäärä	132 s. + liitt. 13 s.
Projektin nimi	Ympäristön vaikutus ydinvoimalaitosmateriaalien murtumiseen ja vanhenemiseen (ENVIS)
Rahoittajat	
Avainsanat	Nikkeliseoshitsit, matalan lämpötilan särönkasvu, vedyn loukkuuntuminen, murtumisvastus
Julkaisija	Teknologian tutkimuskeskus VTT Oy PL 1000, 02044 VTT, puh. 020 722 111

Effect of microstructure on low temperature hydrogen-induced cracking behaviour of nickel-based alloy weld metals

Various nickel-based materials are susceptible to low temperature crack propagation (LTCP) in simulated PWR (pressurized water reactor) water at a temperature range of about 50 to 150 °C. Although no LTCP related incidents have been reported in open literature thus far, the understanding of the possible material degradation phenomena is of great importance in order to ensure safe operation of nuclear power plants.

The experimental part of this work was focused on LTCP susceptibility of nickel-based Alloy 182, 82, 152 and 52 weld metals. Both all-weld metals and dissimilar metal weld (DMW) mock-ups were studied. The obtained J-R test results show that Alloy 182 is the most susceptible nickel-based weld metal to LTCP, whereas Alloy 52 retains its high fracture resistance in hydrogenated water with moderate hydrogen content. However, some specimens of Alloy 52 showed a dramatic reduction of fracture resistance with high dissolved hydrogen content. A clear relation between the low fracture resistance values and intergranular/interdendritic type of fracture was observed. The different LTCP behaviour of Alloy 182 and 52 weld metals is believed to be caused mainly by different types of carbides dominating the hydrogen-induced fracture. The carbides may have an effect on hydrogen distribution at the grain/dendrite boundaries and the availability of hydrogen close to the crack tip, by acting as trapping sites for hydrogen and by affecting the strain distribution at the grain boundary area.

ISBN 978-951-38-8338-6 (Soft back ed.)
ISBN 978-951-38-8339-3 (URL: http://www.vttresearch.com/impact/publications)
ISSN-L 2242-119X
ISSN 2242-119X (Print)
ISSN 2242-1203 (Online)